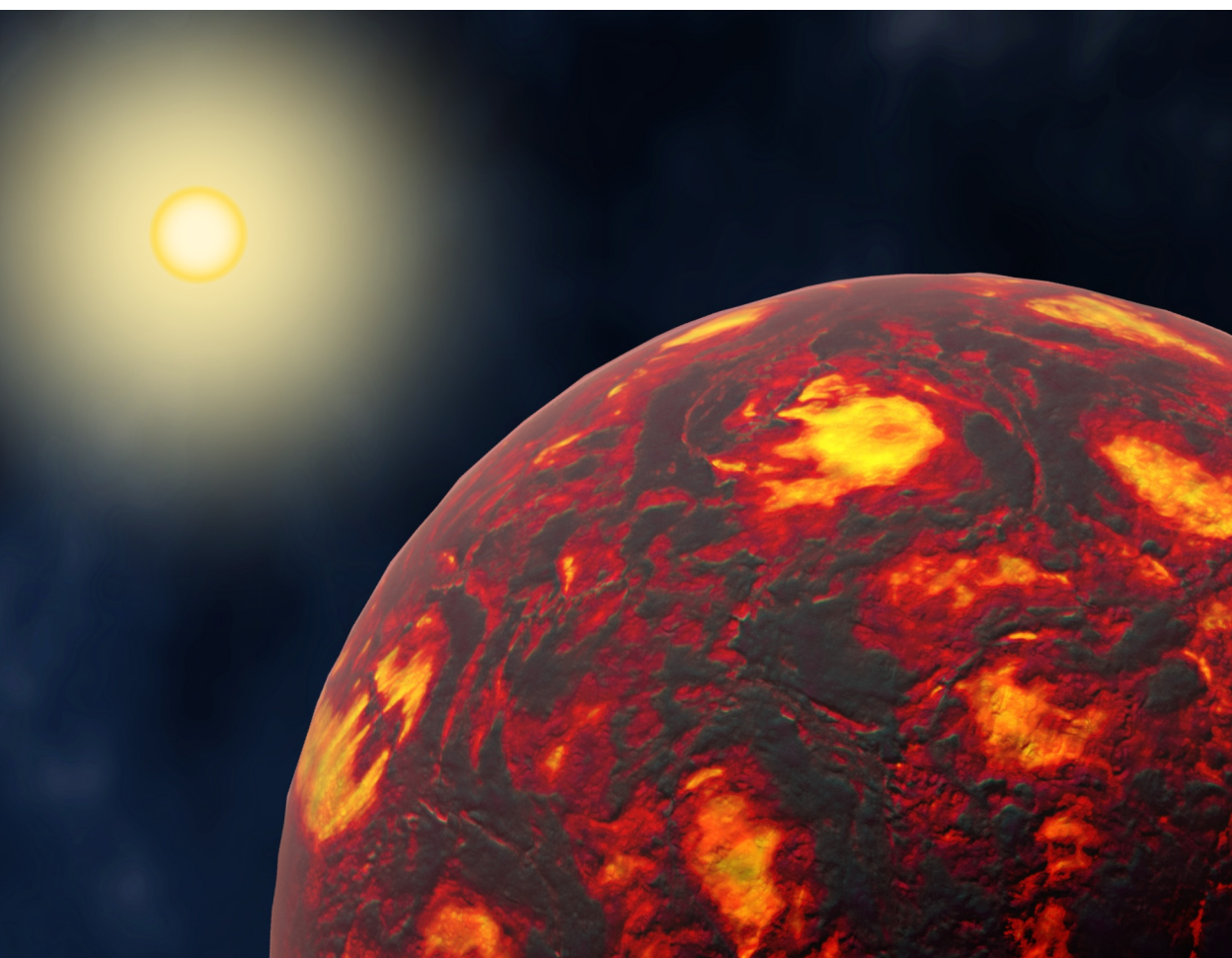


Exploring close-in exoplanets with space telescopes

Jayshil A. Patel



Exploring close-in exoplanets with space telescopes

Jayshil A. Patel

Academic dissertation for the Degree of Doctor of Philosophy in Astronomy at Stockholm University to be publicly defended on Wednesday 8 October 2025 at 13.00 in FD5, AlbaNova University Center, Roslagstullsbacken 21.

Abstract

Since the discovery of the first planet outside our Solar System, known as an exoplanet, we have come a long way in their study, from their detection to characterisation. The advent of ultra-precision telescopes such as the CHaracterising ExOPlanet Satellite (CHEOPS), the Transiting Exoplanet Survey Satellite (TESS), and the *James Webb* Space Telescope (JWST) has enabled us to examine not only the composition of exoplanets, but also their atmospheres. The present thesis introduces the subject of transiting exoplanets and reviews research on close-in exoplanets.

After presenting a brief history of the field and the techniques used to detect exoplanets, we focus on the transit method to characterise exoplanets and their atmospheres. We discuss how a transit (flux drop when a planet passes in front of its host star), occultations (flux change when a planet is blocked by its host star), and phase curves (flux variations throughout planetary orbit) can be used to study planetary bulk, orbital, and atmospheric properties. We then describe how we can exploit the photometric and spectroscopic capabilities of space-based telescopes, together with Bayesian data analysis, to extract the planetary properties from observations. Some of the prime targets to observe in transit geometry are close-in planets. In this thesis, we examine two classes of close-in planets: ultra-short-period rocky planets (USPs) and hot Jupiters. USPs are rocky planets that orbit their host star within about a day. They have very high equilibrium temperatures, resulting in a partially or fully molten surface, which can outgas a thin secondary atmosphere containing rock vapours (e.g., SiO) or volatiles (e.g., CO, CO₂). Characterising atmospheres help constrain their atmospheric and interior composition. Hot Jupiters are hot gas giant planets orbiting very close to their host star. They have peculiar atmospheric chemistries with cloudless daysides because of high temperatures, typically resulting in low albedos. Hot Jupiters have a characteristic thermal structure of a strong day-night contrast and a strong eastward jet stream. The hottest among them are known as ultra-hot Jupiters, and they can have a distinct atmospheric structure compared to the cooler hot Jupiters.

Scientific articles presented in this thesis use the transit method to primarily characterise the atmospheres of close-in exoplanets. We use CHEOPS, TESS, and JWST to observe two USPs, TOI-561 b and 55 Cnc e, and two hot Jupiters, WASP-189 b and HD 189733 b, photometrically and/or spectroscopically. Our photometric observations of TOI-561 b not only constrains the internal structure of the planet but also finds a hint of a secondary silicate atmosphere. The spectroscopic observations of 55 Cnc e with JWST reveals a strong variability in the dayside emission, which could be the result of a transient outgassed atmosphere or a circumstellar inhomogeneous dust torus. The photometric observations of hot Jupiters constrains the thermal and reflective properties of those planets. A TESS phase curve of the ultra-hot Jupiter WASP-189 b measures the temperature map of the planet, which helps in estimating Bond albedo and heat redistribution efficiency. Finally, optical observations of cooler hot Jupiter HD 189733 b with CHEOPS uncover a very low geometric albedo. The small albedo is consistent with a cloud-free atmosphere with Rayleigh scattering from hydrogen molecules and sodium absorption.

Keywords: *Exoplanets, Exoplanet atmospheres, Transits, Occultations, Phase curves, Ultra-short-period rocky planets, Hot Jupiters, Photometric observations, Spectroscopic observations, CHaracterising ExOPlanet Satellite (CHEOPS), Transiting Exoplanet Survey Satellite (TESS), James Webb Space Telescope (JWST).*

Stockholm 2025

<http://urn.kb.se/resolve?urn=urn:nbn:se:su:diva-245815>

ISBN 978-91-8107-362-1
ISBN 978-91-8107-363-8

Department of Astronomy

Stockholm University, 106 91 Stockholm



EXPLORING CLOSE-IN EXOPLANETS WITH SPACE TELESCOPES

Jayshil A. Patel



Exploring close-in exoplanets with space telescopes

Jayshil A. Patel

©Jayshil A. Patel, Stockholm University 2025

ISBN print 978-91-8107-362-1
ISBN PDF 978-91-8107-363-8

Cover image: Artist's impression of hot rocky exoplanet 55 Cancri e, which is believed to have a full or partial lava surface on its dayside. Picture credits: ESA/Hubble, M. Kornmesser

Printed in Sweden by Universitetsservice US-AB, Stockholm 2025

To my family

Abstract

Since the discovery of the first planet outside our Solar System, known as an exoplanet, we have come a long way in their study, from their detection to characterisation. The advent of ultra-precision telescopes such as the CHaracterising ExOPlanet Satellite (CHEOPS), the Transiting Exoplanet Survey Satellite (TESS), and the *James Webb* Space Telescope (JWST) has enabled us to examine not only the composition of exoplanets, but also their atmospheres. The present thesis introduces the subject of transiting exoplanets and reviews research on close-in exoplanets.

After presenting a brief history of the field and the techniques used to detect exoplanets, we focus on the transit method to characterise exoplanets and their atmospheres. We discuss how a transit (flux drop when a planet passes in front of its host star), occultations (flux change when a planet is blocked by its host star), and phase curves (flux variations throughout planetary orbit) can be used to study planetary bulk, orbital, and atmospheric properties. We then describe how we can exploit the photometric and spectroscopic capabilities of space-based telescopes, together with Bayesian data analysis, to extract the planetary properties from observations. Some of the prime targets to observe in transit geometry are close-in planets. In this thesis, we examine two classes of close-in planets: ultra-short-period rocky planets (USPs) and hot Jupiters. USPs are rocky planets that orbit their host star within about a day. They have very high equilibrium temperatures, resulting in a partially or fully molten surface, which can outgas a thin secondary atmosphere containing rock vapours (e.g., SiO) or volatiles (e.g., CO, CO₂). Characterising atmospheres help constrain their atmospheric and interior composition. Hot Jupiters are hot gas giant planets orbiting very close to their host star. They have peculiar atmospheric chemistries with cloudless daysides because of high temperatures, typically resulting in low albedos. Hot Jupiters have a charac-

teristic thermal structure of a strong day-night contrast and a strong eastward jet stream. The hottest among them are known as ultra-hot Jupiters, and they can have a distinct atmospheric structure compared to the cooler hot Jupiters.

Scientific articles presented in this thesis use the transit method to primarily characterise the atmospheres of close-in exoplanets. We use CHEOPS, TESS, and JWST to observe two USPs, TOI-561 b and 55 Cnc e, and two hot Jupiters, WASP-189 b and HD 189733 b, photometrically and/or spectroscopically. Our photometric observations of TOI-561 b not only constrains the internal structure of the planet but also finds a hint of a secondary silicate atmosphere. The spectroscopic observations of 55 Cnc e with JWST reveals a strong variability in the dayside emission, which could be the result of a transient outgassed atmosphere or a circumstellar inhomogeneous dust torus. The photometric observations of hot Jupiters constrains the thermal and reflective properties of those planets. A TESS phase curve of the ultra-hot Jupiter WASP-189 b measures the temperature map of the planet, which helps in estimating Bond albedo and heat redistribution efficiency. Finally, optical observations of cooler hot Jupiter HD 189733 b with CHEOPS uncover a very low geometric albedo. The small albedo is consistent with a cloud-free atmosphere with Rayleigh scattering from hydrogen molecules and sodium absorption.

Sammanfattning (Swedish)

Sedan upptäckten av den första planeten utanför vårt solsystem, känd som en exoplanet, har vi kommit långt i studiet av exoplaneter – från deras upptäckt till deras karakterisering. Framväxten av ultraprecisa teleskop som Characterising ExOPlanet Satellite (CHEOPS), Transiting Exoplanet Survey Satellite (TESS) och *James Webb* Space Telescope (JWST) har möjliggjort att vi inte bara kan undersöka planeternas sammansättning utan även deras atmosfärer. Denna avhandling introducerar ämnet passage-exoplaneter och ger en översikt över forskningen kring nära liggande exoplaneter.

Efter en kort historik över fältet och en genomgång av tekniker för att upptäcka exoplaneter, fokuserar vi på passagemetoden för att karakterisera exoplaneter och deras atmosfärer. Vi diskuterar hur en passage (ljusminskning från stjärnan när en planet passerar framför sin värdstjärna), ockultationer (förändring i ljusflöde när planeten blockeras av sin värdstjärna) och faskurvor (ljusvariationer under planetens omloppsbanan) kan användas för att studera planeternas struktur, banegenskaper och atmosfärer. Vi beskriver sedan hur vi kan utnyttja fotometriska och spektroskopiska möjligheter hos rymdbaserade teleskop, tillsammans med bayesiansk dataanalys, för att extrahera planetära egenskaper från observationer. Några av de mest gynnsamma målen för passageobservationer är planeter som ligger nära sin stjärna. I denna avhandling undersöks två klasser av sådana planeter: ultra-kortperiodiska stenplaneter (USPs) och heta Jupitrar. USPs är stenplaneter som kretsar runt sin värdstjärna på ungefär en dag. De har mycket höga jämviktstemperaturer, vilket kan leda till en delvis eller helt smält yta som kan avge en tunn sekundär atmosfär bestående av bergartsångor (t.ex. SiO) eller flyktiga ämnen (t.ex. CO, CO₂). Karakterisering av en sådan atmosfär hjälper till att begränsa både atmosfärens och planetens inre sammansättning. Heta Jupitrar är gasjättar som kretsar mycket nära sin stjärna. De har en ovanlig atmosfärisk kemi, där dagsi-

dan ofta är molnfri på grund av de höga temperaturerna, vilket i sin tur leder till låga albedon. Dessa planeter har en karakteristisk termisk struktur med stark kontrast mellan dag och natt samt en kraftig östlig jetström. De allra hetaste bland dem kallas ultra-heta Jupitrar och kan ha en atmosfär med strukturer som skiljer sig från de svalare heta Jupitrarna.

De vetenskapliga artiklar som presenteras i denna avhandling använder passagemetoden för att i första hand karakterisera atmosfärerna hos närliggande exoplaneter. Vi använder CHEOPS, TESS och JWST för att observera två USPs, TOI-561 b och 55 Cnc e, samt två heta Jupitrar, WASP-189 b och HD 189733 b, fotometriskt och/eller spektroskopiskt. Våra fotometriska observationer av TOI-561 b begränsar inte bara planetens inre struktur utan avslöjar även en möjlig sekundär atmosfär av silikater. Spektroskopiska observationer av 55 Cnc e med JWST visar en stark variation i emissionssignalen från dagsidan, vilket kan bero på en tillfällig utgasad atmosfär eller en ojämn stoftskiva runt stjärnan. De fotometriska observationerna av heta Jupitrar begränsar deras termiska och reflektiva egenskaper. TESS-faskurvan för den ultra-heta Jupiter-planeten WASP-189 b gjorde det möjligt att skapa en temperaturkarta över planeten, vilket hjälper till att uppskatta Bond-albedo och effektiviteten i värmeomfördelning. Slutligen avslöjar optiska observationer av den svalare heta Jupiter-planeten HD 189733 b med CHEOPS ett mycket lågt geometriskt albedo. Det låga albedot är förenligt med en molnfri atmosfär med Rayleigh-spridning från vätemolekyler och natriumabsorption.

Sārānsh (Gujarati)

સૌરમંડળની બહાર પહેલા બાહ્યાવકાશી ગ્રહની શોધ બાદ આજે આપણે તેમની શોધથી લઈને તેમના વિગતવાર વિશ્લેષણમાં ઘણી પ્રગતિ કરી છે. Characterising ExOPlanet Satellite (CHEOPS), the Transiting Exoplanet Survey Satellite (TESS), અને James Webb Space Telescope (JWST) જેવા ઉચ્ચ ચોક્સાઈયક્ટ ટેલિસ્કોપના વિકાસે આપણને બાહ્યાવકાશી ગ્રહોના ફક્ત બંધારણ જ નહિ, પરંતુ તેમના વાતાવરણના સંશોધનમાં પણ ઘણી મદદ કરી છે. પ્રસ્તુત શોધનિબંધ અધિકમાણીય પરગ્રહોના વિષયનો પરિચય આપે છે અને નિકટ-કક્ષીય પરગ્રહો પરના સંશોધનની સમીક્ષા કરે છે.

પરગ્રહોના વિષયના ઈતિહાસની અને તેમને શોધ કરવા વપરાતી વિવિધ પદ્ધતિઓની સંક્ષિમ રજ્યાત કર્યા બાદ આપણે બાહ્યાવકાશી ગ્રહો અને તેમના વાતાવરણનો અભ્યાસ કરવામાં ઉપયોગી એવી અધિકમાણની રીત પર ધ્યાન કેન્દ્રિત કરીશું. આપણે એ ચર્ચા કરીશું કે અધિકમાણ (પિતૃતારાની આગામણી ગ્રહના પસાર થવાને કારણે તારાના પ્રકાશમાં થતો ઘટાડો), ગ્રહાવરણ (ગ્રહના પ્રકાશમાં ગ્રહના તેના પિતૃતારાની પાછળથી પસાર થવાને કારણે થતો અવરોધ), અને કળા વફની (ગ્રહની સંપૂર્ણ ભ્રમારકક્ષા દરમ્યાન તેની અલગ કળાઓને કારણે ગ્રહના પ્રકાશમાં આવતો બદલાવ) મદદથી આપણે કેવી રીતે ગ્રહના બંધારણીય, કક્ષીય, અને વાતાવરણીય ગુણધર્મોનો અભ્યાસ કરી શકીએ. ત્યારબાદ આપણે અવકાશ-સ્થિત ટેલિસ્કોપોની પ્રકાશ-માપન અને વર્ણપટીય ક્ષમતાઓનો, બેયાયીયન ડેટા વિશ્લેષણની સાથે, ઉપયોગ કરીને કેવી રીતે ગ્રહોની લાક્ષણિકતાઓનો અભ્યાસ કરી શકીએ એના પર ચર્ચા કરીશું. અધિકમાણ દરમ્યાન અવલોકન કરવા માટે નિકટ-કક્ષીય પરગ્રહો સૌથી ઉત્કૃષ્ટ લક્ષ્યો પૈકીના એક છે. આ શોધનિબંધમાં આપણે નિકટ-કક્ષીય પરગ્રહોના બે વર્ગાનું પરીક્ષણ કરીશું: અતિ-સ્મીપ કક્ષીય ખડકાળ ગ્રહો અને ઉષ્ણ બૂહસ્પતિઓ. આમાંથી પ્રથમ પ્રકારના ગ્રહો મુખ્યત્વે ખડકોના બનેલા છે જેઓ તેમના પિતૃતારાની આસપાસ આશરે એક દિવસમાં પરિકમા પાર્શ્વ કરે છે. તેમનું ઉષ્ણતાસમસ્થિતિ તાપમાન ઘણું ઉંચુ હોવાને કારણે તેમની ભૂસપાટી સંપૂર્ણ કે આંશિક પીગળેલી હોય છે. આવી ભૂસપાટી ખડકીય બાણ્ય (જેવી કે, SiO) અથવા બાણ્યોભવનશીલ પદાર્થોનું (જેવા કે, CO, CO₂) બનેલું પાતળું વાતાવરણ ઉત્સર્જિત કરી શકે છે. આવા વાતાવરણનો અભ્યાસ ગ્રહોના વાતાવરણ અને આંતરિક બંધારણને સમજવા મદદરૂપ છે. ઉષ્ણ બૂહસ્પતિઓ તેમના પિતૃતારાની ખૂબ જ નજીકથી પરિકમા કરતા ગરમ વાયુમાન ગ્રહો છે. તેઓ વિલક્ષણ વાતાવરણ ધરાવે છે જેમાં તેમની દિવસની બાજુ, ખૂબ જ ઉંચા તાપમાનને કારણે, વાદળરહિત હોય છે, જે સામાન્ય રીતે લઘુ પરાવર્તાકમાં પરિણામે

છે. ઉષ્ણ બૃહસ્પતિઓનું ઉભાગતિય બંધારણ પ્રબળ દિન-રાત્રિ તાપમાનના તફાવતવાળું અને શક્તિશાળી પૂર્વીય વાયુપ્રવાહ ધરાવતું વિશિષ્ટ હોય છે. તેમનામાંના વધુ પડતા ગરમ ગ્રહો અતિઉષ્ણ બૃહસ્પતિઓ તરીકે ઓળખાય છે, અને તેઓ હંડા ઉષ્ણ બૃહસ્પતિઓની સરખામણીમાં નિરાળું વાતાવરણીય બંધારણ ધરાવે છે.

આ શોધનિબંધમાં સમાવાયેલા સંશોધનપત્રો અધિકમાણની પદ્ધતિ વડે નિકટ-કક્ષીય ગ્રહોના મુખ્યત્વે વાતાવરણનો અભ્યાસ કરે છે. અમે CHEOPS, TESS, અને JWSTનો ઉપયોગ બે અતિ-સમીપ કક્ષીય ખડકાળ ગ્રહો, TOI-561 b અને 55 Cnc e, તથા બે ઉષ્ણ બૃહસ્પતિઓ, WASP-189 b અને HD 189733 bનું પ્રકાશ-માપન અને/અથવા વર્ણપટીય અવલોકન કરવામાં કર્યો. અમારા TOI-561 bના પ્રકાશ-માપન અવલોકનોએ ફક્ત ગ્રહના આંતરિક બંધારણની શક્યતોઓને મર્યાદિત કરવામાં જ યોગદાન નહિ આપ્યું, પરંતુ તેમણે ગ્રહ પર દ્વિતીય સિલિકેટ વાતાવરણના સંકેત પણ આપ્યા. 55 Cnc eના JWST દ્વારા લેવાયેલા વર્ણપટીય અવલોકનોએ ગ્રહની દિવસની બાજુના ઉત્સર્જનમાં નોંધપાત્ર પરિવર્તનશીલતા છતી કરી, જે અસ્થાયી ઉત્સર્જિત વાતાવરણ અથવા પરિતારક અસમાંગ ધળવલયના પરિણામે ઉદ્ભવી શકે છે. ઉપરના બે ઉષ્ણ બૃહસ્પતિઓના પ્રકાશ-માપન અવલોકનોએ તે ગ્રહોના ઉખ્ખીય અને પરાવર્તિય ગુણધર્મોને નિર્ધારિત કરવામાં સહાય આપી છે. અતિઉષ્ણ બૃહસ્પતિ WASP-189 bના TESS કળા વક્ફાએ તે ગ્રહનો તાપમાન નકશો માપ્યો, જેણે ગ્રહના બોન્ડ પરાવર્તાક અને ઉષ્ણા પુનર્વિતરણ ક્ષમતાનો અંદાજ આપવામાં મદદ કરી. છેલ્લે, શીતળ ઉષ્ણ બૃહસ્પતિ, HD 189733 bના CHEOPS વડે લેવાયેલા દૃશ્ય-પ્રકાશીય અવલોકનોએ તે ગ્રહનો ખૂબ નીચો ભૂમિતિય પરાવર્તાક શોધયો. આવો લઘુ પરાવર્તાક વાદળ-વિહિન વાતાવરણમાં હાઈડ્રોજન આણુઓના રેલે પ્રકીર્ણન અને સોડિયમ શોષણ સાથે સુસંગત છે.

List of Papers

The following papers are **included** in this thesis.

Paper I: **CHEOPS and TESS view of the ultra-short-period super-Earth TOI-561 b**

Patel, J. A., Egger, J. A., Wilson, T. G., et al., 2023, *Astronomy & Astrophysics*, 679, A92.

DOI: [10.1051/0004-6361/202244946](https://doi.org/10.1051/0004-6361/202244946)

Author's contributions: I led the data analysis of the CHEOPS and TESS datasets. I wrote the bulk of the text except for Sect. 3 and parts of Sects. 4.1 and 5. Except for two tables and figures, I produced all the rest of the figures and tables.

Paper II: **JWST reveals the rapid and strong day-side variability of 55 Cancri e**

Patel, J. A., Brandeker, A., Kitzmann, D., et al., 2024, *Astronomy & Astrophysics*, 690, A159.

DOI: [10.1051/0004-6361/202450748](https://doi.org/10.1051/0004-6361/202450748)

Author's contributions: I led the data reduction and analysis of the NIRCam/JWST datasets. For this purpose, I have, supervised by A. Brandeker, developed a dedicated data reduction pipeline. I wrote the bulk of the text except for Sects. 2.3, 3.2, A.2, A.3, A.4, A.6, B.1, and parts of Sect. 4.2. Except for seven figures and three tables, I produced all the rest of the figures and tables.

Paper III: **TESS phase curve of ultra-hot Jupiter WASP-189 b**

Patel, J. A., Kitzmann, D., Brandeker, A., et al., *submitted*.

Author's contributions: I designed the concept of the paper and led the TESS and CHEOPS data analysis. I wrote the bulk of the

text except for Sect. 3.2.1. Except for one figure, I produced all the rest of the figures.

Paper IV: **The geometric albedo of the hot Jupiter HD 189733 b measured with CHEOPS**

Krenn, A. F., Lendl, M., **Patel, J. A.**, et al., 2023, *Astronomy & Astrophysics*, 672, A24.

DOI: [10.1051/0004-6361/202245016](https://doi.org/10.1051/0004-6361/202245016)

Author's contributions: I led the transit light curve analysis of the CHEOPS data that produced the bulk planetary parameters. I performed an independent analysis of the CHEOPS occultation results that helped confirm the main results of the article. I wrote Sect. 3.2 and produced Fig. 2 in the article. I provided comments on the rest of the article text.

A concise summary of these papers can be found in Ch. 7. PDF copies of the papers are available at the end of this thesis. Reprints of the papers are authorised under the terms of the [Creative Commons Attribution License](#), which permits unrestricted reuse, distribution, and reproduction in any medium, provided the original work is properly cited.

The following papers are **not included** in this thesis, but are results of other projects that I contributed to during my PhD.

Paper V: **CHEOPS geometric albedo of the hot Jupiter HD 209458 b**

Brandecker, A., Heng, K., Lendl, M., et al. (including **Patel, J. A.**), 2022, *Astronomy & Astrophysics*, 659, L4.

DOI: [10.1051/0004-6361/202243082](https://doi.org/10.1051/0004-6361/202243082)

Paper VI: **Empirical limb-darkening coefficients & transit parameters of known exoplanets from TESS**

Patel, J. A. & Espinoza, N., 2022, *the Astronomical Journal*, 163, 228.

DOI: [10.3847/1538-3881/ac5f55](https://doi.org/10.3847/1538-3881/ac5f55)

Paper VII: **RVSPY - Radial Velocity Survey for Planets around Young Stars. A warm Super-Jovian companion around HD 114082, a young star with a debris disk**

Zakhozhay, O., Launhardt, R., Trifonov, T., et al. (including **Patel, J. A.**), 2022, *Astronomy & Astrophysics*, 667, A14.

DOI: [10.1051/0004-6361/202244747](https://doi.org/10.1051/0004-6361/202244747)

- Paper VIII: **RVSPY – Radial Velocity Survey for Planets around Young Stars. Target characterization and high-cadence survey**
Zakhozhay, O., Launhardt, R., Mueller, A., et al. (including *Patel, J. A.*), 2022, *Astronomy & Astrophysics*, 667, A63.
DOI: [10.1051/0004-6361/202244213](https://doi.org/10.1051/0004-6361/202244213)
- Paper IX: **55 Cancri e's occultation captured with CHEOPS**
Demory, B. -O., Sulis, S., Meier Valdes, E., et al. (including *Patel, J. A.*), 2023, *Astronomy & Astrophysics*, 669, A64.
DOI: [10.1051/0004-6361/202244894](https://doi.org/10.1051/0004-6361/202244894)
- Paper X: **Imaging of exocomets with infrared interferometry**
Janson, M., *Patel, J. A.*, Ringqvist, S. C., et al., 2023, *Astronomy & Astrophysics*, 671, A114.
DOI: [10.1051/0004-6361/202245402](https://doi.org/10.1051/0004-6361/202245402)
- Paper XI: **TESS and CHEOPS Discover Two Warm Sub-Neptunes Transiting the Bright K-dwarf HD 15906**
Tuson, A., Queloz, D., Osborn, H. P., et al. (including *Patel, J. A.*), 2023, *Monthly Notices of the Royal Astronomical Society*, 523, 3090.
DOI: [10.1093/mnras/stad1369](https://doi.org/10.1093/mnras/stad1369)
- Paper XII: **CHEOPS observations of KELT-20 b/MASCARA-2 b: an aligned orbit and signs of variability from a reflective dayside**
Singh, V., Scandariato, G., Smith, A. M. S., et al. (including *Patel, J. A.*), 2024, *Astronomy & Astrophysics*, 683, A1.
DOI: [10.1051/0004-6361/202347533](https://doi.org/10.1051/0004-6361/202347533)
- Paper XIII: **Characterisation of the TOI-421 planetary system using CHEOPS, TESS, and archival radial velocity data**
Krenn, A. F., Kubyshkina, D., Fossati, L., et al. (including *Patel, J. A.*), 2024, *Astronomy & Astrophysics*, 686, A301.
DOI: [10.1051/0004-6361/202348584](https://doi.org/10.1051/0004-6361/202348584)
- Paper XIV: **A secondary atmosphere on the rocky Exoplanet 55 Cancri e**
Hu, R., Bello-Arufe, A., Zhang, M. et al (including *Patel, J. A.*), 2024, *Nature*, 630, 609.
DOI: [10.1038/s41586-024-07432-x](https://doi.org/10.1038/s41586-024-07432-x)

Paper XV: **Characterising the atmosphere of 55 Cancri e: 1D forward model grid for current and future JWST observations**

Zilinskas, M., van Buchem, C. P. A., Zieba, S., et al. (including **Patel, J. A.**), 2025, *Astronomy & Astrophysics*, 697, A34.

DOI: [10.1051/0004-6361/202554062](https://doi.org/10.1051/0004-6361/202554062)

A note on new and reused material

The present Doctoral thesis includes some of the materials that were published elsewhere. This chapter lists all new and reused materials.

Reuse of the material from the licentiate thesis:

The current Doctoral thesis includes the material from the Licentiate thesis titled “**Exploring ultra-short-period rocky planets with space-based photometry**”, written by the same author and defended on November 11, 2024. The Licentiate thesis is available online at the DiVA portal¹.

The **Abstract** is heavily modified to reflect the changes made in the Doctoral thesis. The Swedish version of the abstract (*Sammanfattning*) is translated using a generative artificial intelligence chatbot, ChatGPT, and further edited by native Swedish speakers. The Gujarati version of the abstract (*Sārāñsh*) is translated by the author. Out of the papers included in this Doctoral thesis, only Paper I (Patel et al., 2023) was part of the Licentiate thesis.

Ch. 1 (*Introduction*) is largely reproduced from the Licentiate thesis with some additional changes to introduce new material presented in the Doctoral thesis, such as the topic of hot Jupiters. **Chs. 2** (*Transits, occultations and phase curves*) and **3** (*Observations of exoplanets*) are created out of Ch. 2 of the Licentiate thesis to accommodate new material. In particular, Sects. **2.1.1**, **2.1.2**, **2.2.1**, **2.3**, **3.2**, **3.3**, and **3.4** are written specifically for this Doctoral thesis. Other sections in **Chs. 2** and **3** are taken from the Licentiate thesis. **Ch. 4** (*Planetary internal structure*) is reproduced as it is from the Licentiate thesis. **Ch. 5** (*Ultra-short-period planets*) is taken from the Licentiate thesis with minor revisions to include updates on scientific research since then. **Ch. 6** (*Hot Jupiters*) is an en-

¹<https://urn.kb.se/resolve?urn=urn:nbn:se:su:diva-234536>

tirely new chapter written for the Doctoral thesis. Only Sect. 7.1.1 and some parts of Sect. 7.3 in Ch. 7 (*Summary and outlook*) are taken directly from the Licentiate thesis, all other sections are new. **Glossary** has been created from scratch for this Doctoral thesis.

Figures:

The source is cited in the caption for any figure taken from other publications. No source is cited when figures are original works created by the author specifically for the thesis. Even when a figure is an original work, it is possible that the data/model used to create that figure was taken from elsewhere — the source of the data/model is then cited in the caption of the figure. The source code used to generate all original figures can be found on GitHub at: <https://github.com/Jayshil/thesis-figures>.

Contents

Abstract	vii
Sammanfattning (Swedish)	ix
Sārānsh (Gujarati)	xi
List of Papers	xiii
A note on new and reused material	xvii
1 Introduction	1
2 Transits, occultations and phase curves	7
2.1 Exoplanetary transits	7
2.1.1 Departure from symmetric transits	11
2.1.2 Wavelength dependence of transit depth	12
2.2 Occultations of exoplanets	13
2.2.1 Emission spectrum of a planet	17
2.3 Phase curves	20

3	Observations of exoplanets	23
3.1	Photometric observations of exoplanets	23
3.1.1	Ultra-precision photometry with CHEOPS	26
3.2	Spectroscopic observations of exoplanets	29
3.3	The art of data analysis	34
3.3.1	Bayesian parameter estimation	36
3.3.2	Model comparison	38
3.4	Atmospheric retrieval	40
4	Planetary internal structure	41
4.1	Forward models	42
4.2	Bayesian analysis to constrain internal structure	44
5	Ultra-short-period planets	47
5.1	Formation of USPs	50
5.2	Surface and atmosphere of hot rocky planets	52
5.2.1	Global processes shaping the surface and atmosphere	52
5.2.2	Rock vapour atmospheres	55
5.2.3	Volatile-rich atmospheres	57
5.2.4	Escape and evolution of secondary atmospheres	58
6	Hot Jupiters	61
6.1	Formation mechanisms	62
6.2	Atmospheric chemistry	65
6.2.1	Ultra-hot Jupiters	66
6.2.2	Reflective properties of close-in gas giants	66
6.3	Atmospheric thermal and dynamical structure	68
7	Summary and outlook	71
7.1	Publications on USPs	72
7.1.1	Paper I: Photometric observations of TOI-561 b	72
7.1.2	Paper II: Dayside emission variability of 55 Cancri e	72
7.2	Publications on hot Jupiters	74
7.2.1	Paper III: Thermal and orbital structure of WASP-189 b	74
7.2.2	Paper IV: Reflective properties of HD 189733 b	75

7.3	Frontiers in research of close-in planets	75
	Glossary	79
	Acknowledgements	85
	References	89

1

Introduction

“It’s a wonderful thing to look at something and find it beautiful, to reflect on it and hold it fast and then to say: I’m going to draw that, and then to work on it until it’s done.”

Vincent van Gogh to his brother Theo
in a letter on April 6, 1882

THE night sky has attracted the curiosity of humans since ancient times. Even before the discovery of the telescope, humans were observing the night sky with their naked eyes. It is during this sky-gazing that they noticed the existence of planets as bright moving objects in the night sky. Many ancient civilisations were aware of the five planets apart from the Earth and Moon visible to the naked eye. This number remained unchanged until the late 18th century, when William Herschel discovered the planet Uranus. While the number of known planets remained the same, our knowledge about them, especially their motion, increased greatly in the meantime. In the 16th century, Nicolaus Copernicus published his work on the Heliocentric model, suggesting that all planets orbit the Sun. This was in stark contrast with the old and well-accepted Geocentric view of Aristotle and Ptolemy. Johannes Kepler supported and updated the Heliocentric view based on observational data from Tycho Brahe. The model was later interpreted by Sir Isaac Newton as an outcome of his laws of Gravitation.

Building upon the success of the Heliocentric model, Italian philosopher Giordano Bruno, and later Sir Isaac Newton, wondered if the other fixed stars

in the night sky have planets orbiting around them, similar to the planets around our Sun. However, the subject of planets around other stars remained much of a speculation until recently, since they are challenging to detect because of their faintness. Although there were few claims of discovery of an *Exoplanet*, as they are called, even in 19th century (e.g. [Jacob, 1855](#)), which were later turned out to be false positives, the true detection of an exoplanet had to wait until the last decade of 20th century. Then the first detection of an exoplanet came as a complete surprise as it was not discovered around a main sequence star but around a stellar remnant, a pulsar ([Wolszczan & Frail, 1992](#)). Three years later, [Mayor & Queloz \(1995\)](#) announced the discovery of a Jupiter-mass planet around a sun-like star. The newly discovered planet, 51 Pegasi b, was peculiar because, despite being a Jupiter-like planet, it orbited its host star very closely within about 4 days. That is why the equilibrium temperature of the planet is higher than 1000 K. In contrast, Jupiter in our own Solar System orbits the Sun in about 12 years and has a quite cooler temperature of 110 K.

The initial discoveries of exoplanets were significant because they not only demonstrated that planets around other stars exist but also showed that planets can exist in previously inconceivable exotic places. Furthermore, the initial success led to numerous new detections of exoplanets. Many of them were “51 Pegasi-like” planets, and many of them were even stranger than any other known planets (e.g., [Butler et al., 1997](#); [Rivera et al., 2005](#), to name a few). At the time of writing¹, the total number of confirmed exoplanets stands at 5889, and another 7576 candidates are waiting to be confirmed. It is astonishing that just within three decades of the first exoplanet discovery, we have detected more than 5000 of them. It is worth taking a moment to discuss the reason for this immense success before delving into the main subject matter of the current thesis, which is focused on observing atmospheres of several types of exoplanets.

Direct detection of an exoplanet is difficult because of the inherent faintness of the planet compared to the host star and their smaller angular separation. For example, the brightness ratio of Jupiter-Sun is about 10^{-9} at visible wavelengths and their angular separation is 5.2 arcsec and 0.52 arcsec at distances of 1 and 10 pc, respectively. Because of the difficulties involved in this method, it is responsible for detecting only a handful of planets. However, with the advent of bigger telescopes such as the *Extremely Large Telescope* (ELT), detecting and characterising nearby (< 20–50 pc) Earth-like planets would be possible. The future *Large Interferometer For Exoplanets* (LIFE) mission aims to put an array of telescopes in space and utilise interferometric techniques to characterise warm Earth-like exoplanets.

¹May 6, 2025; the numbers of confirmed exoplanets were 5616 and 3926 when I wrote my licentiate thesis (April 2024) and master’s thesis (March 2019), respectively.

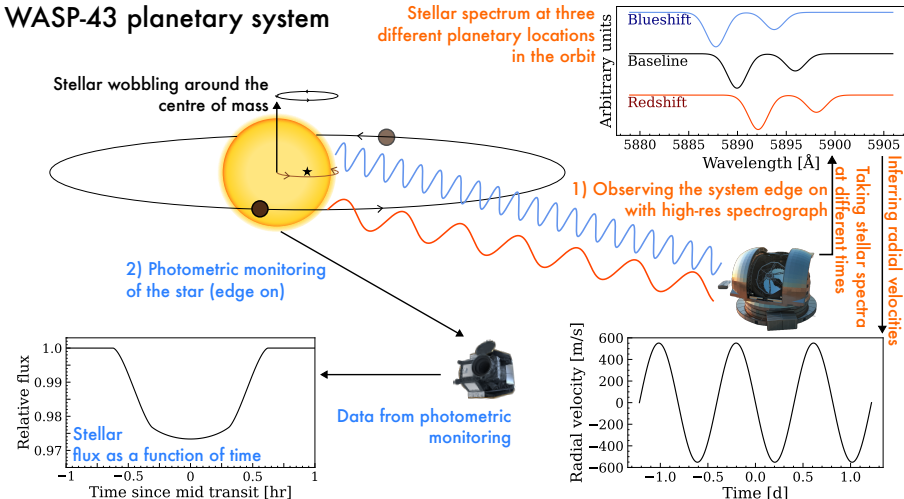


Figure 1.1: Schematic diagram of WASP-43 planetary system along with various detection methods. The planetary system, including the planetary orbit, the size of the planet and the host star, is drawn to scale, while the stellar orbit around the centre of mass of the system (shown with the ★ symbol), is exaggerated. Also shown are 1) a model of the radial velocity measurements of the star from a ground-based telescope and 2) a model of the transit of the star by the planet observed while monitoring the star photometrically. Models are created using batman and radvel (Kreidberg, 2015; Fulton et al., 2018). Planetary and stellar parameters used to generate the figure are taken from Hellier et al. (2011); Patel & Espinoza (2022).

Most of the exoplanet discoveries today are made possible by indirect detection methods. Employing these methods, we do not detect exoplanets directly but rather infer their presence based on their influence on the host stars. One of the main effects that the planet can have on its host star is gravitational perturbation on the star. In a star-planet system, all bodies, including the host star, orbit around their common centre of mass. If the system is not completely face-on, then the wobbling of the host star around the centre of mass can be seen as a periodical Doppler shift of its spectrum, as shown in Fig. 1.1. It is possible to measure this Doppler shift and derive the radial velocity (RV), i.e., velocity along the line of sight, of the host star by taking a series of stellar spectra over some time. The amplitude of the RV signal is proportional to the mass of the planet, and the period of the RV signal gives the orbital period of the planet. However, since only the radial component of the stellar velocity is measured using this method, only the minimum mass of the orbiting objects can be measured, unless the orbital inclination is known from other sources.

Jupiter and Earth mass companions typically produce RV signals on the

order of $10^2 - 10^3$ m/s and ~ 10 cm/s, respectively, depending upon the orbital period. The spectrograph needs to be very stable over a long time period to achieve a high enough signal-to-noise ratio to detect this tiny signal. While instruments such as HARPS (High Accuracy Radial velocity Planet Searcher) can reach the precision of about 1 m/s (Pepe et al., 2004), it is possible to achieve an even higher precision, on the order of several cm/s, with the new generation of spectrographs such as ESPRESSO (Echelle SPectrograph for Rocky Exoplanet and Stable Spectroscopic Observations) on the Very Large Telescope (VLT). Indeed, the ESPRESSO has been built with the aim to reach the precision of about 10 cm/s over a long time span in order to find rocky, possibly Earth-like, planets around Sun-like stars (Pepe et al., 2021).

The amplitude of the RV signal is directly proportional to the mass of the planet and inversely proportional to the square root of the semi-major axis of the orbit (Murray & Correia, 2010). Giant planets at short orbital periods (e.g., similar to WASP-43 b, which is a $1.78 M_{\text{Jup}}$ -mass planet in a 0.8 d orbit, Fig. 1.1) produce a large RV signal and thus are easier to detect. Many of the planets detected by this method, unsurprisingly, include massive giant planets on short orbital periods. On the other hand, planets at larger orbital separations are challenging to find. As we reach the regime of the smaller RV signals, signals from stellar phenomena such as magnetic cycles, active regions, stellar granulation etc. start to become important noise sources. For example, these sources would produce RV signals of the order of $10^{-2} - 10$ m/s. The strength of this signal is similar to the RV signals produced by smaller planets, or planets in wider orbits; Jupiter and Earth-like planets in 5 AU and 1 AU orbits produce 10 m/s and 10 cm/s of RV signal. The contaminating stellar signal would make it particularly difficult to detect these small RV signals. Efforts have been made to better understand the stellar RV signal by studying RV signals coming from our own Sun, where we know what should be the planetary Keplerian RV signal (e.g., Al Moulla et al., 2023).

We will now briefly introduce probably the most successful method to detect exoplanets in terms of the total number of discoveries². The transit method, as its name suggests, basically looks for transit events, i.e., when an exoplanet passes in front of the host star and causes a momentary dip in the observed stellar flux (see Fig. 1.1). For example, a Jupiter-like planet around a Sun-like star would create about a 1 % decrease in stellar flux during transit, an Earth-like planet would make an even smaller dip in stellar flux of about 0.01 %. However, even this small change in stellar flux can be detected with modern telescopes. Indeed, many surveys from the ground (e.g., SuperWASP, HATNet, Pollacco et al., 2006; Bakos et al., 2013) and space (e.g., Kepler, Koch

²https://exoplanetarchive.ipac.caltech.edu/docs/counts_detail.html

[et al.](#), 2010; [Borucki et al.](#), 2010) discovered more than 4000 exoplanets using the principles of a planetary transit. These indirect methods to detect exoplanets are one of the main reasons behind this immense success in the discovery of exoplanets in the last 30 years.

The decrease in stellar flux during a transit event is directly proportional to the planetary size. Furthermore, the detection of a planetary transit provides a way to determine orbital inclination. Coupled with minimum mass measurements from RVs, this can give the planet's true mass. Both mass and radius measurements of a planet were decisive in confirming the planetary nature of 51 Peg-like planets in the early days of the field. The discovery of a Jupiter-mass companion in a 4 d orbit raised scepticism about its planetary nature because the planetary formation theories of the time predicted that the giant planet must form in a wide orbit around its host ([Pollack et al.](#), 1996). Consequently, it was even suggested that RV signals from 51 Peg were caused not by a real planet but rather by a spectroscopic binary in a nearly face-on orbit or by an active region on the stellar surface (e.g., [Gray](#), 1997). The only way to confirm the planetary nature of the close-in giant planets was to measure their radius and true mass, which can be done with the help of the transit method. The first planet for which both mass and radius measurements were possible was HD 209458 b. After the radial velocity measurements of the star indicated the presence of a planetary-mass companion in a 3.5 d orbit ([Mazeh et al.](#), 2000), it was monitored photometrically, leading to the successful discovery of a planetary transit ([Charbonneau et al.](#), 2000). Having measured the orbital inclination using the planetary transit, [Charbonneau et al.](#) (2000) were able to derive the true mass of the planet and radius, $0.63 M_{\text{Jup}}$ and $1.27 R_{\text{Jup}}$, respectively. The mass and radius measurements of the planet not only established the planetary nature of the object but also showed that exoplanets can exist in exotic places. This example illustrates the highly complementary nature of radial velocity and transit methods to detect and characterise exoplanets.

The transit method is one of the widely used methods to detect exoplanets today. Using the same principles of planetary transit, it is also possible to study the atmosphere of the planet if there is one. Given its importance in characterising exoplanets and their atmospheres, we discuss the technique in detail in Ch. 2. We describe in Ch. 2 how we can use photometric and spectroscopic observations of transiting exoplanets to characterise their atmosphere. The space-based telescopes that can be used to obtain these observations are the subject matter of Ch. 3. We also discuss the techniques used to retrieve physical properties of planets from observations in Ch. 3.

Thanks to the modern telescopes, the field of exoplanetary science is evolving from the detection of new exoplanets to their in-depth characterisation.

For example, the precise radius measurements from the transit observations, together with the mass calculated from RVs, enable the computation of the bulk density of the planet. The bulk density provides a first estimate of the internal structure of the planet. Constructing a more detailed modelling of the planetary interior is possible based on precise mass and radius measurements as described in Ch. 4.

Among the wide variety of exoplanets known today, a particular class of them, known as ultra-short-period planets (USP), is probably the most extreme. They orbit their host star within about a day, hence the name, and have a bulk density comparable to that of rocky planets (see, e.g., [Winn et al., 2018](#)). They can have surface temperatures exceeding 2000 K because of their proximity to the host star. Consequently, their surface might be partially or completely molten, and they may even sustain a thin atmosphere made of rock vapour. Observing this rock vapour atmosphere, when possible, is the direct way to probe the interior composition of the planet. In the absence of an atmosphere on the planet, we can directly observe its surface conditions. Ch. 5 gives the details of the formation history and atmospheres of USPs.

On the other end of the size scale from USPs are the gas giants in close-in orbits around their host stars. Although they are called hot Jupiters, they are very different from the planet in our Solar system whose name they bear. The extreme radiation and the tidally locked orbit shape their atmospheric structure and chemistry. Ch. 6 describes the formation mechanism and atmospheres of hot Jupiters in detail. The bigger size of the hot Jupiters makes them comparatively easy to observe — Ch. 6 discusses how photometric and spectroscopic observations of hot Jupiters can inform us about their atmospheres.

The scientific articles included in the present thesis deal with the characterisation of several close-in planets. This includes two USPs (TOI-561 b and 55 Cnc e) and two hot Jupiters (WASP-189 b and HD 189733 b). We used space-based photometric and spectroscopic observations, obtained with the Characterising ExOPlanet Satellite (CHEOPS, [Benz et al., 2021](#)), the Transiting Exoplanet Survey Satellite (TESS, [Ricker et al., 2014](#)), and the James Webb Space Telescope (JWST, [Gardner et al., 2023](#)), to observe these planets. In a nutshell, these observations hint at the presence of secondary atmospheres on both USPs (and variability in dayside emission for 55 Cnc e). On the other hand, our observations of hot Jupiter WASP-189 b constrained its thermal structure by estimating its 2D temperature map. The optical CHEOPS observations of HD 189733 b directly observed its geometric albedo. A summary of these publications, followed by a discussion about future pathways in the research of close-in exoplanets, can be found in Ch. 7.

Transits, occultations and phase curves

“On the subject of stars, all investigations ... are ... necessarily denied to us. While we can conceive of the possibility of determining their shapes, their sizes, and their motions, we shall never be able by any means to study their chemical composition or their mineralogical structure.”

Auguste Comte in *Cours de la Philosophie Positive*, 1835

PLANETARY transits provide a unique opportunity to not only detect exoplanets but also to characterise them by measuring their radius and emitted flux. The planetary emission, either observed in a wide photometric or spectroscopic band, allows us to infer the atmospheric structure. The present chapter describes the principles of exoplanetary transits (Sect. 2.1), occultations (Sect. 2.2) and phase curves (Sect. 2.3), and how they can be used to study the atmosphere of the planet.

2.1 Exoplanetary transits

The passage of one celestial body in front of another is a quite common phenomenon as seen from Earth. The most popular among such events is the passage of the Moon or the Earth in front of the Sun or the Moon, referred

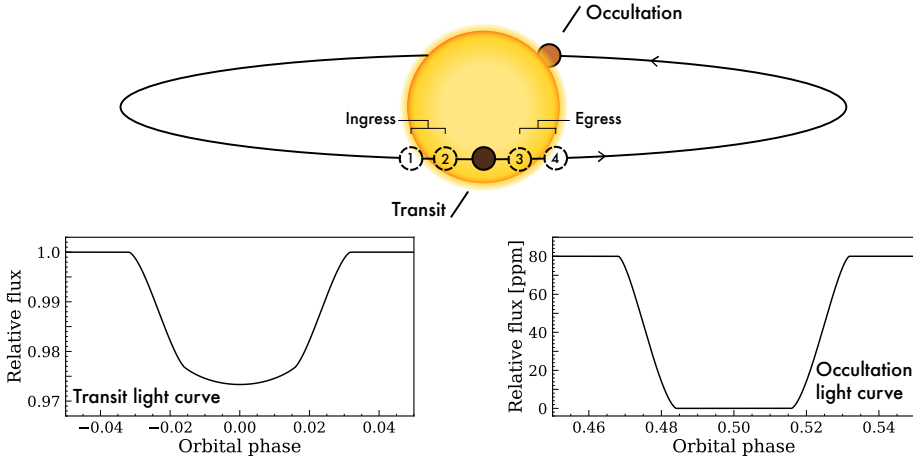


Figure 2.1: Diagram explaining the transit and occultation events using an example of WASP-43 b exoplanet. We mark the ingress and egress of the transit. All objects are drawn to scale. Plots at the bottom show the model transit and occultation light curves. The planetary and stellar parameters used to create the figure are taken from Hellier et al. (2011); Patel & Espinoza (2022); Scandariato et al. (2022). The transit and occultation light curve models are generated using batman (Kreidberg, 2015).

to as Solar and Lunar eclipses, respectively. In both events, one of the objects blocks the other. Some other scenarios are also possible when, e.g., Mercury or Venus, pass in front of the Solar disk as seen from the Earth. Since the apparent size of either of those inner planets is small compared to that of the Solar disk, they do not completely block the Sun but rather block a small amount of the light. When this happens, known as *planetary transits*, the planets could be seen as tiny black dots passing the Solar disk.

First proposed by Struve (1952), similar events could also happen with exoplanets in certain favourable cases, as shown in Fig. 2.1, e.g., when the orbit is seen edge-on from the observer's point of view. We can measure the stellar flux as a function of time, called a *transit light curve*, to search for a momentary dip in the stellar flux and thereby detect an exoplanetary transit. One example of the transit light curve for WASP-43 b system is shown in Fig. 2.1. The light blocked when an exoplanet passes in front of its host star, called *transit depth*, gives the ratio of the projected area of the planet and the star, $\Delta F = (R_p/R_\star)^2$. Here, R_p and R_\star are the planetary and stellar radii, respectively.

If multiple transits are observed continuously, the time difference between two successive transits gives the orbital period of the planet. Additionally, we can also measure the total duration and ingress/egress duration of the transit.

Here, ingress is defined as a time period between the instances when the leading and trailing limb of the planetary disk touches the stellar disk for the first time; and similarly for the egress when the planetary leading and trailing edge touches the stellar disk for the last time (see Fig. 2.1). The period, transit time, transit depth, transit duration and ingress/egress duration are the primary observables of a planetary transit. We can derive the physical parameters of the planet and its orbit from these observables.

One of the main orbital parameters that can be estimated from a transit is the orbital inclination, i.e., the angle between the planetary orbital angular momentum vector and the direction of observation. Intuitively, if the system is completely edge-on (i.e., inclination equals 90°), the planet would transit the stellar disk exactly along the diameter, giving the largest possible transit duration for a given orbital separation (i.e., semi-major axis). It turns out that combining transit depth, period, total transit duration, and ingress/egress duration can give an estimate of orbital inclination *and the scaled semi-major axis, a/R_\star* (defined as the ratio of the semi-major axis, a , and stellar radius). Moreover, the measurement of a/R_\star along with the use of Kepler's third law provides independent measurements of stellar density. The detailed derivation of these parameters from transit observables can be found in [Seager & Mallén-Ornelas \(2003\)](#); [Winn \(2010\)](#).

In practice, analytical models have been developed that compute the transit light curves given the planetary and stellar parameters. One of the popular analytic models is given by [Mandel & Agol \(2002\)](#). Researchers typically use Python implementations of analytical formulae, e.g., batman ([Kreidberg, 2015](#)), PyTransit ([Parviainen, 2015](#)), to fit observational data and subsequently derive planetary parameters from the observations (see Sect. 3.3 for details on data analysis). The derived planetary parameters from a transit observation typically include period, transit time, planet-to-star radius ratio (R_p/R_\star), scaled semi-major axis (a/R_\star) and orbital inclination. Eccentricity and argument of periastron passage can also be derived in some cases.

We cannot independently determine the planetary radius and orbital semi-major axis from the transit observations. What we can measure is their values relative to the stellar radius, i.e., R_p/R_\star and a/R_\star . We need to find R_\star from other sources to estimate R_p and a from the transit light curve. The stellar radius can be evaluated using the spectral energy distribution (SED) modelling. The SED modelling requires distance, effective temperature, surface gravity and metallicity, which can be obtained from stellar spectra modelling (see, e.g., [Persson, 2024](#), for an overview). In addition to this indirect method to measure stellar radius, other direct methods exist that use interferometric observations to measure the angular diameter of the star. Together with a distance measurement from, e.g., a parallax measured by *Gaia*, the angu-

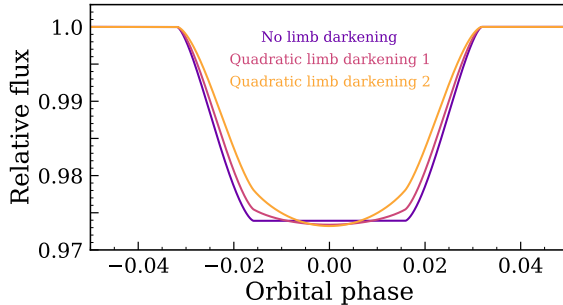


Figure 2.2: Effect of stellar limb darkening on a transit light curve. A flat-bottomed light curve displaying no limb darkening is shown in purple. The other two light curves are generated with quadratic limb darkening (LD) with different LD coefficients: $u_1 = 0.27$, $u_2 = 0.12$ (in magenta) and $u_1 = 0.85$, $u_2 = -0.14$ (in yellow). All light curves are generated using batman (Kreidberg, 2015).

lar diameter can provide an accurate estimate of the stellar radius (von Braun et al., 2011). The stellar radius is one of the largest sources of uncertainty when deriving planetary parameters.

The stellar limb darkening, an apparent decrease in stellar intensity towards the stellar limb, is another factor impacting the transit observations. This happens because of the temperature gradient in the stellar atmosphere. In the absence of limb darkening, the light blocked by the planet during a transit would remain constant throughout the planetary passage. Consequently, we should get a flat-bottomed transit light curve signifying the constant light blockage (Fig. 2.2). However, because of stellar limb darkening, the planet blocks more light near the centre of the stellar disk compared to the limb resulting in a 'U'-shaped light curve, which is what we typically observe as shown in Figs. 2.1 and 2.2. It is crucial to model the limb darkening effect on the transit light curve to estimate planetary parameters accurately. The common practice is to model the intensity distribution on the stellar disk using parametric models such as linear or quadratic polynomials or other more complex laws. The parameters of these parametric limb darkening laws are called limb darkening coefficients (LDCs). The LDCs determine the shape of the transit light curve by defining the stellar intensity profile (see Fig. 2.2). The transit light curve models from batman and PyTransit packages take LDCs to generate limb-darkened stellar disk profiles and compute transit light curves using it. Uncertainties on derived planetary parameters from transit observations also depend upon the knowledge of limb darkening (ultimately LDCs). Therefore, it is important to model LDCs properly. We can either fit for LDCs in the light curve modelling if the data precision is good enough, or we can use theoretical

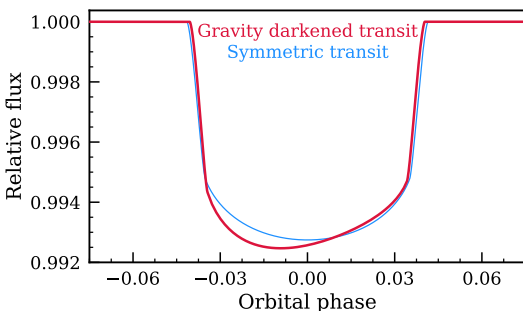


Figure 2.3: Comparison of a typical symmetric transit light curve (in blue) and a gravity darkened transit light curve (in red) for MASCARA-1 b exoplanet. The planetary and stellar parameters used to create the figure are taken from [Hooton et al. \(2022\)](#). We used batman ([Kreidberg, 2015](#)) and PyTransit ([Parviainen, 2015](#)) to generate these models.

models of stellar limb darkening to estimate LDCs theoretically ([Espinoza & Jordán, 2015](#); [Patel & Espinoza, 2022](#)).

We mentioned in Ch. 1 that the radial velocity method can only determine the minimum mass of the planet because we measure only the radial component of the stellar velocity around the centre of mass. The true mass of the planet can be measured only in cases where the orbital inclination is known. Fortunately, the transit method provides a way to compute the orbital inclination. That means that by using both methods, it is possible to measure the true mass of the planet. Additionally, the transit method gives the radius of the planet. The first approximation about the internal structure of the planet, i.e., whether the planet is rocky or gaseous, can be made by computing the bulk density of the planet from mass and radius (see Ch. 4). This is the greatest benefit of observing planets using both radial velocity and transit methods.

2.1.1 Departure from symmetric transits

The transit shape will be symmetric when a spherical planet with homogeneous absorption crosses a uniformly illuminated spherical stellar disk (e.g., Fig. 2.1). Although these assumptions usually work very well in practice, they are inaccurate in some cases. For example, the strong tidal forces of the star can deform the shape of the planet from spherical to ellipsoid. We will observe a non-symmetric transit profile when such an ellipsoidal planet transits its host star (e.g., [Barros et al., 2022](#)).

Similarly, the shape and brightness of the star can also affect the transit shape. Early-type stars are known to be rapid rotators. The resulting centrifugal force can distort the star to make it oblate, which makes the stellar equatorial radius larger compared to its polar radius. [von Zeipel \(1924\)](#) showed that the local temperature, and thus brightness, on the stellar disk would change with latitude on an oblate star because of change in local surface gravity. In

particular, the equator would appear darker than the pole. This is called gravity darkening of the star. If a planet in a misaligned orbit transits such a star, it will block the stellar disk with varying brightness. This leads to a peculiar asymmetric transit shape, such as the one shown in Fig. 2.3, which depends on the exact planetary orbit and stellar orientation (e.g., Barnes, 2009). Therefore, a careful observation and modelling of gravity darkened transit can reveal not only planetary parameters, but also the orbital architecture and 3D angle between the stellar spin and planetary orbital axes.

2.1.2 Wavelength dependence of transit depth

The transit depth is independent of wavelength to the zeroth-order approximation. However, if the planet has an atmosphere, the transit depth can change with wavelength since the atmosphere on the planet adds an additional source of wavelength-dependent opacity. As demonstrated in the top-left cartoon of Fig. 2.4, the starlight filters through the planetary atmosphere before reaching the observer during planetary transit. The planet would appear slightly bigger at wavelengths where the gases, if any, in the atmosphere absorb, making the atmosphere opaque at those wavelengths. This makes the planet's size, and therefore transit depth, wavelength-dependent. The change in the planet's transit depth (δ_{transit}) compared to the transit depth in the atmosphere-less case (R_0^2/R_\star^2), typically proportional to some multiples (n) of the isothermal scale height (H^1), is given by (e.g., Heng, 2017; Kreidberg, 2018),

$$\delta_{\text{transit}} = \frac{(R_0 + nH)^2}{R_\star^2} - \frac{R_0^2}{R_\star^2} \approx \frac{2nH}{R_0} \left(\frac{R_0}{R_\star} \right)^2 \quad (2.1)$$

Since the atmospheric scale height is directly proportional to the temperature (T) and inversely proportional to the mean molecular weight (μ) and surface gravity (g), the δ_{transit} will be maximum for hot planets with low μ , i.e., hydrogen-rich, atmospheres and small surface gravities (or, large radii). The transit signal would be maximised for planets orbiting around small stars.

Several works have developed theoretical forward models to compute wavelength-dependent transit depths, which is known as a *transmission spectrum* (e.g., Heng & Kitzmann, 2017; Mollière et al., 2017). These forward models calculate (or, sometimes, assume) the temperature structure, i.e., how temperature changes with altitude, chemical abundances, aerosol properties of the atmosphere and planetary bulk properties and finally solve radiative transfer equations using this information to compute the transmission spectrum

¹The scale height is the altitude in the atmosphere where the pressure decreases by $1/e$. It is defined as $H \equiv k_B T / \mu g$, where k_B , T , μ and g are Boltzmann's constant, temperature, mean molecular weight and surface gravity, respectively.

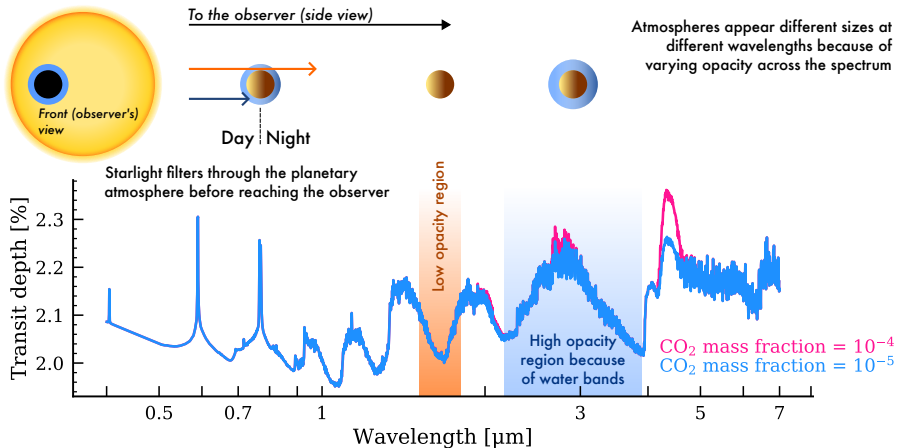


Figure 2.4: A demonstration of transmission spectroscopy. The top cartoon illustrates the basic principles of transmission spectroscopy. The bottom plot shows the model of variation in the transit depth of WASP-39 b as a function of wavelength generated using petitRADTRANS (Mollière et al., 2019).

(e.g., see Fig. 2.4). The transmission spectrum provides an opportunity to detect not only the species in the atmosphere but also their abundances. This is because the amplitude of the spectral features in the transmission spectrum is sensitive to the abundances (Fig. 2.4).

We note here that, as shown in Fig. 2.4, the atmospheric ring of the morning-evening annulus is probed during the transit. Therefore, the atmospheric properties found while observing the transmission spectrum are characteristics of that particular region on the planet.

2.2 Occultations of exoplanets

If a planet passes in front of the stellar disk during its orbit (a transit event), it is also probable that it will pass behind the star from an observer's point of view. While the planet will show its nightside during the transit, it will show the dayside when it is about to go behind the star (see Fig. 2.1). This event, called an *occultation*, gives information about the dayside of the planet: just before and after an occultation the total observed flux is the combined flux from the star and the dayside of the planet, while only the stellar flux is observed during the occultation. That means that the flux from the planet's dayside could be obtained by comparing the flux out of and during the occultation.

The relative flux change during an occultation is called the occultation depth (δ) and simply measures the ratio between the flux from the planet's dayside and stellar flux (F_p/F_*). The total emitted light from the planet consists of ther-

mal emission and reflected starlight. This gives complementary information about the planet and its atmosphere at different observing wavelengths. Planetary thermal emission dominates only at longer wavelengths because planets have lower equilibrium temperatures than their host stars. Generally, observations at longer infrared (IR) wavelengths probe thermal emission from the planet. In contrast, reflected (that is, scattered) stellar radiation would be the main source of emission from the planet at shorter wavelengths.

The occultation depth due to purely thermal emission from the planet is directly proportional to the ratio of thermal emission, that is, disk-averaged specific intensities, of the planet (I_p) and the star (I_*). Since the occultation depth measures the flux from the dayside of the planet relative to the stellar flux, it also depends upon the solid angle ratio of the planet and the star (Ω_p and Ω_*). The solid angle ratio, in turn, is directly proportional to the square of the planet-to-star radius ratio (R_p/R_*), which is accurately measured by transit observations. Assuming that both star and planet emit as a blackbody, the thermal occultation depth (δ_{th}) is defined as (when observed at long wavelengths, Winn, 2010):

$$\delta_{\text{th}}(\lambda) = \frac{F_p}{F_* + F_p} \approx \frac{F_p}{F_*} = \frac{\Omega_p}{\Omega_*} \frac{I_p}{I_*} = \left(\frac{R_p}{R_*} \right)^2 \frac{B_\lambda(T_p)}{B_\lambda(T_*)}. \quad (2.2)$$

Here F is the total emission and $B_\lambda(T)$ is the Planck function for a blackbody at temperature T as a function of wavelength (λ). The p and $*$ subscripts denote the planet and the star, respectively.

The thermal occultation depth depends on wavelength as the Planck function depends on it (see also Sect. 2.2.1). Further, in the limit of very long wavelengths, the Planck function approaches the Rayleigh-Jeans limit, in which the emission becomes directly proportional to the temperature of the blackbody at a given wavelength:

$$B_\lambda(T) \longrightarrow \frac{2c k_B T}{\lambda^4} \quad \text{when} \quad \lambda \gg \frac{hc}{k_B T}, \quad (2.3)$$

where λ is wavelength, k_B is Boltzmann's constant, c is the speed of light and h is Planck's constant. Combining Eqs. 2.2 and 2.3 gives,

$$\delta_{\text{th}} \longrightarrow \left(\frac{R_p}{R_*} \right)^2 \frac{T_p}{T_*} \quad \text{at sufficiently long wavelengths,} \quad (2.4)$$

which suggests that it is possible to estimate planetary day-side temperature (T_p) directly from the measurement of occultation depth at long IR wavelengths when the stellar temperature (T_*) is known from other sources. This temperature, calculated directly from the occultation depth measurement by assum-

ing the emission from the planet as a blackbody, is called its brightness temperature and is a relevant parameter to characterise the planet even at shorter wavelengths. The brightness temperature is measured for many planets including hot Jupiters (e.g., HD 189733 b, [Knutson et al., 2007](#)) and rocky planets (e.g., 55 Cnc e, [Demory et al., 2016a](#)) using IR observations from *Spitzer* Space Telescope (see Ch. 3, for details on the observations of exoplanets).

The measurement of an occultation depth, and dayside brightness temperature subsequently, could be useful in detecting a candidate thick atmosphere on a warm, tidally locked, rocky planet. If there is a thick atmosphere on the planet, it will transport the heat imparted on the dayside by incoming stellar radiation to its nightside. Such heat redistribution would bring down the dayside temperature of the planet. On the contrary, in the absence of heat redistribution, caused by the absence of a thick atmosphere, the dayside temperature of the planet would be significantly higher compared to the previous case. [Burrows \(2014\)](#); [Koll et al. \(2019\)](#) theoretically calculated dayside temperature in both of the cases mentioned above by computing the total incoming and outgoing energy budget of the planet. A colder observed dayside brightness temperature of the planet than the expected maximum temperature in the absence of heat re-distribution is a strong indication of the presence of heat re-distribution due to an atmosphere on the planet. [Zhang et al. \(2024\)](#) used this technique to argue that a hot sub-Earth planet, GJ 367 b is a dark, airless planet. We note here that this technique cannot identify thin atmospheres because they are inefficient in redistributing the heat to the nightside and therefore the dayside temperature would be much higher than in the thick atmosphere case. However, a thin atmosphere can host clouds that increase the planet's reflectivity. Thus, they can be identified by measuring the reflectivity of the planet ([Mansfield et al., 2019](#)). Since the surfaces of rocky planets tend to be dark (e.g. [Essack et al., 2020](#)) except for some specific cases (e.g., [Kite et al., 2016](#)), there is only a small risk of confusing reflected clouds with a reflective surface.

While IR observations of the occultation depth could provide a direct estimate of planetary dayside temperature, the same observations in the short wave provide reflective properties of the planet. Since the planet can reflect more light the larger it is, the occultation depth in this case is directly proportional to the square of the planetary radius. Since the intensity of the stellar light decreases as the inverse square of distance, the amount of reflected light also reduces in the same proportion. The occultation depth due to reflected light is defined as

$$\delta_{\text{refl}}(\lambda) = A_g(\lambda) \cdot \left(\frac{R_p}{a} \right)^2. \quad (2.5)$$

Here, A_g is the geometric albedo of the planet and is defined as the brightness of the planet compared to an illuminated isotropically scattering (i.e., Lambertian) disk at full phase at a given wavelength (e.g., [Heng, 2017](#)). The geometric albedo is *not* the fraction of scattered starlight by the atmosphere. This definition means that the geometric albedo can be > 1 in some cases. Many atmospheric and surface phenomena, including, e.g., cloud layer in the atmosphere, could contribute towards the planet's reflectivity, or scattering. [Bran-deker et al. \(2022\)](#); [Krenn et al. \(2023\)](#) recently observed two benchmark hot Jupiters, HD 209458 b and HD 189733 b, in the optical bandpass using CHEOPS (see Sect. 3.1.1) to empirically measure their geometric albedos. They found that both planets have geometric albedos ~ 0.1 , meaning that these planets appear dark when observed in the optical.

In general, when the dayside of the planet is observed at a given wavelength, the total light contributing to the occultation depth comes from both thermal emission and scattered starlight unless the observing wavelength is too long or too short. That means

$$\delta(\lambda) = \delta_{\text{th}} + \delta_{\text{refl}} = \left(\frac{R_p}{R_\star} \right)^2 \frac{B_\lambda(T_p)}{B_\lambda(T_\star)} + A_g(\lambda) \cdot \left(\frac{R_p}{a} \right)^2. \quad (2.6)$$

The exact proportion of the reflected and thermally emitted flux in the occultation depth depends upon the temperature of the planet and the observing wavelength. For example, the thermal emission could be a significant portion of the total flux even at optical wavelengths for some of the hottest planets (e.g., [Jones et al., 2022](#)). Assuming a fixed geometric albedo of 0.1, [Morris et al. \(2022\)](#) computed the fraction of reflected flux for several planets with varying equilibrium temperatures shown in Fig. 2.5. It is clear from the figure that the contribution from the thermal emission ($1 - \text{reflected flux}$) is non-zero for a vast range of wavelengths from the near ultraviolet (UV) to the mid-IR, except for some cooler planets at shorter wavelengths. What this means in practice is that the occultation depth measurements, i.e. the total dayside emission, are typically contaminated with thermally emitted flux from the planet. Therefore, if we want to measure the geometric albedo of the planet, we first need to decontaminate the occultation depth from the thermal emission. For this purpose, we use other observations at longer wavelengths to estimate the thermal contribution to the occultation depth at the given observing wavelength and then subtract this contribution from the total flux. The remaining flux, now completely reflected flux from the planet, can then be used to compute the scattering properties of the planet. [Scandariato et al. \(2022\)](#) uses this technique to measure the geometric albedo of the hot Jupiter WASP-43 b.

If it is not possible to decontaminate the occultation depth from the thermal emission, then the problem becomes degenerate, and we cannot deter-

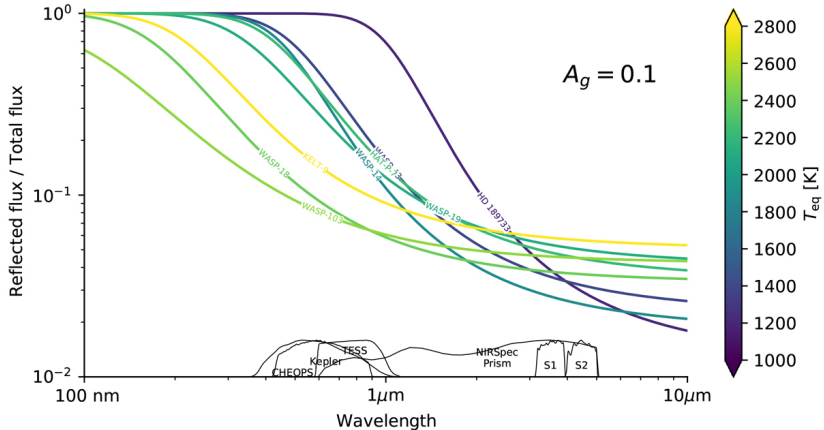


Figure 2.5: Fraction of reflected starlight from the planet as a function of wavelength for several planets assuming a fixed geometric albedo, $A_g = 0.1$. Also shown are transmission functions for some instruments including TESS and CHEOPS. The figure is adapted from [Morris et al. \(2022\)](#).

mine the geometric albedo uniquely. In other words, we cannot solve for two unknowns, the planetary temperature (T_p) and the geometric albedo (A_g), with only one equation, Eq. 2.6, assuming that other variables are known. We could make some additional assumptions, such as adopting the dayside temperature to its appropriate theoretical estimate, to lift this degeneracy. Or, we could take at least another observation at a different wavelength and assume that the geometric albedo is constant with wavelength: this would give two equations similar to Eq. 2.6 (for observed δ at two wavelengths) with two unknowns (T_p and A_g), which would then make the equations fully solvable (see, e.g., [Singh et al., 2024](#)). The assumption of wavelength independence of the geometric albedo is not accurate, however, unless the two observations are very close in wavelength.

2.2.1 Emission spectrum of a planet

The occultation depth is generally a function of wavelength since both the thermal emission and the scattering are wavelength-dependent quantities (Eq. 2.6). Since the occultation depth gives the planet-to-star flux ratio (F_p/F_*), observing an occultation depth spectrum provides a direct way to observe planetary flux (see Fig. 2.6) as long as the stellar flux is known.

The geometric albedo changes with wavelength depending on the physical properties of the material scattering the stellar light. The starlight scattering material could be a solid surface for airless rocky planets or gas/cloud particles for planets with an atmosphere. We can directly measure the reflectance spec-

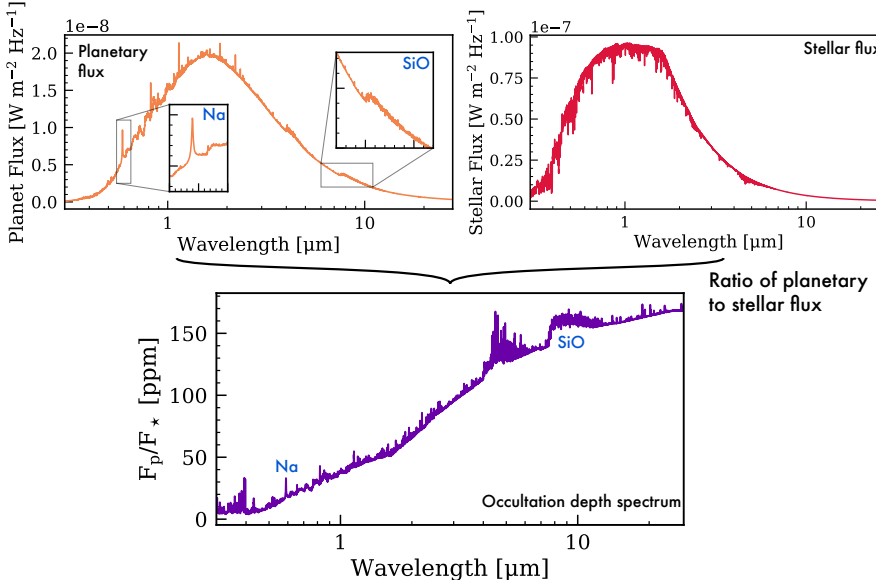


Figure 2.6: The occultation depth spectrum, shown in the bottom panel, is the ratio of planetary flux (top left) and stellar flux (top right). Observing the occultation depth spectrum, thus, constrains the planetary flux given that the stellar spectrum is known. Some of the emission lines, e.g., of Na and SiO, can be seen in both the planetary and occultation depth spectra. The planetary spectrum is of thermal origin. All of the models plotted in this figure are of TOI-561 b and are taken from [Zilinskas et al. \(2022\)](#).

trum of the planet by measuring the variation of occultation depths at shorter wavelengths, given that we know the stellar spectrum. [Hu et al. \(2012\)](#); [Paragas et al. \(2025\)](#) generated a spectral library of geometric albedo as a function of wavelength for surfaces of airless rocky planets. They showed that different material compositions and structures produce diverse reflectance spectra. Theoretically, it is possible to estimate scattering from gas/cloud particles in a planet's atmosphere. We can solve the radiative transfer equation, assuming a particular scattering law, such as Rayleigh or Mie scattering, for the planetary atmosphere, to obtain the wavelength dependence of geometric albedo (e.g., [Malik et al., 2017](#)).

Similarly, the thermal occultation depth is wavelength dependent since the Planck function is wavelength dependent (Eq. 2.2). Typically, thermal occultation depth increases with wavelength since the planetary and stellar thermal emission increases with temperature. Asymptotically, the occultation depth approaches the planet-to-star temperature ratio (Eq. 2.4). The gases in the atmosphere of the planet, or planetary surface in the case of a bare rock, emit

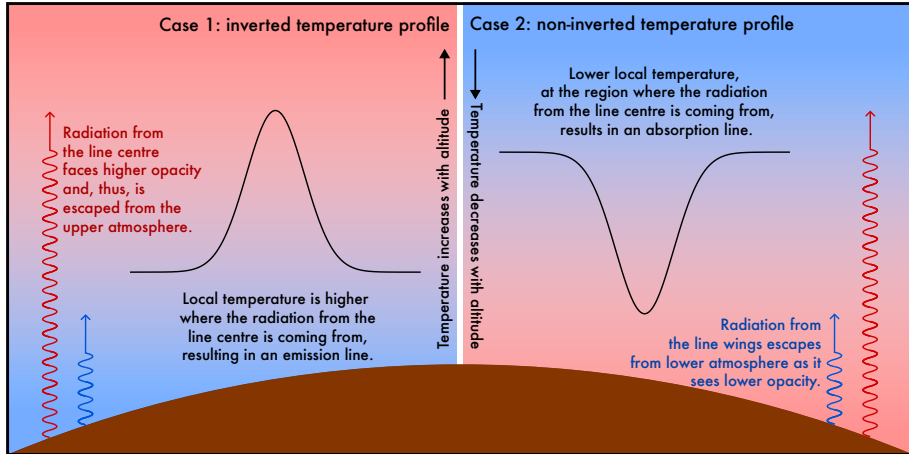


Figure 2.7: A schematic demonstrating the creation of spectral lines in two environmental conditions characterised by the thermal structure of the atmosphere. We describe the two cases with positive (left) and negative (right) temperature gradients. The temperature gradients are depicted with blue-red (cool-hot) colours. The outgoing radiation from the planet experiences varying opacities depending on its wavelength: the radiation at the line centre (red curve) sees high opacity compared to radiation at the line wings (blue curve). Therefore, the radiation at the line centre and wings escapes at higher and lower heights in the atmosphere, respectively. Depending on the local temperature at the location of escape, the lines would either appear as an emission or an absorption line.

and/or absorb at certain wavelengths, making the planetary flux deviate from the blackbody emission. The shape of the spectral features in the thermal emission spectrum, i.e., the occultation depth spectrum, can constrain the vertical thermal structure (how temperature varies with altitude) of the planetary atmosphere (see Fig. 2.7). As explained in Fig. 2.7, the inverted temperature profile (i.e., temperature increases with altitude) produces an emission line, while an absorption line means that the temperature is decreasing with altitude in the atmosphere. For example, the presence of emission lines in the occultation depth spectrum in Fig. 2.6 is a result of a temperature inversion in the atmosphere. In summary, detecting spectral features in the occultation depth spectrum not only confirms the presence of a particular species in the atmosphere, but its shape also provides the information about the thermal structure. Finally, the strength of the spectral features can constrain the chemical abundances of a given species.

It is possible to theoretically estimate the dayside emission coming from a planet by solving the radiative transfer and heat transfer equations (e.g., Heng, 2017). We also need to specify the chemical structure of the atmosphere

since it governs the opacity and optical depth, which, in turn, are required to solve the radiative transfer equation. In practice, we have to solve for the radiative transfer equation, the heat transfer equation (e.g., radiative or convective equilibrium) and the chemical structure (e.g., abundances) simultaneously to obtain the planetary flux at the top of the atmosphere (e.g., Heng et al., 2014; Malik et al., 2017). In principle, we can solve for scattering and thermal emission together to calculate the total flux emission from the planet.

Since we cannot spatially resolve the planet, the observed planetary emission spectrum would be the integrated emission spectrum from the planetary dayside.

2.3 Phase curves

While we can observe the transit and occultation during specific times (e.g., only when the planet is either passing in front of or behind the star), we can also observe the system flux throughout the full planetary orbit. We see different phases of the planet during its orbit as shown in Fig. 2.8. Since the planet does not emit uniformly at various phases, because the physical properties change throughout the planet, we should see flux variation besides the transit and occultation (see Fig. 2.8). These flux variations, called the planetary phase curve, provide a unique way to directly estimate flux emitted by different planetary hemispheres: any additional flux above the stellar flux level, which is defined by the flux observed during the occultation when we only see the star, gives planet to star flux ratio (F_p/F_\star) for the planetary hemisphere visible at the given orbital phase. In other words, we can

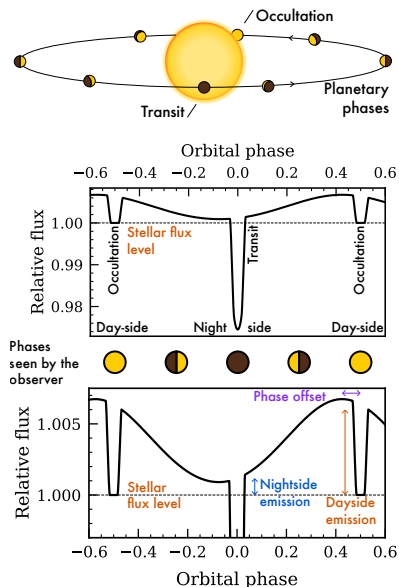


Figure 2.8: Phase curve measures the flux from different planetary hemispheres. The middle and bottom panels show the model of planetary phase curve for WASP-43 b, with the bottom panel showing a zoomed-in view of the middle panel. Planetary transits and occultations are visible. Any flux variation above the stellar flux level is caused by the planet. Cowan & Agol (2008) phase curve model and Kreidberg (2015) transit models, with planetary parameters from Scandariato et al. (2022); Bell et al. (2024), are used to generate the models.

constrain the planetary hemispherical flux variation by carefully observing the phase curve. As we cannot spatially resolve the planet, the phase curve measures the integrated flux of the visible planetary hemisphere as a function of orbital phase. For example, the excess flux above the stellar flux level at the transit and occultation gives the integrated F_p/F_\star for the planet's nightside and dayside, respectively (Fig. 2.8). Moreover, we can also measure the location of the peak phase curve amplitude, called phase offset, which should give us the location of the brightest spot on the planet (Fig. 2.8).

Similar to occultation observations, the total flux variation in phase curves contains both planetary thermal emission and reflected/scattered starlight. One or both components contribute to the total flux depending on the observed wavelength. Typically, phase curves at longer (shorter) wavelengths are dominated by the planetary thermal (scattered) emission.

We primarily observe the thermal emission from the planet at long IR wavelengths (or even at shorter wavelengths for hotter planets, Fig. 2.5). The integrated planetary flux (F_p) observed by a distant observer at a given star-planet-observer angle ($\xi \equiv -2\pi\alpha + \pi$; α is the orbital phase, which is 0 at transit and 0.5 at occultation) is given by (Cowan & Agol, 2008; Seager, 2010),

$$F_p(\xi) = \int_0^\pi \int_{-\xi-\pi/2}^{-\xi+\pi/2} I_p(\phi, \theta) \cos(\phi + \xi) \sin^2 \theta d\phi d\theta \quad (2.7)$$

Here, $I_p(\phi, \theta)$ gives the planetary intensity at a given longitude (ϕ) and latitude (θ). Normalising $F_p(\xi)$ with the stellar flux (F_\star) would give the planetary phase variation ($F_p(\xi)/F_\star$). The ϕ integration is performed over the visible hemisphere at a given orbital phase. We note that only the integration over ϕ contributes towards ξ dependence of F_p , and integration over θ adds a constant value for all ξ . Therefore, the phase curve does not contain any information about the planet's latitudinal (along θ) flux variation. What the phase curve can constrain is the integrated longitudinal flux from the planet, $J(\phi) = \int_0^\pi I_p(\phi, \theta) \sin^2 \theta d\theta$ (Cowan & Agol, 2008). Once we estimate $J(\phi)$ from $F_p(\xi)$, we can assume a certain latitudinal flux variation, e.g., sinusoidal, to obtain $I_p(\phi, \theta)$, the intensity map of the planet. Inverting the intensity map, by assuming that the planet emits as a black body, yields the temperature map, $T_p(\phi, \theta)$, of the planet. $T_p(\phi, \theta)$ is crucial in understanding the thermal properties of the atmosphere, e.g., the day-night temperature contrast, which can determine what fraction of incident heat on the dayside is transferred to the nightside (the so-called heat re-distribution efficiency). Furthermore, since we know the total power received by the planet, and $T_p(\phi, \theta)$ gives the total power radiated by the planet, we can estimate the fraction of power reflected by the planet, the so-called Bond albedo (e.g., Kempton et al., 2023).

Naturally, the phase curve variations depend on the observing wavelength

because the thermal flux from the planet changes with the wavelength. Such spectroscopic phase curves can constrain $I_p(\phi, \theta)$ as a function of wavelength, i.e., phase-resolved planetary emission spectrum. Spectroscopic phase curves provide a powerful way to constrain emission spectra of different planetary sides, such as nightside, dayside or morning-evening (see, e.g., Fig. 3.4 in Ch. 3). A careful modelling of emission spectra, and any spectral features in it, can tell us whether there are spatial inhomogeneities in the planetary atmospheres. Moreover, spectroscopic phase curves can constrain $T_p(\phi, \theta)$ as a function of wavelength, which is a proxy for height in the atmosphere since heights probed by different wavelengths vary. This means that we can determine a 2D, longitude-altitude thermal structure of the planetary atmosphere (the latitudinal structure is poorly constrained by the phase curves).

On the other hand, the flux due to scattered starlight dominates the planetary phase curve at shorter wavelengths. Mathematically, the flux scattered by a planet is (Seager, 2010),

$$F_p^{\text{scat}}(\xi) = \int_0^\pi \int_{\xi-\pi/2}^{\pi/2} I_p^{\text{scat}}(\phi, \theta) \cos(\xi - \phi) \sin^2 \theta d\phi d\theta \quad (2.8)$$

Here, $I_p^{\text{scat}}(\phi, \theta)$ is the intensity of scattered light at a given longitude (ϕ) and latitude (θ). An analytical solution for the above equation can be found for an isotropically scattering disk (i.e., Lambertian disk),

$$\frac{F_p(\xi)}{F_\star} = A_g \left(\frac{R_p}{a} \right)^2 \frac{\sin \xi + (\pi - \xi) \cos \xi}{\pi} \quad (2.9)$$

Here, A_g is the geometric albedo (see Sect. 2.2), R_p is the planetary radius, a is the semi-major axis of the orbit and ξ is the star-planet-observer phase angle. We note that the above equation reduces to Eq. 2.5 at $\xi = 0$ (i.e., at occultation) as expected. The above solution is only valid for isotropic scattering, which is not always true for scattering from natural particles. Recently, Heng et al. (2021) have derived closed-form solutions of reflected light phase curves. They basically solve the radiative transfer equation to calculate the scattered light from the planet as a function of single scattering albedo (ω) and scattering asymmetry factor (g). The single scattering albedo is defined as the fraction of incident starlight scattered by a given particle in the atmosphere. It is the physical properties of a species. g , on the other hand, gives the scattering direction with $g = 0, -1$ and 1 for isotropic, backward and forward scattering, respectively. Heng et al. (2021) phase curve formulation allows us to directly measure the single scattering albedo and phase asymmetry factor from the phase curve observations.

Observations of exoplanets

“Not until the empirical resources are exhausted, need we pass on to the dreamy realms of speculation.”

Edwin P. Hubble in *The Realm of the Nebulae*

OBSERVING a planet during a transit, an occultation, or during its entire orbit provides a wealth of information, from its bulk properties to its atmospheric structure. While a transit signal from a large planet is detectable even from low-precision observations, high precision is required to observe tiny occultation and phase curve signals. Fortunately, such ultra-high precision is possible to achieve with modern telescopes. Unsurprisingly, the transit method is one of the primary methods to detect and characterise an exoplanet and its atmosphere. In this chapter, we review the photometric (Sect. 3.1) and spectroscopic (Sect. 3.2) techniques to observe exoplanets. We will also discuss the space-based telescopes used to obtain these observations. We finally explore the data analysis schemes used in retrieving physical properties of planets from the observations (Sects. 3.3 and 3.4).

3.1 Photometric observations of exoplanets

Photometric observations of light curves, or time variations of stellar flux, also called time-series photometry, are straightforward to get, especially with modern detectors. We need multiple stellar flux observations in one transit/occultation duration to accurately measure the flux variation during the

event, which is possible with modern detectors made with charged-coupled devices (CCDs). CCDs work on the principles of the photoelectric effect to convert incident photons into electrons that are then recorded with negligible loss by accompanying electronics. Most modern telescopes exploit the capabilities of CCDs to record precise high-cadence time-series photometry.

Transits of a planet could cause as large as 1% flux dimming that can be detected even from a small facility on the ground. There are many dedicated telescopes to detect planets from the ground. Although observing a transit is simple, finding a good target star is difficult because a small fraction of stars would have planets orbiting them with a geometry appropriate for a transit event. Since the geometric transit probability, defined by R_*/a ([Borucki & Summers, 1984](#)), varies inversely with the semi-major axis (a) and thus is very low for many planets (for instance, it is 0.0046 for the Earth), we need to observe many stars before finding a transit signal. That is why wide-angle surveys are designed that can observe hundreds of stars simultaneously for months. Some of such wide-angle surveys are WASP (Wide-Angle Search for Planets, [Pollacco et al., 2006](#)) and HATNet (The Hungarian Automated Telescope Network, [Bakos et al., 2013](#)) that collectively are responsible for the bulk of the discoveries of transiting planets from the ground. Both of these surveys have small telescopes ($\sim 10\text{--}20$ cm) with a wide field of view, with which they can observe hundreds of stars over a couple of months. The list is not exhaustive; many surveys are in operation (or were operated), covering a large fraction of the sky.

Typical planets discovered in transit surveys are giant Jupiter-like planets on shorter orbits. The bias for close-in orbits is because of their larger transit probability and generally small observing baseline required for detection. Additionally, bigger transit signals produced by giant planets simplify detecting them. The noise from the turbulent atmosphere limits the smallest signal detected from the ground. Except for the polar regions, observing continuously from the ground is impossible because of the day-night cycle; bad weather could impact the observations. Altogether, it is beneficial to observe from space to achieve precise, stable and long uninterrupted photometry required to discover smaller planets and planets in wide orbits. With stable and precise photometry from space, it has been possible to detect an occultation event that could be on the order of several tens to hundreds of ppm. Three dedicated space-based missions have been launched until now to survey the sky in search of transiting exoplanets: CoRoT (Convection, Rotation and planetary Transits; [Auvergne et al., 2009](#)), Kepler/K2 ([Koch et al., 2010](#); [Borucki et al., 2010](#)) and TESS (the Transiting Exoplanet Survey Satellite; [Ricker et al., 2014](#)).

TESS is unique among them as it surveys almost the whole sky to obtain time-series photometry. The nearby bright stars are chosen as the main tar-

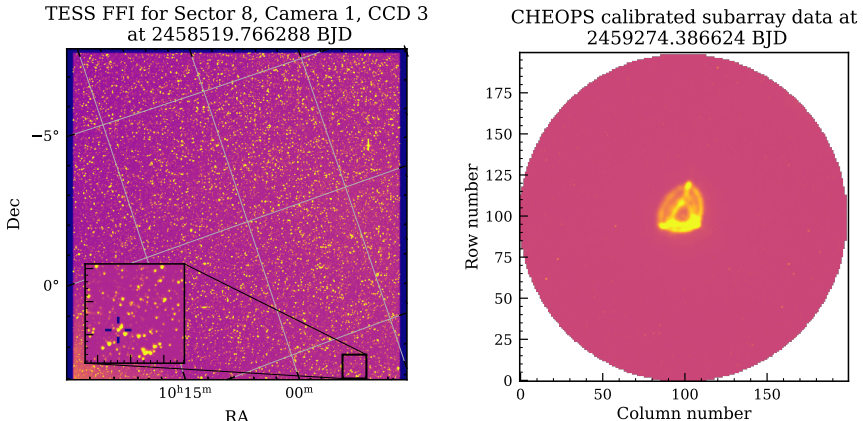


Figure 3.1: Example photometric data at a given timestamp from TESS (left panel) and CHEOPS (right panel). (Left) The data are the full frame image (FFI) from one of the CCDs in one of the TESS cameras. The inset image shows the zoomed-in region that contains the star TOI-561, the location of which is marked. (Right) CHEOPS subarray displaying a typical CHEOPS PSF from the photometric observations of the star TOI-561. The required data are taken from the Mikulski Archive for Space Telescopes (MAST) and the CHEOPS archive.

gets for TESS as they are easier to follow up with ground-based radial velocity observations. TESS has four identical wide-field cameras, each with an aperture of 105 mm and a field-of-view (FOV) of $24^\circ \times 24^\circ$ spread over four CCDs. With four cameras, it can cover a large portion of the sky, with the FOV of $24^\circ \times 96^\circ$, during a given observation. A typical observation run, called a sector, lasts for 27.4 days, during which it obtains photometry every 2 min for all targets from the TESS input catalogue (TIC). After the completion of one sector, TESS re-orients its position in the sky to a different area and continues observing. Being a wide-angle satellite, it can observe several thousands of stars simultaneously in an observing sector: an example of a snapshot of a whole CCD at a given time, shown in Fig. 3.1, clearly illustrates this point. Such a strategy of observing multiple stars simultaneously is an effective strategy for discovering planets. The TESS data reduction pipeline (called, Pre-search Data Conditioning Simple Aperture Photometry, or PDC-SAP, [Smith et al., 2012; Stumpe et al., 2014; Jenkins et al., 2016](#)) derives time-series light curves from the observed data using the technique of aperture photometry, i.e., summing up the total flux counts in the aperture. Since its launch in 2018, TESS has discovered 545 planets, while more than 7000 candidates are waiting to be confirmed.

The main target stars for TESS are the bright nearby stars (within 200 parsecs) that are easier to follow up for further studies. A majority of nearby stars

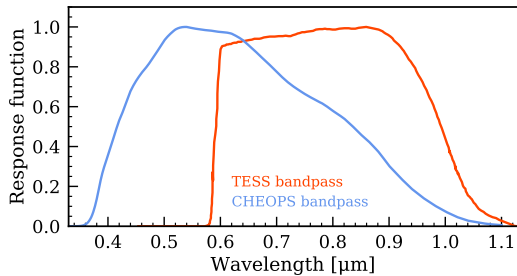


Figure 3.2: Peak-normalised response functions of TESS and CHEOPS. It is clearly seen that the TESS bandpass is more sensitive at redder wavelengths compared to CHEOPS.

are cooler M-dwarfs, therefore, the TESS bandpass (shown in Fig. 3.2) is more sensitive towards redder wavelengths. TESS can achieve a photometric precision (measured as Combined Differential Photometric Precision – CDPP) of 230 ppm in 1 hour at 10th mag. This precision is sufficient to detect small rocky planets in transit if they have orbital periods short enough to be observed multiple times. However, it falls short of measuring tiny signals, such as individual transits of small rocky planets or occultation signals with a good signal-to-noise ratio. A dedicated telescope is needed for follow-up observations to measure smaller signals precisely. Characterising ExOPlanet Satellite, or CHEOPS, was launched by the European Space Agency (ESA) with this exact goal. TESS has another limitation in observing long-period planets: it can only observe a given target for about 28 days, so it likely misses planets with a longer orbital period. The upcoming space mission PLATO (PLAnetary Transits and Oscillations of stars; [Rauer et al., 2014](#)) will fulfil this need by observing bright stars for an extended time (on the order of a year).

3.1.1 Ultra-precision photometry with CHEOPS

CHEOPS is an S-class mission launched by ESA to perform precise transit follow-up observations to characterise exoplanets ([Benz et al., 2021](#)). One of the scientific requirements of CHEOPS is to provide stable, ultra-precision photometry with 20 ppm precision in 6 hr for bright stars ($6 < V < 9$ mag) and 85 ppm in 3 hr for faint stars up to $V = 12$ mag. These specifications were derived from science requirements of detecting a transit of an Earth and Neptune-like planets around a G5 and K dwarfs, respectively, with a signal-to-noise ratio of at least 5 ([Benz et al., 2021](#)). Its design and orbit were chosen to fulfil these criteria: the telescope, which has Ritchey-Chrétien optical design with 320 mm primary mirror, revolves the Earth in Sun-synchronous nadir-locked orbit to reduce stray light and enable radiator cooling to deep space. CHEOPS’ bandpass, shown in Fig. 3.2, is centred at around $0.6 \mu\text{m}$ in the optical, where G–K dwarfs have peak emission. The CHEOPS point spread function (PSF, see

Fig. 3.1) is deliberately defocused to mitigate the saturation while observing bright targets and to reduce pointing jitter. Indeed, the in-flight performance showed that CHEOPS could achieve a precision of 30 and 12 ppm in 1 and 6 hrs respectively for bright stars with $V \leq 9$ mag, while 96 ppm in 3 hr for faint stars with $V < 12$ mag, that too with extreme pointing stability of less than $1''$ (Fortier et al., 2024). Fortier et al. (2024) further showed that the observations of the bright stars are photon-noise limited, and other noise sources start to dominate only at the faint end.

Although the size of CHEOPS' detector CCD is 1024×1024 pix, the full frame CCD data are only downlinked at the start of a visit. Afterwards, to save the bandwidth, only 200×200 pix CCD subsections centred on the target location, called a subarray, are downloaded if the exposure time is longer than 30 s. In case of shorter exposure times, images are co-added pixel-by-pixel before downloading until the total integration time becomes longer than 30 s. To compensate for the information loss caused by stacking images, circular cropped images of subarrays with a radius of 30 pix are generated before co-adding. Such cropped images, called imagettes, which have shorter original exposure times, are also downlinked. CHEOPS data products and how they are generated are illustrated in Fig. 3.3. After downlinking, the subarrays are analysed using the official CHEOPS Data Reduction Pipeline (DRP, Hoyer et al., 2020) to produce light curves using aperture photometry, which simply sums up the total flux inside the aperture to extract the light curves.

As the CHEOPS orbits the Earth in a nadir-locked orbit, the field of view rotates around the target. This will produce the roll angle dependence of the flux as the background changes with time – this dependence can be observed as a repeating pattern in the light curve produced by the DRP for the case shown in the top right panel of Fig. 3.3. This DRP light curve is dominated by the extra noise in this case, especially because of the crowded background. Similarly, the DRP performance is not optimal for faint stars where other noise sources dominate the total noise budget. PSF photometry, which models the CHEOPS PSF (Fig. 3.1) and uses this model to measure the flux changes efficiently, could be beneficial in those cases. Light curves from PSF photometry, produced by an open-source package PIPE (PSF Imagette Photometric Extraction, Brandeker et al., 2024), indeed have shown to produce better precision than those from the DRP for faint stars (Fortier et al., 2024). In Fig. 3.3, we compare the light curves produced by the DRP and PIPE, and it is clearly visible that PIPE does a better job in taking care of roll angle modulation. PIPE surpasses the DRP in one more aspect of producing photometry from the imagettes, which the DRP cannot. As the imagettes are collected at the original shorter exposure time without any stacking, the resultant photometry better samples the light curve than the subarray photometry.

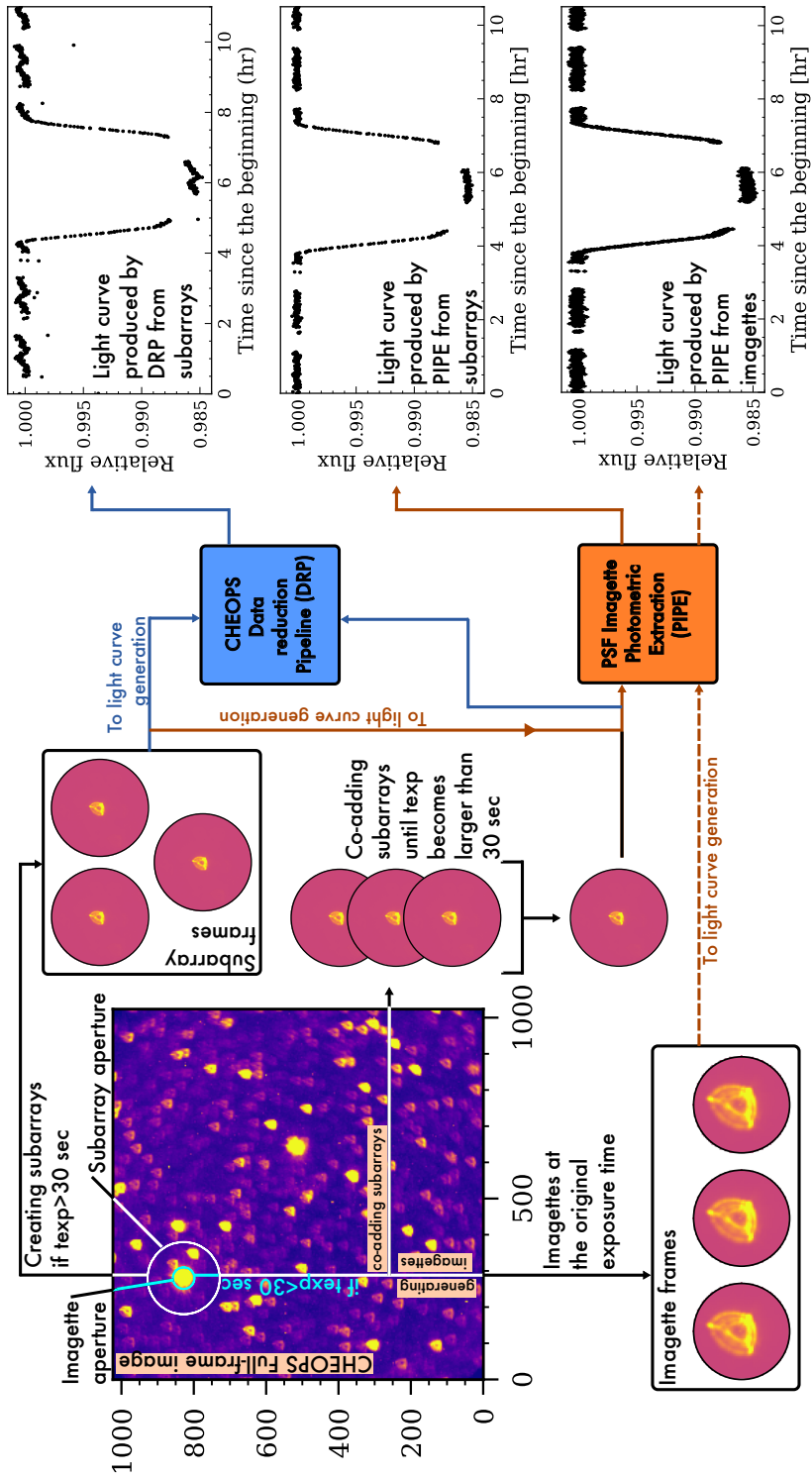


Figure 3.3: A diagram explaining the generation of various CHEOPS data products (see the text for more details). We also show the light curves produced by different data products and from two data reduction pipelines. The light curve data is a transit of planet KELT-20 b published in [Singh et al. \(2024\)](#). As CHEOPS is in a low-Earth orbit, sometimes observations are interrupted for a few minutes when the Earth eclipses the target. These events create data gaps in the light curves.

CHEOPS has already started producing exceptional results aided by its ultra-high precision photometry. Some of its significant findings include the measurement of the optical geometric albedo of two hot Jupiters HD 208458 b and HD 189733 b (Brandeker et al., 2022; Krenn et al., 2023), detection of asymmetric transit of WASP-189 b because of gravity darkening (Lendl et al., 2020; Deline et al., 2022), the discovery of TOI-178 planetary systems in which planets are in Laplace resonance chain (Leleu et al., 2021), the discovery glory effect in the atmosphere of WASP-76 b because of morning clouds (Demangeon et al., 2024) etc. CHEOPS is continuing to advance exoplanetary science with the approval of its extended mission until the end of 2026 and the potential for a second extension until the end of 2029.

3.2 Spectroscopic observations of exoplanets

Observing a planetary transit or occultation with photometric telescopes provides observations in wide photometric bands. While such photometric observations are still important to constrain the physical properties of planets, spectroscopic observations, e.g., transmission or emission spectra, of exoplanets are needed for their in-depth characterisation. As a first step towards this, we can observe the planet in multiple photometric bands covering different wavelength ranges. Such observations can be treated as a very low-resolution spectrum in the absence of other truly spectroscopic observations. Such photometric observations often give first-order information regarding the planet's atmosphere.

CHEOPS and TESS bandpasses, while overlapping for a range of wavelengths, are sensitive to slightly different wavelengths (see Fig. 3.2). CHEOPS is more sensitive to bluer wavelengths than TESS. We know that the scattering processes, such as Rayleigh scattering, are stronger towards bluer wavelengths. Therefore, any larger-than-expected difference in occultation depth between TESS and CHEOPS bandpasses can be attributed to the scattering processes. Similarly, if the planet is hot enough such that we mainly see thermal emission in both TESS and CHEOPS bandpasses, the occultation depths in these bandpasses would follow the planetary blackbody curve, which would be useful in determining the temperature of the planet. *Spitzer* Space Telescope had several photometric bands, among them, two were centred at 3.5 and $4.5\text{ }\mu\text{m}$. The latter is situated at the centre of the CO₂ spectral band, while the former is in the wings. A significantly deeper transit of WASP-39 b was observed at $4.5\text{ }\mu\text{m}$ compared to the transit at $3.5\text{ }\mu\text{m}$, leading Wakeford et al. (2018) to suggest that the deeper $4.5\text{ }\mu\text{m}$ transit was due to the presence of CO₂ in the planetary atmosphere. This was later confirmed by the transmission spectrum of WASP-39 b obtained by the *James Webb* Space Telescope (JWST)

Transiting Exoplanet Community Early Release Science Team et al., 2023).

We ideally want a high-resolution transit/occultation depth spectrum instead of transit/occultation measurements in sparse photometric bands for a thorough atmospheric characterisation. What we can do is, instead of observing time variation in stellar flux (light curves) in photometric bands, observe how the whole stellar spectrum changes with time. Such stellar spectral time series observations (TSOs), depicted and explained in Fig. 3.4, essentially observe light curves for the full wavelength range covered by the stellar spectrum. As a result, we get light curves at multiple wavelengths, which are known as spectroscopic light curves (see Fig. 3.4). We can recover the wavelength dependence of transit/occultation depths by modelling spectroscopic light curves.

Prior to the launch of the *James Webb Space Telescope* (JWST), the *Hubble Space Telescope* (HST) and the *Spitzer Space Telescope* were the main workhorses of spectroscopic observations of transiting exoplanets from space. *Spitzer*, which is no longer operational, had two photometric bands from its Infrared Array Camera (IRAC) centred at 3.5 and 4.5 μm (see Fig. 3.5). As previously mentioned, observing planetary transits with IRAC/*Spitzer* helped constrain the atmospheric structure in some cases (e.g., Wakeford et al., 2018). Furthermore, since we primarily observe thermal emission at longer wavelengths, the thermal emission at these wavelengths can measure the dayside temperature of the planet (see Sect. 2.2). The spectroscopic modes of *Spitzer* were not widely utilised for exoplanet science, except in a few cases (Grillmair et al., 2008).

HST, on the other hand, has spectroscopic capabilities. HST, with the help of the Space Telescope Imaging Spectrograph (STIS) and Wide Field Camera 3 (WFC3) instruments, can provide spectroscopic observations from ultraviolet (UV) to near-infrared (NIR). In particular, the NIR grisms G102 and G141 on HST cover the spectral range where water molecules have a strong opacity (see Fig. 3.5). Both instruments are widely used to observe transiting exoplanets, which resulted in the detection of H_2O in the atmospheres of many exoplanets (see Kreidberg, 2018; Madhusudhan, 2019, for a review).

While HST was instrumental in studying the chemical and thermal structure of transiting exoplanet atmospheres via detecting the H_2O feature in transmission and emission, it is limited by its wavelength coverage and precision. For example, it is not possible to detect carbon-bearing molecules, e.g., CO, CO_2 , CH_4 , in planetary atmospheres because those molecules mainly have strong spectral bands in NIR beyond 2 μm , which is longer than what HST can observe. Moreover, a lower resolution of its instruments (e.g., the resolving power of G102 and G141 grisms is about 210 and 130, respectively¹) means that we cannot observe narrow spectral features with HST. Although several

¹<https://www.stsci.edu/hst/instrumentation/wfc3/documentation/grism-resources>

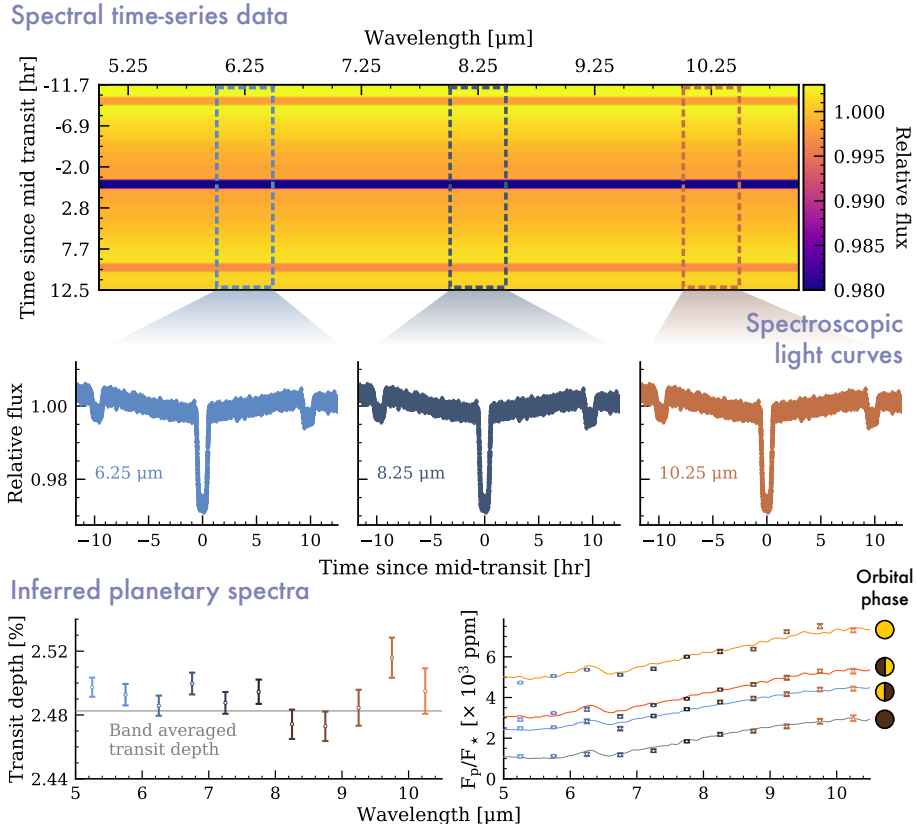


Figure 3.4: The process of recovering planetary spectra from spectral time-series observations. We demonstrate this using spectroscopic phase observations of WASP-43 b obtained by the Mid-Infrared Instrument (MIRI) onboard JWST as a part of the JWST Transiting Exoplanet Community Early Release Science program (PID 1366). We first observe stellar spectra, between $5\text{--}12\,\mu\text{m}$ with MIRI/JWST in this case, continuously throughout the whole planetary orbit. The top panel plots stellar spectral time series, which shows how the stellar spectrum (shown on a horizontal line) changes with time (vertical axis). We note that the overall stellar flux through the whole wavelength range decreases during a transit and occultations, as expected. This decrement left its marks as horizontal bands on a 2D spectral time series, clearly visible in the top panel. We can recover the spectroscopic phase curve at a given wavelength by measuring how stellar flux changes with time at that wavelength. Although we only show the spectroscopic light curves at three arbitrary wavelengths in the middle panel, they can be extracted for the whole wavelength range, in principle. We can model spectroscopic light curves to retrieve the transit spectrum (bottom left) and F_p/F_\star spectra (bottom right): how transits and F_p/F_\star change with wavelength. Since these are phase curve observations, we can find F_p/F_\star spectra at various planetary phases. The data and model shown here are taken from Bell et al. (2024); Espinoza & Perrin (2025).

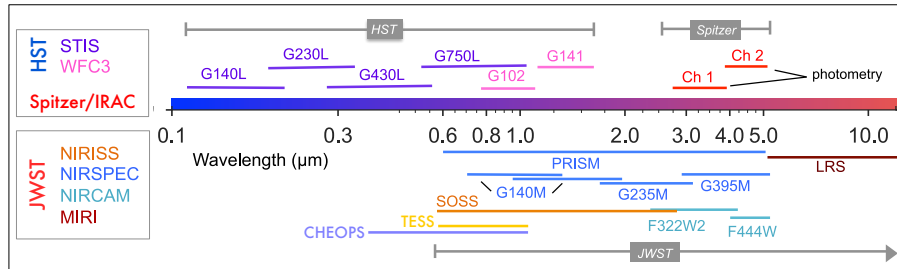


Figure 3.5: Wavelength coverage of main photometric and spectroscopic space-based telescopes that can be used to observe transiting exoplanets. A full panchromatic planetary spectrum from $0.1 \mu\text{m}$ - $12 \mu\text{m}$ can be observed by utilising several instruments on board HST and JWST. The figure is adapted and modified from Kreidberg (2018).

instruments on STIS have high-resolution observing models, they are in the UV and optical, where not many molecules have spectral features (however, see [Ehrenreich et al., 2015](#)). At the same time, a comparatively smaller mirror size of HST restricts the smallest precision that we can obtain.

The recently launched *James Webb* Space Telescope (JWST) has an advantage over HST and other previous telescopes in terms of better precision, long-term stability and a wider wavelength coverage. The primary mirror of JWST has a diameter of about 6.5 m with a collecting area roughly 5 times bigger than that of HST. This helps JWST to achieve superior precision. The JWST commissioning observations with G395H grism on Near Infrared Spectrograph (NIR-Spec) have shown pointing jitter of about 1/500:th of a pixel (0.2 mas) over 6 hr ([Espinoza et al., 2023](#)). Such an exquisite pointing stability reduces the additional instrumental systematics, which, in turn, is useful in obtaining better precision on observables. Finally, a suite of instruments on board JWST collectively covers wavelengths from about 0.6–28 μm (see Fig. 3.5). We can acquire spectroscopic time series observations (i.e., spectroscopic transit light curves, etc.) for this wavelength range. This wide wavelength range not only covers H_2O bands in the NIR, but also contains spectral bands of several carbon (CO, CO_2 , CH_4), sulphur (SO_2 , H_2S), silicon (SiO , SiO_2) and even nitrogen (NH_3) bearing molecules. A wide wavelength coverage is extremely useful in not only detecting chemical species in the atmosphere but also in constraining chemical abundances. The JWST has already demonstrated its capability in characterising exoplanetary atmospheres: the Early Release Science (ERS) observations of transmission spectra of hot Saturn WASP-39 b revealed the presence of H_2O , CO, CO_2 and SO_2 in its atmosphere ([Carter et al., 2024](#)). The SO_2 in the atmosphere is thought to be produced by photochemical reaction, which is the

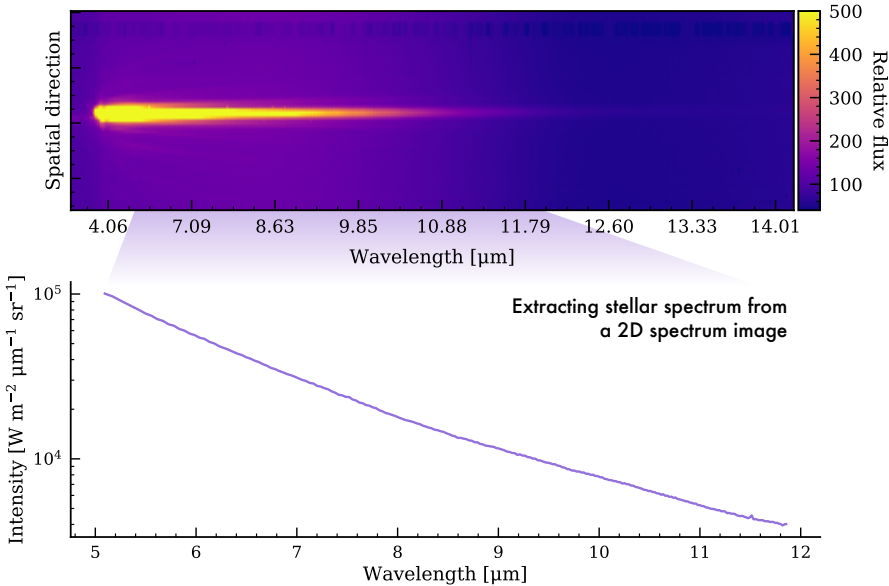


Figure 3.6: A raw JWST observation of a 2D spectral trace is shown in the top panel. The wavelength increases along the x-axis (the dispersion direction), while the y-axis is the spatial, or cross-dispersion, direction. The stellar PSF at a given wavelength spreads across multiple pixels, giving a finite, non-zero width to the spectral trace. The extracted 1D stellar spectrum, wavelength vs intensity, is shown in the bottom panel. The 2D spectrum data shown here was obtained as part of WASP-43 b phase curve observations obtained with MIRI/JWST as a part of JWST ERS program (PID 1366) and extracted using an open source package stark ([Patel et al., 2024](#)).

first evidence of photochemistry in an exoplanet atmosphere (e.g., [Tsai et al., 2023](#)). The JWST has even detected silicate clouds in a hot Jupiter-like planet and in a warm Neptune-like planet ([Grant et al., 2023; Dyrek et al., 2024](#)).

As mentioned previously, we observe the stellar spectrum with time during spectroscopic observations of transiting exoplanets. The precision obtained on final transit/occultation depths depends a lot on the precision of the stellar spectrum. Therefore, it is crucial to robustly extract stellar spectra from raw observations. JWST (or other telescopes that can observe spectra) observes stellar spectrum as a 2D image, with a dispersion (i.e., wavelength) direction and a cross-dispersion direction, as shown in the top panel of Fig. 3.6. The stellar PSF typically extends across several pixels along the cross-dispersion (or spatial) direction for a given wavelength. We can simply sum up the total flux in the stellar PSF for every wavelength to compute how much stellar intensity changes with wavelength, or stellar spectrum, in other words. This pro-

cedure, which is akin to aperture photometry, is, thus, called aperture spectral extraction. However, aperture extraction is often not the optimal method to extract stellar spectrum from the raw 2D spectral image. This is because aperture extraction gives equal weight to pixels in the centre and wings of the stellar PSF. Moreover, it is hard to detect and remove outliers, e.g., produced by cosmic rays or hot pixels, from the data. Therefore, several methods have been developed to optimally extract stellar spectra from 2D spectral images (e.g., Horne, 1986; Marsh, 1989). The idea is to model the stellar PSF and then use the modelled PSF to measure the flux changes along the wavelength axis. For example, the underlying algorithm in the stark package uses splines to fit the stellar PSF, and how it changes wavelength, and then uses the estimated PSF to extract the stellar spectrum. Since we have an estimate of how stellar PSF should behave, it is fairly straightforward to identify and remove outliers. Once we extracted the stellar spectrum for the 2D spectral image, we can find the spectroscopic light curves as explained in Fig. 3.4 and perform the data analysis as discussed below (Sect. 3.3) to find planetary parameters.

3.3 The art of data analysis

Retrieving planetary parameters, such as transit depth, occultation depth, or their spectra, from raw photometric or spectroscopic observations is a two-part process. In the first part, we reduce the raw observations to obtain light curves (time variations of stellar flux), which is described in previous sections and summarised in Figs. 3.3, 3.6 and 3.4 for CHEOPS and JWST observations. Once we have light curves, we want to model them in order to estimate planetary parameters. In simple words, we want to fit an appropriate model to the data (this is commonly also referred to as *data analysis*).

To do this, we must first develop a model that we can use to fit the data. A complete model should include the astrophysical signal from the planet and the star, and any additional systematics because of the telescope instrument (see Fig. 3.7). The planetary model can be either a transit/occultation model or a phase curve model. The models for transit and occultation signals have been developed by Mandel & Agol (2002), as previously mentioned. Similarly, Cowan & Agol (2008); Heng et al. (2021) have developed analytical models for phase curve observations. These models take planetary parameters and compute a transit/occultation/phase curve model using these parameters. In addition to the planetary model, we need a model to account for stellar flux variations. In our discussion until now, we have implicitly assumed that the flux from the star remains constant during the observations. However, this may not be the case in practice (e.g., Deline et al., 2022): the stellar flux can change because of, e.g., star spots, granulations, etc. The stellar flux variations be-

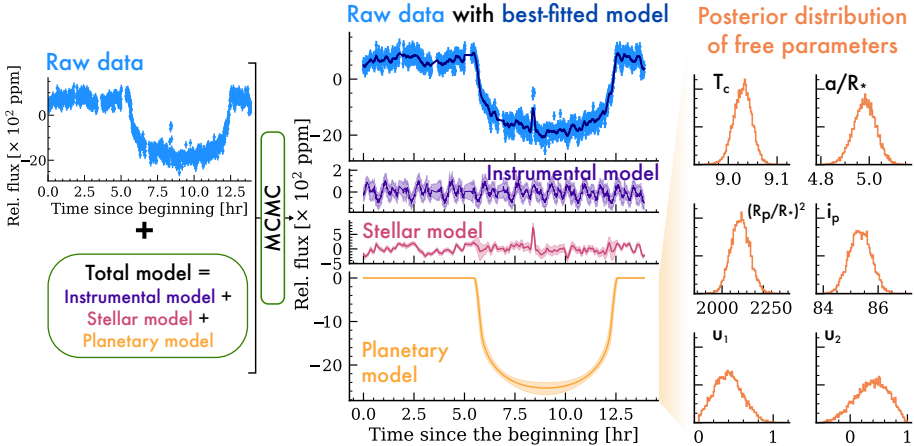


Figure 3.7: A diagram illustrating the data analysis and its products. The raw data (transit of KELT-11 b observed by CHEOPS; top left) is usually fitted with a model containing an instrumental, stellar and planetary model, using Bayesian techniques such as MCMC. The middle panel shows the total fitted model (dark blue) in the first row of the middle panel. The constituent models of the total model, instrumental, stellar and planetary models, are shown in the second, third and fourth rows of the middle panels (solid coloured lines). The shaded region around the solid coloured lines shows the uncertainty in the fitted models. The right panel shows the posterior probability distribution of free planetary parameters, transit time (T_c), scaled semi-major axis (a/R_*), transit depth ($(R_p/R_*)^2$), orbital inclination (i_p), and limb darkening coefficients for the quadratic law (u_1 and u_2). The transit light curve data is downloaded from the CHEOPS archive and is published in Benz et al. (2021). The modelling is performed using an open-source Python tool, juliet (Espinoza et al., 2019).

cause of the activity are usually stochastic in nature, and no closed-form analytical model exists for them. We typically use similar stochastic processes, such as the so-called Gaussian processes (GPs), to model stellar activity in the observations (see Rasmussen & Williams, 2006, for details). Finally, we need a model to describe instrumental systematics. The instrumental model depends on the instrument at hand, but generally, it can be very well described by linear functions of telescope housekeeping parameters. For example, the roll-angle modulation in the case of CHEOPS observations (Sect. 3.1.1) can be modelled by a combination of sinusoidal functions of roll angle (e.g., Deline et al., 2022). The effect of stellar and instrumental signals is clearly visible in out-of-transit flux variations in the raw transit light curve of KELT-11 b observed by CHEOPS and shown in Fig. 3.7.

Once we have defined the total model, consisting of planetary, stellar and instrumental models, we are ready to fit it to the observational data. Each

component of the total model — planetary, stellar, and instrumental models — has its own set of parameters. These parameters together create an N-dimensional parameter space. Our goal when fitting a model to the observational data is to find a set of model parameters such that the resulting total model can best explain the observed data. The simplest way to do this is by minimising χ^2 -statistic:

$$\chi^2 = \sum_{i=1}^n \frac{(y_{i,\text{obs}} - y_{i,\text{model}})^2}{y_{i,\text{errors}}^2} \quad (3.1)$$

Here, $y_{i,\text{obs}}$ and $y_{i,\text{model}}$ are the i^{th} observed data point and model prediction, and $y_{i,\text{errors}}^2$ is the errorbars on i^{th} -observation. We can numerically explore the parameter space to find the minimum value of χ^2 . The corresponding model would best explain the observed data. Several numerical algorithms, such as the Levenberg–Marquardt algorithm or gradient descent, have been developed to minimise the χ^2 -statistic. While such algorithms may work in a simple problem, they are not robust when the models are non-linear and have degeneracies. Furthermore, χ^2 minimisation cannot give us proper uncertainties on the planetary parameters. In practice, we usually resort to Bayesian probabilistic parameter estimation.

3.3.1 Bayesian parameter estimation

Since we don't have the *complete* information about how the planet, the star or even the instrument would behave during an observation, our knowledge of observables becomes necessarily probabilistic. This means that we can only calculate the probability distribution of model parameters given the observations. This distribution, however, gives the complete information of a parameter, including expected value and the range of values a parameter can take, given the observations. We can use the parameter estimation technique from Bayesian statistics to retrieve the probability distribution of model parameters from observations. According to Bayes' theorem,

$$\mathbb{P}(\theta|D, I) = \frac{\mathbb{P}(\theta|I) \cdot \mathbb{P}(D|\theta, I)}{\mathbb{P}(D|I)} \quad (3.2)$$

Here, θ is the vector of all model parameters (i.e., *all* planetary, stellar, and instrumental parameters) that we want to constrain using the new observational data (D), given any prior information (I) on those parameters. The Bayes' theorem provides a way to compute desired *posterior* probability distribution of the model parameters, $\mathbb{P}(\theta|D, I)$, given the data and prior information. The term in the denominator of the right-hand side of above equation, $\mathbb{P}(D|I)$, is called the marginal likelihood and serves as a normalisation factor to ensure

that $\int \mathbb{P}(\theta|D,I) d\theta = 1$ (i.e., the joint probability distribution of all model parameters is normalised to 1). Integrating both sides of Eq. 3.2 over θ and setting the result to 1 would yield $\mathbb{P}(D|I) \equiv \int \mathbb{P}(\theta|I) \cdot \mathbb{P}(D|\theta,I) d\theta$ (e.g., [Gregory, 2005](#)). Omitting the normalisation factor in Eq. 3.2,

$$\mathbb{P}(\theta|D,I) \propto \mathbb{P}(\theta|I) \cdot \mathbb{P}(D|\theta,I) \quad (3.3)$$

The first term on the right-hand side of the equation, $\mathbb{P}(\theta|I)$, describes the probability distribution of the model parameters (θ) given the previous information (I). This probability distribution, known as the prior distribution, encodes our knowledge (or ignorance) of model parameters *before* getting the new observational data. The second term on the right-hand side of the above equation, $\mathbb{P}(D|\theta,I)$, is called the likelihood function. The likelihood function gives the probability of obtaining the data given the assumed model computed with a set of parameters (θ) and prior information. It essentially tells how well the model prediction can explain the observations given a set of parameters under certain prior information. The Bayes' theorem (Eq. 3.3) states that the posterior probability distribution is proportional to the multiplication of prior and likelihood. The Bayes' theorem simply outlines the learning process in which we use the likelihood function to update our knowledge of model parameters from prior information to compute the posteriors.

We need to assign probability distributions to both the prior and likelihood in order to use Bayes' theorem to find the posterior probability distribution of model parameters. The prior probability distribution, $\mathbb{P}(\theta|I)$, can be provided based on our prior knowledge of θ . For example, suppose previous works have constrained a planetary parameter. In that case, we can provide a normal distribution with mean and standard deviation based on its values from past research as a prior distribution of that parameter (informative priors). Sometimes, past observations don't give enough information about a parameter. We can then specify uninformative or weakly informative priors, such as a uniform distribution in the parameter's theoretically expected range. Similarly, we want to designate a probability distribution for the likelihood function. Since the likelihood function is defined as the probability of obtaining data (D) given the model parameters (θ), it should describe the distribution of data around the predicted model location, computed with θ . The observational data, in turn, is distributed according to the nature of the uncertainties in observations. Thus, the nature of uncertainty determines the form of the likelihood. In many scenarios in astronomy, this would be a normal (Gaussian) distribution, however, it can take other forms as well.

Once we have assigned probability distributions to the prior and likelihood, we can use the Bayes' theorem (Eq. 3.3) to estimate the posterior probability distribution of model parameters. This, however, is easier said than

done, primarily because it is almost impossible to calculate the posterior distribution analytically. We need to use numerical methods to determine the posterior distribution of model parameters. Typically, we use some Markov Chain Monte Carlo (MCMC) methods to draw samples directly from the right-hand side of Bayes' theorem (Eq. 3.3)—if we draw large enough samples, they will approximately describe the posterior distribution of model parameters (i.e., left-hand side of Bayes' theorem; Eq. 3.3). This process is called the posterior sampling, or, simply, sampling. One of the simplest of MCMC algorithms is the Metropolis-Hastings algorithm ([Metropolis et al., 1953](#); [Hastings, 1970](#)), in which a chain of random samples is drawn from the target probability distribution (right-hand side of the Bayes' theorem, in our case). While the Metropolis-Hastings algorithm would work for simple problems, it will take too long to sample from a complicated, multimodal distribution. Other more efficient algorithms, e.g., affine invariant MCMC ([Goodman & Weare, 2010](#)), Hamiltonian Monte Carlo ([Neal, 2011](#)), nested sampling ([Skilling, 2004, 2006](#); [Higson et al., 2019](#)), have been developed to robustly perform posterior sampling. In practice, we typically use the Python implementations (e.g., [Hoffman & Gelman, 2011](#); [Foreman-Mackey et al., 2013](#); [Speagle, 2020](#)) of the above algorithms to perform posterior sampling and thus, model fitting. Fig. 3.7 demonstrates a typical model fitting procedure where we fit a transit model to the transit light curve of KELT-11 b observed by CHEOPS: upon analysing the data, we not only find posterior probability distributions of model parameters (right panel in Fig. 3.7), but also the corresponding uncertainties in the estimated model prediction (shaded region in the middle pane of Fig. 3.7). The posterior probability distribution of planetary parameters can tell us the most probable value and range of expected values (e.g., standard deviation from the median value) of all parameters, based on the given observational data.

3.3.2 Model comparison

One of the advantages of using Bayesian methods to analyse the data is that we can naturally compare competing models to find out which of them is the most supported by the observational data. Suppose we have observed a light curve and we now want to check whether we have detected a transit signal from a new planet, or if we have detected an occultation signal in the dataset or not. When the signal is small, we cannot just visually inspect the dataset to claim whether we have detected the signal we were looking for—we want a statistical measure for this. Bayesian statistics provide us with tools to exactly do this. Using Bayes' theorem,

$$\mathbb{P}(M_i|D, I) = \frac{\mathbb{P}(M_i|I) \cdot \mathbb{P}(D|M_i, I)}{\mathbb{P}(D|I)} \quad (3.4)$$

Here, $\mathbb{P}(M_i|D, I)$ is the probability of i^{th} model (M_i) being true given the observed data (D) under certain prior assumptions (I). $\mathbb{P}(M_i|I)$, $\mathbb{P}(D|M_i, I)$, and $\mathbb{P}(D|I)$ are the prior probability, likelihood function, and marginal likelihood for M_i , respectively, as described in Sect. 3.3.1.

Suppose we want to test which of the two models, M_1 and M_2 , is supported by the data (for instance, M_1 : no planetary occultation signal in the data, and M_2 : detection of a significant occultation signal). We can statistically compare the probabilities of either M_1 or M_2 being true using Eq. 3.4 as,

$$\frac{\mathbb{P}(M_2|D, I)}{\mathbb{P}(M_1|D, I)} = \frac{\mathbb{P}(M_2|I) \cdot \mathbb{P}(D|M_2, I)}{\mathbb{P}(M_1|I) \cdot \mathbb{P}(D|M_1, I)} \quad (3.5)$$

Typically, before the observations, we have no way to prefer either model over the other. That means the prior probability of both models is equal, $\mathbb{P}(M_1|I) = \mathbb{P}(M_2|I)$, which would simplify the above equation to,

$$\frac{\mathbb{P}(M_2|D, I)}{\mathbb{P}(M_1|D, I)} = \frac{\mathbb{P}(D|M_2, I)}{\mathbb{P}(D|M_1, I)} \quad (3.6)$$

This ratio on the right side of the above equation is popularly known as the Bayes factor (B_{21}) of two competing models, M_2 and M_1 . B_{21} encodes all necessary information required for Bayesian model comparison; $B_{21} > 1$ means that $\mathbb{P}(M_2|D, I) > \mathbb{P}(M_1|D, I)$, implying that M_2 is statistically favoured by the observational data. The absolute value of B_{21} gives how significantly one of the models is favoured by the data.

We have to compute $\mathbb{P}(D|M_j, I)$ for both models to calculate the Bayes factor. In this calculation, we need to remember that both models have their own sets of parameters (θ_j ; in our example, M_2 have a non-zero occultation depth, while M_1 has occultation depth fixed to zero to show that there is no occultation). The computation of $\mathbb{P}(D|M_j, I)$ must somehow account for uncertainties in θ_j , which is given by $\mathbb{P}(\theta_j|D, M_j, I)$. Using the law of total probability²,

$$\mathbb{P}(D|M_j, I) = \int \mathbb{P}(\theta|M_j, I) \cdot \mathbb{P}(D|\theta, M_j, I) d\theta \quad (3.7)$$

This is exactly the definition of marginal likelihood as defined in Sect. 3.3.1. At that time, we were only dealing with one model, so M_j was implicitly a part of I . In the context of model comparison, however, we need to explicitly mention the assumed model. The integration in Eq. 3.7, sometimes also known as Bayesian evidence, is non-trivial to calculate. However, some of the algorithms developed for posterior sampling also compute the Bayesian evidence during the sampling process (e.g., Skilling, 2004). The Bayesian evidence, in turn, can be used to compute the Bayes factor, and thus can be used for model

² $\mathbb{P}(A|C) = \int \mathbb{P}(B|C) \cdot \mathbb{P}(A|B, C) dB$

comparison. Among mutually competing models, the model with the highest Bayesian evidence is said to be preferred most by the data at hand. We note here that we can only find a relative comparison of competing models and not an absolute comparison.

3.4 Atmospheric retrieval

The primary observables of transiting planet light curves are transit or occultation depths or their spectra, in the case of photometric and spectroscopic observations. While photometric transit/occultation depths can be directly used to infer atmospheric properties (e.g., planetary size, temperature), the spectroscopic depths cannot be used as they are to deduce the physical properties of the planet. We need to fit a model again to the transit/occultation depth spectra to detect chemical species, their abundances, or the thermal structure of the atmosphere. As discussed in Sects. 2.1.2 and 2.2.1, models have been developed to compute the transmission/emission spectra of a planet as a function of chemical abundances, temperature-pressure profile, etc.

We can use the Bayesian parameter estimation techniques (Sect. 3.3.1) to fit the theoretical planetary spectra to the observed ones. As a result, we can find the chemical abundances, their ratios and even temperature-pressure profiles (Powell et al., 2024; Evans-Soma et al., 2025). Bayesian model comparison (Sect. 3.3.2) can be used to determine whether the planetary spectra contain spectral features of a species by statistically comparing two models with and without the spectral features of that species (e.g., Patel et al., 2024).

4

Planetary internal structure

“I had,” said he, “come to an entirely erroneous conclusion which shows, my dear Watson, how dangerous it always is to reason from insufficient data.”

Sherlock Holmes in *The Adventure of the Speckled Band* by Sir Arthur Conan Doyle

ESTIMATING the bulk density of the planet provides a first-order estimate of the internal structure of the planet. For instance, a very low bulk density would imply the presence of a thick atmospheric envelope, probably made up of H/He, on the planet, while a higher bulk density would mean a primarily rocky composition. Planetary mass and radius measurements, which are needed to compute bulk density, could be made by observing the planet using the radial velocity method (see, Ch. 1, for a review) and the transit method (see Ch. 2). Unfortunately, additional *in situ* observations that are possible for the Solar System planets, e.g., measuring the gravity field to constrain internal structure, are not possible for exoplanets. The atmospheric composition of a planet, when it can be observed, can provide additional information regarding the structure of the planet. As mass and radius are the most important observables that determine the internal structure of a planet, we want to measure them with extreme precision. We want to estimate the planetary radius more precisely because the bulk density depends on the inverse third power of the radius. Therefore, even a small uncertainty in

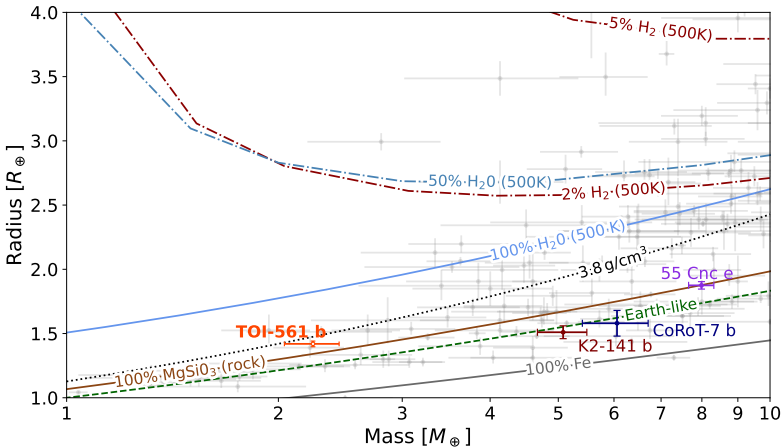


Figure 4.1: The mass-radius diagram, showing the population of low-mass ($< 10M_{\oplus}$), small ($< 4R_{\oplus}$) exoplanets in mass-radius space, taken from Patel et al. (2023). We also plot the theoretical models for various chemical compositions from Zeng et al. (2019). We overplot the location of several USPs, TOI-561 b, 55 Cnc e, K2-141 b and CoRoT-7 b.

the radius measurement could propagate to a large uncertainty in the density estimate. CHEOPS, with its ultra-precision photometric observations, would prove crucial in this respect as it can measure the planet's radius very precisely. Indeed, CHEOPS has been instrumental in characterising the internal structure of many planets by providing ultra-precise measurements of their radius (e.g., Leleu et al., 2021; Bourrier et al., 2022).

In the present chapter, we will first discuss the forward models of the internal structure of rocky planets in Sect. 4.1. In Sect. 4.2, we will describe how these forward models can be used to fit the observational data in order to estimate the most probable internal structure.

4.1 Forward models

Given the total mass and the chemical composition of a planet, it is possible to compute its radius based on this. We can compare these forward models to the observed radius of a planet to understand its internal structure. For example, Fig. 4.1 shows the forward models computed using several chemical compositions for a range of mass and radius. The models are usually idealised models generated for, e.g., 100% iron or 100% water composition. Fig. 4.1 compares the forward models to the observed population of the planet. The location of

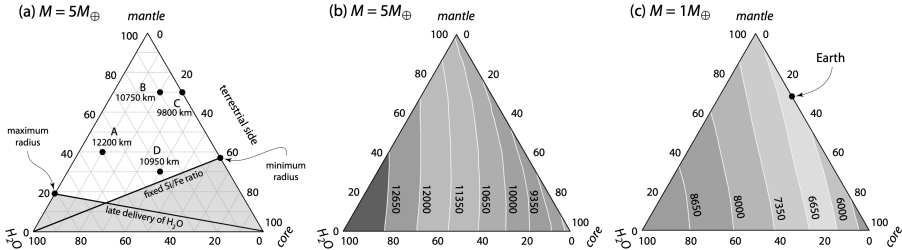


Figure 4.2: Ternary diagrams showing the radius predicted by forward models with arbitrary fractions of Fe core, silicate mantle and water layer for planets with two masses as taken from [Valencia et al. \(2007\)](#); [Perryman \(2018\)](#). Each component, core, mantle and water, is represented by a vortex in a triangle. The vortex gives a planet with 100% fraction of that component while the opposite side is the composition with 0% fraction of the element. The parallel lines in between give the increasing fraction of the element from the side to the vortex. The left panel gives the estimated radius for a planet with $5M_{\oplus}$ mass for several arbitrary compositions. The middle and right panels show the iso-radius curves for planets with $5M_{\oplus}$ and $1M_{\oplus}$ mass.

a given planet, e.g., K2-141 b, near one of the models, the Earth-like composition model in this case, indicates the internal structure. However, the scope of these models is limited since the exact composition of the planet would be far from the ideal ones presented in Fig. 4.1.

The forward models are computed by solving the structure equations similar to the ones used to find a stellar structure. These equations are the ones of the hydrostatic equilibrium, mass and energy conservation and thermodynamic equilibrium. The equations can be written as (see, e.g., [Perryman, 2018](#), for a review):

$$\begin{aligned} \frac{\partial P}{\partial r} &= -\rho g \\ \frac{\partial M}{\partial r} &= 4\pi r^2 \rho \\ \frac{\partial L}{\partial r} &= 4\pi r^2 \rho \left(\dot{\varepsilon} - T \frac{\partial S}{\partial t} \right) \\ \frac{\partial T}{\partial r} &= \frac{\partial P}{\partial r} \frac{T}{P} \frac{d \ln T}{d \ln P} \end{aligned} \quad (4.1)$$

Here, P , M , L , T , r , ρ , g , $\dot{\varepsilon}$ and S are the pressure, mass, intrinsic luminosity, temperature, radius, density, gravity, the energy produced and the entropy per unit mass, respectively.

The four coupled differential equations can be solved in conjunction with

other information, such as the equation of state. The equation of state relates the state variables, pressure (P), temperature (T) and density (ρ), with each other. Although Eqs. 4.1 are similar to the stellar structure equations, the planets differ from stars in one aspect. While the stars can be treated as isolated objects, we need to take into account the stellar radiation incoming onto the planets. This is usually done by adding a term to the temperature of the planet as stellar radiation mainly increases its temperature.

[Valencia et al. \(2007\)](#) computed forward models for a planet with three components: an iron core, a silicate mantle and a water layer. The estimated radius for these models for two planetary masses, $5 M_{\oplus}$ and $1 M_{\oplus}$, is shown in Fig. 4.2 in the form of ternary diagrams. The middle and right panels of Fig. 4.2, which show the iso-radius curves for different models, illustrate that the internal structure models are not unique. For example, there is a degeneracy in radius between a model with iron core + H_2O envelope and a pure silicate mantle. One way to solve the degeneracy is by assuming the elemental abundance ratio from, e.g., atmospheric characterisation or fixing it to the stellar value (e.g., [Dorn et al., 2015](#)). While the models by [Valencia et al. \(2007\)](#) only assume a three-component planet, some other works model a more complex structure, e.g., with a thick hydrogen atmosphere ([Dorn et al., 2017](#)) or even interior-atmosphere joint modelling ([Acuña et al., 2023](#)). [Boley et al. \(2023\)](#) studied the impact of magma oceans on the bulk density of a USP planet and showed that indeed the presence of a magma ocean can change the bulk density compared to a complete solid planet. An in-depth discussion of the internal structure models is beyond the scope of the present work, but can be found in the references mentioned above.

4.2 Bayesian analysis to constrain internal structure

The forward models calculate the radius of the planet given its mass and internal composition. However, we are more interested in the reverse problem, i.e., given the observed mass and radius of the planet, we want to estimate its internal structure. [Dorn et al. \(2017\)](#) developed a full probabilistic Bayesian analysis technique to infer the internal composition of the planet from observations. They take the data of i) observed radius and mass (main observables), ii) bulk Fe, Mg, and Si abundances (can be fixed to their corresponding stellar values) and iii) semi-major axis, stellar radius and effective temperature (from transit and stellar spectrum analysis). The data is then ‘fitted’ using appropriate forward models. The forward model developed by [Dorn et al. \(2017\)](#) for super-Earths is a four-layer planet with a Fe core, Si-Mg mantle, water envelope and a thin atmosphere.

Typically an iterative Markov Chain Monte Carlo (MCMC) method is em-

ployed to estimate the posteriors of model parameters. These may include mass fractions of the core, mantle, water layer and atmosphere and mantle elemental composition in the case of [Dorn et al. \(2017\)](#) models. The method is successfully implemented in several works to estimate the internal structure of the planet (e.g., [Leleu et al., 2021](#); [Patel et al., 2023](#)).

5

Ultra-short-period planets

*Na hi ekayā drṣṭya samyamgam
nirvarnam nirvahati* — No single view
can claim to describe it all adequately.

Abhinavagupta in his commentary on
Anandwardhana's *Dhwanyaloka*

DISCOVERY of planets outside our Solar System answered many unsolved questions of planetary science. At the same time, these discoveries uncovered many surprises. This includes the detections of planets at very short orbital distances: a population study of known exoplanets, e.g., in period-radius space shown in Fig. 5.1, revealed a whole new class of small ($< 2\text{-}3 R_{\oplus}$) planets at short orbital periods (even < 1 d). They are referred to as the ultra-short period planets (USPs) because of the very short orbital period. Mass determinations USPs (e.g., Léger et al., 2009; Batalha et al., 2011) showed that they have high mean densities consistent with a rocky composition. Thanks to the proximity to their host star, the substellar temperature on their dayside could easily reach 2000 K or more for many of them. This led researchers to suggest that the surface of these planets could be molten and may host a lava ocean (hence the name lava-ocean planets, Léger et al., 2011). Various formation mechanisms for USPs are discussed in Sect. 5.1. Although much of their atmosphere is thought to be stripped away because of intense stellar irradiation, they could still sustain a thin secondary atmosphere. The atmospheres of USPs, and the variety of surfaces they may have, are further discussed in Sect. 5.2.

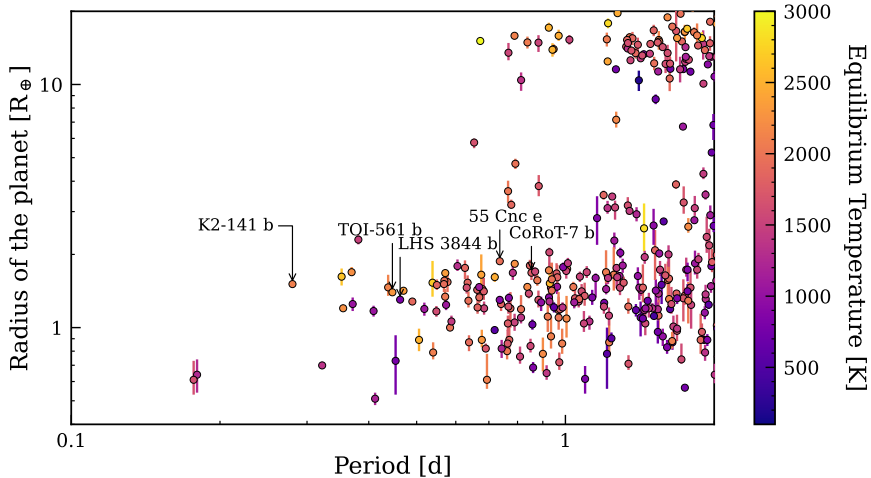


Figure 5.1: Population of all known planets with $R_p \leq 20 R_\oplus$ and $P \leq 2$ d, covering the population of USPs. Some of the popular USPs are annotated in the figure. The data, which is retrieved from the NASA Exoplanet Archive on May 6, 2025, is colour-coded according to the equilibrium temperature of the planet ([NASA Exoplanet Archive, 2024](#)).

The *Kepler* space telescope was instrumental in detecting USPs – [Sanchis-Ojeda et al. \(2014\)](#) compiled a list of more than 100 USP candidates from *Kepler* data. This, however, does not mean that USPs are more common types of planets. They are just easier to detect using the transit method because the method itself is biased towards planets on shorter orbits. Moreover, small signals from USPs are easier to detect with space-based high-precision telescopes rather than from the ground, which resolves why space telescopes like *Kepler* discovered many USPs while very few are detected from the ground. [Sanchis-Ojeda et al. \(2014\)](#) analysed the *Kepler* data available until then to search for USPs and found 106 candidates. They performed simulations based on their survey results to estimate the actual occurrence rate of USPs, that is, a fraction of stars hosting at least one USP (see [Petigura et al., 2013](#), for more details), which is computed by dividing the total number of USP hosts by the total number of stars. They found that 0.5% of G-dwarfs, 0.83% of K-dwarfs and 1.10% of M-dwarfs should be the USP hosts. This occurrence rate is similar to that of hot Jupiters with an orbital period of less than 10 days. [Sanchis-Ojeda et al. \(2014\)](#) further computed the occurrence rate as a function of orbital period and planet radius, which is shown in Fig. 5.2. The fraction of USP host stars decreases with decreasing orbital period and with increasing planetary radius. The reason for the former is simply that USPs cannot survive too near to their

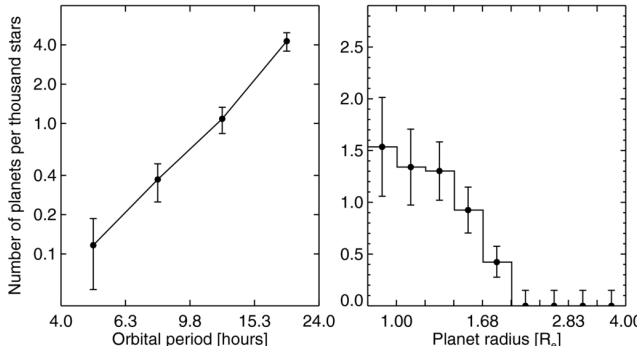


Figure 5.2: Occurrence rate of the population of USPs as a function of orbital period and planetary radius. The figure is adapted from Sanchis-Ojeda et al. (2014).

host stars without being destroyed by the tidal forces, while the scarcity of USPs with radii larger than $\sim 2 R_{\oplus}$ is the photoevaporation (see also, Sect. 5.1). Both of these points are also clearly imprinted upon the current population of exoplanets shown in Fig. 5.1.

Even more extreme among the class of USPs are the disintegrating exoplanets. *Kepler*/K2 detected many of such planets. Such systems were identified in the data by their peculiar asymmetric transit shape – significantly longer egress time than ingress time – and possibly variable transit depth (e.g., Rappaport et al., 2012). This signal contrasts with the regular, symmetric signal, shown in Fig. 2.1, observed for typical planets. Rappaport et al. (2012) suggested that the asymmetric and variable transit could be caused by a small, Mercury-like planet losing its mass because of either evaporation or volcanism on the surface and subsequent escape into the circumstellar environment. The escaped material, mainly composed of dust and gas from the planet, forms a comet-like tail in the circumstellar environment, responsible for the asymmetric transit shape. Spectroscopic observations of such a comet-like tail from a disintegrating planet could identify chemical species, which, in turn, can provide clues on the composition of planetary interiors. Tusay et al. (2025) have observed transmission spectra of a disintegrating planet, K2-22 b, with MIRI/JWST. These spectroscopic observations suggest a hint of magnesium silicate minerals and possibly some gaseous species like NO and/or CO₂, suggesting a silicate mantle. If confirmed, these detections would be immensely helpful in determining the internal structure of rocky planets. A handful of disintegrating planets were discovered with *Kepler* (e.g., Rappaport et al., 2012, 2014; Brogi et al., 2012; Sanchis-Ojeda et al., 2015), while with the TESS mission, we are expected to find more of them. Indeed, TESS has recently identified a disintegrating planet around a K-dwarf host BD+05 4868 A by detecting asymmetric variable transits in its TESS light curves (Hon et al., 2025). Based on the TESS observations, Hon et al. (2025) were able to constrain the grain size of 1–10 μm and mass-loss rate of $10 M_{\oplus} \text{ Gyr}^{-1}$. The planet is scheduled

for spectroscopic observations with MIRI/JWST, which should be able to constrain the composition of the planetary interior.

5.1 Formation of USPs

One of the first questions asked upon the discoveries of the first USPs was regarding their formation. Some of the initial studies, e.g., [Jackson et al. \(2013\)](#); [Valsecchi et al. \(2014\)](#), suggested that hot Jupiters are progenitors of the USPs. A hot Jupiter that migrates too close to its host star to be inside the Roche limit could be disrupted by Roche lobe overflow. Such a disruption event would leave behind a dense rocky core of the hot Jupiter if the giant was formed by core accretion. Similar occurrence rates for USPs and hot Jupiters with orbital periods < 10 d found by [Sanchis-Ojeda et al. \(2014\)](#) were put forward in support of this hypothesis. However, it was quickly realised that hot Jupiters are probably not the originators of USPs. [Winn et al. \(2017\)](#) found that the metallicity distribution of the USP host stars and that of the hot Jupiter host stars are significantly different. Moreover, as pointed out by [Winn et al. \(2018\)](#), while USPs are typically found in multi-planetary systems with one or more nearby companions, hot Jupiters hardly have any nearby planets at least within 2–3 orbital periods of the hot Jupiter. Both of these points suggest that hot Jupiters and USPs exist in different kinds of planetary systems, and one cannot be the progenitor of the other.

[Raymond et al. \(2008\)](#) hypothesised that if there is enough mass in the protoplanetary disk, it is possible to form hot terrestrial planets locally *in situ*. Since the amount of total material in the disk increases with the radial distance, and if it could already form one close-in terrestrial planet, it could form more rocky planets further away in the system. Simulations by [Raymond et al. \(2008\)](#) showed that the inner USP around FGK host stars would be dry (i.e., water-poor) in composition because the delivery of water from beyond the snowline¹ becomes unlikely as the line would be far from the planet. On the other hand, USP with an M-dwarf host could be water-rich because the proximity of the snowline to the planet ensures water delivery to the planet. [Raymond et al. \(2008\)](#) suggested both of these characteristics of a) system architecture of multiple rocky planets and b) water-rich USPs as diagnostics to know whether the USPs in question formed *in situ*. While some of the USPs, e.g., CoRoT-7 b, seem to form *in situ* (see, e.g. [Léger et al., 2011](#)), many others, especially those around M-dwarfs, are unlikely to form this way. One of the main concerns against this model was whether stars, especially lower mass

¹The location in the protoplanetary disk beyond which enough decrement in the temperature causes water to condense.

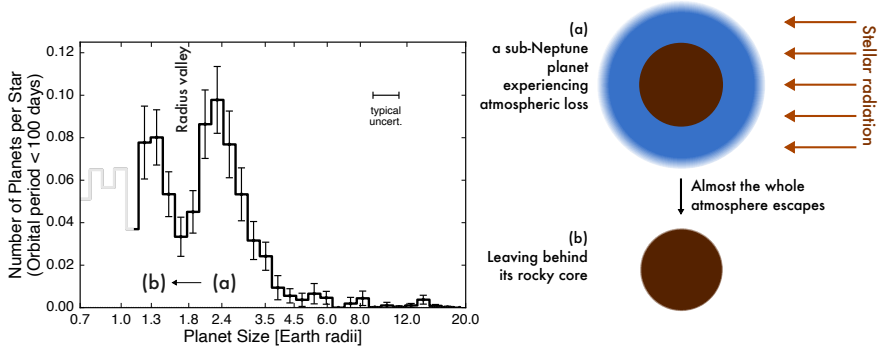


Figure 5.3: The left panel shows the distribution of the number of planets with planetary radii $< 20R_{\oplus}$, illustrating the radius valley. The plot is taken from [Fulton et al. \(2017\)](#). The right panel depicts the formation of USPs from the photo-evaporation of low-mass giants.

stars, could have sufficiently dense and massive protoplanetary disks to form rocky planets *in situ*.

Other pathways to form USPs include formation in outer parts of the disk followed by various types of migration (see [Raymond et al., 2008](#); [Winn et al., 2018](#)). The end system configuration from such a scenario is usually a multi-planet system in mean-motion resonance (MMR, i.e., the period ratios of two nearby planets are integers). However, this MMR is not always satisfied for USPs, making this formation channel unlikely.

The most widely accepted view of the formation of USPs is by atmospheric escape, also known as photo-evaporation, of low-mass gas giants. Upon observing the hot Jupiter HD 209458 b in transit at Lyman- α wavelength, [Vidal-Madjar et al. \(2003\)](#) discovered that neutral hydrogen was escaping from the atmosphere of the planet. One of the primary processes causing the escape was thought to be hydrodynamic escape (see, e.g., [Lammer et al., 2003](#); [Owen, 2019](#)). The basic idea behind hydrodynamic escape is that when XUV (X-ray and extreme UV) flux from the star heats the upper atmosphere of the planet and increases its temperature to thousands of Kelvins, it will become unstable and expand hydrodynamically. The velocity of the material could become larger than the escape velocity, causing the material to extend beyond the Roche lobe. This process, also known as atmospheric blow-off or photo-evaporation, is theoretically similar to the Parker instability and could result in losing the bulk of the atmosphere from the planet (see [Owen, 2019](#)). Although other thermal (e.g., Jeans escape) and non-thermal (e.g., stellar wind scavenging, sputtering, etc.) processes exist, they are not as efficient as hydrodynamic escape,

as a bulk of the atmosphere could escape in the latter case. While hot Jupiters are found to be stable against atmospheric loss (although it was initially suggested that they could not remain stable, see [Lammer et al., 2003](#)), smaller gas giants, e.g., hot mini-Neptunes could lose their entire atmosphere via hydrodynamic escape leaving behind the rocky core ([Raymond et al., 2008](#); [Owen & Jackson, 2012](#); [Owen & Wu, 2013](#); [Lopez & Fortney, 2013](#); [Owen, 2019](#)). It was further predicted that if mini-Neptunes could indeed photo-evaporate their whole atmosphere, exposing their rocky core as terrestrial planets, there should be an overall lack of intermediate mass planets with a radius around $2 R_{\oplus}$ known as the evaporation valley in period-radius space ([Owen & Wu, 2013](#); [Lopez & Fortney, 2013](#)). The prediction was later confirmed by observations of *Kepler* planets (see Fig. 5.3, [Fulton et al., 2017](#)). A low-mass gas giant planet ($\lesssim 25 M_{\oplus}$), with $2-3 R_{\oplus}$ radius, would undergo photo-evaporation and eventually lose its whole atmosphere to become a rocky planet (see Fig. 5.3). The statistical confirmation of this hypothesis by *Kepler* helped cement this view of the formation of USPs.

5.2 Surface and atmosphere of hot rocky planets

The atmosphere on a hot rocky planet is usually coupled with its interior and is dependent on the temperature, ultimately, on the stellar insolation at the planet. In Sect. 5.2.1, we qualitatively describe various global processes on a hot rocky planet, depicted in Fig. 5.4, that shape its atmosphere. We then move on to describe atmospheres on USPs and their observations in Sects. 5.2.2 and 5.2.3. We then briefly touch upon the evolutionary history and escape of secondary atmospheres in Sect. 5.2.4.

5.2.1 Global processes shaping the surface and atmosphere

The dayside temperature on USPs is expected to reach higher than ~ 2000 K, which is enough to melt its surface and host a lava ocean (e.g., [Léger et al., 2011](#)), which is also known as a magma ocean or a magma pool. We note that some of the cooler USPs, e.g. those around cool stars, may have solid surface ([Kreidberg et al., 2019](#)). Various theoretical models suggest that while the magma ocean would mostly cover the whole dayside, it would probably not be too deep, with depth of around 500–2000 km (see Fig. 5.4; [Kite et al., 2016](#); [Meier et al., 2023](#)). The surface on the nightside is not expected to be completely molten (however, it can remain partially molten, see [Meier et al., 2023](#)). However, a recent study by [Herath et al. \(2024\)](#) showed that the magma ocean can extend up to the nightside if the heat transport to the nightside is efficient, which could be possible because of the viscosity of the magma. Moreover, the

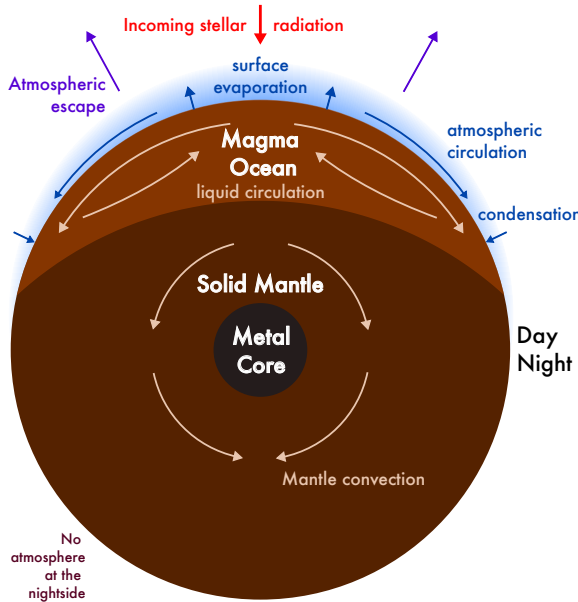


Figure 5.4: Schematic diagram of global atmospheric and interior processes happening on a typical hot rocky planet. The figure, which is a remake of a similar figure from Kite et al. (2016), showcases a magma pool with liquid circulation, a thin rock vapour atmosphere which could condense back to the surface away from the substellar point or escape from the atmosphere. The figure is not drawn to scale.

tidal heating can provide an additional source of heating that can sustain a magma ocean on the nightside. The compositional and temperature gradient inside the magma ocean drives the liquid circulation in the ocean, which is referred to as magma pool overturning (Kite et al., 2016). The same gradients may also start mantle convection, which enables the transport of materials throughout the interiors (Meier et al., 2023).

By studying various lava surfaces in laboratory, Essack et al. (2020) found that most of them are dark and produce low geometric albedos ($\lesssim 0.1$). However, in some cases, lava oceans may have evolved (see below) and their surface may contain Ca/Al oxides, which can produce higher geometric albedos. In any case, it is possible to infer the surface composition from occultation measurements as each composition could produce different occultation depths (or albedo, in other words), especially in the IR. Kreidberg et al. (2019) has used occultation depth measurement of a USP LHS-3844 b at $4.5 \mu\text{m}$ with *Spitzer* and showed that the emission from the planet is consistent with the basaltic surface formed from volcanic eruptions. More observations of the planet are planned with JWST to conclusively determine the surface composition of the planet (Zieba et al., 2023).

Although the USPs are, in general, thought to be devoid of any primordial atmosphere made up of H/He because of their fast escape (Owen & Jackson, 2012; Owen & Wu, 2013; Lopez & Fortney, 2013; Charnoz et al., 2023), they can form and possibly sustain a secondary atmosphere (Charnoz et al., 2023). The lava surface on the planet would be hot enough to make a thin silicate at-

mosphere from evaporation of the surface (atmospheric properties are more described below). The temperature on the dayside decreases azimuthally from the substellar point to the day-night terminator, which would prompt a decrement in atmospheric pressure, as the atmosphere is made from the surface evaporation (Castan & Menou, 2011). The drop in temperature and pressure could be rapid and drastic as we approach the day-night terminator — up to 2500 K and 10^4 bar decrease in temperature and pressure, respectively (though the exact numbers depend strongly on the used model and the planet itself; Castan & Menou, 2011). This strong azimuthal temperature and pressure gradient on the dayside generates strong winds, with speeds up to 1-2 km/s, away from the substellar point, enabling atmospheric transport (see Fig. 5.4; Castan & Menou, 2011; Kite et al., 2016). Since the temperature is decreasing rapidly towards the day-night terminator, the atmospheric wind flow would start condensing after some point, and the material would dissolve in the magma pool. Eventually, the whole atmosphere would condense to the surface. This means that the atmosphere on the USPs is confined to the dayside of the planet only (see Fig. 5.4). Some of the atmospheric material may escape permanently into space as well.

Essentially, there are two processes regulating the global atmosphere and surface of the planet: i) surface evaporation and atmospheric flow and ii) magma pool overturning. Kite et al. (2016) found that the former process dominates the latter on planets with substellar temperature $\gtrsim 2400$ K, resulting in a compositionally distinct surface than the rest of the ocean. This happens because the increasing temperature accelerates the evaporation, making it more efficient than the slower magma currents. As more volatile elements such as Na and K evaporate from the surface because of this, the slower liquid circulation in the pool cannot replenish the surface, leading to an ‘evolved’ surface. A higher evaporation rate could even make the surface variegated in composition over the dayside. On top of this, if the planet’s bulk composition is FeO-rich, the evaporation of volatiles and dense Fe would advocate the stratification of the pool, which can create a refractory lag made of Ca and Al oxides on the surface. The magma pool stratification further slows down the pool overturning and eventually the exchange with the atmosphere. Detection of Ca/Al oxides, which is easy since they have a high geometric albedo (Essack et al., 2020), on a planetary surface would be crucial in constraining planetary composition (e.g., FeO-rich), which, in turn, sheds light on the planet’s formation and evolution.

On the other hand, for planets with a substellar temperature lower than about 2400 K, the magma pool overturning dominates the surface evaporation — an efficient overturning would make the magma ocean compositionally uniform. This may reduce the possibility of forming Ca/Al oxide refractory

lag on the surface, even if the planet's bulk composition is FeO-rich, because efficient overturning prevents stratification.

5.2.2 Rock vapour atmospheres

Since a secondary atmosphere on hot rocky planets is created by evaporation of the surface, their study would not only give information about the atmospheric structure but also about the interior composition. The interior composition is, in turn, strongly linked with the formation and evolution history of the planet (e.g., [Raymond et al., 2008](#)). Moreover, the detection of the secondary atmosphere over a magma ocean would help us understand the formation and evolution of secondary atmospheres on the rocky planets of our own Solar System, some of which, e.g., Earth, were thought to have a magma ocean at some point in their evolutionary history. Finally, observations of an atmosphere on extreme planets can tell us how atmospheres behave in extreme conditions found on USPs.

Many works have tried to model the vapourised atmospheres on lava planets (e.g., [Schaefer & Fegley, 2009](#); [Miguel et al., 2011](#); [Ito et al., 2015](#); [Zilinskas et al., 2022](#)). The chemical inventory of the evaporated atmosphere is computed by assuming magma-vapour chemical equilibrium and contains various oxides of Al, Ca, Fe, K, Mg, Na, Si and Ti ([Schaefer & Fegley, 2009](#); [Zilinskas et al., 2022](#)). Abundances of these oxides are computed using vapour-vapour chemical equilibrium for a given temperature at various pressure levels in the atmosphere. Since the temperature-pressure (TP) profile – temperature at various pressure levels in the atmosphere – itself depends on the atmospheric chemistry, we need to solve both problems of chemical structure and thermal structure simultaneously. In practice, both computations, alongside solving the radiative transfer equation, are run simultaneously and iteratively until convergence is achieved. We describe the results of these modelling here, though the details of exact modelling could be found elsewhere (e.g., [Zilinskas et al., 2022](#), and references therein). Once the TP profile and atmospheric chemistry are found, synthetic emission spectra, in the form of occultation depth as a function of wavelength, are computed. Some examples of model emission spectra and TP profiles are shown in Fig. 5.5.

Several works independently show that the main constituents of the rock vapour atmospheres are Na, SiO, SiO₂, K, MgO with Na and SiO being the most abundant species ([Schaefer & Fegley, 2009](#); [Miguel et al., 2011](#); [Ito et al., 2015](#); [Zilinskas et al., 2022](#); [Charnoz et al., 2023](#); [Falco et al., 2024](#)). Many ionic species like Na⁺, Ca⁺, Si⁺, etc. are also present in the atmosphere, however, they do not contribute significantly to the opacity.

The presence of Na and SiO, which are strong sources of short-wave opac-

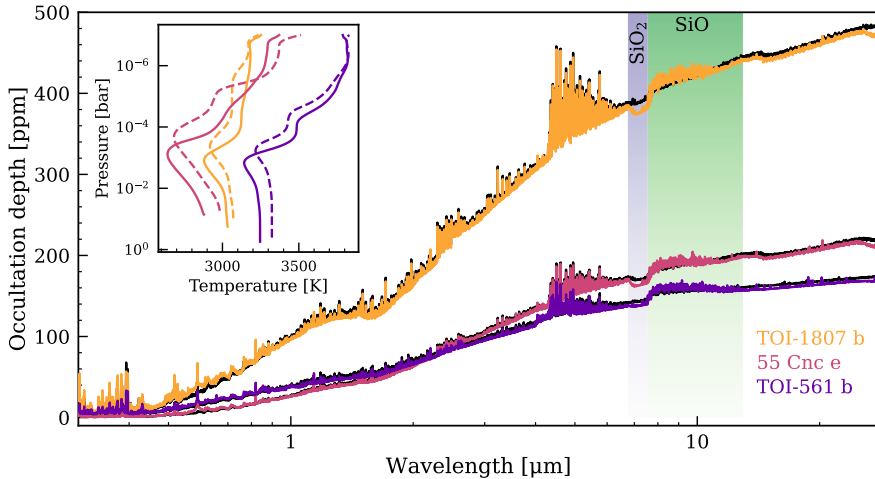


Figure 5.5: Emission spectra, i.e., occultation depths as a function of wavelength, of rock vapour atmospheres for three USPs taken from Zilinskas et al. (2022). The coloured and black spectra show the spectra for the non-evolved and evolved surface conditions, respectively. We also mark the location of significant opacity sources. The inset box shows the corresponding TP profiles; the dashed profile represents the evolved surface.

ity, creates the thermal inversion, i.e., temperature increases with height or decreasing pressure (see Fig. 5.5). The process of thermal inversion is similar to what is seen in the stratosphere of the Earth because of ozone, and happens because the short-wave opacity becomes larger than the IR opacity. This causes short-wave radiation to be absorbed in the upper atmosphere, which heats the surroundings. The TP profile governs whether the spectral feature would appear as emission or absorption in the spectrum: if the given species radiates from the zone where the temperature is increasing with the pressure, the corresponding feature would appear as an emission feature, while it would appear as an absorption feature in the opposite case (see also Fig. 2.7).

The emission spectra for some planets are shown in Fig. 5.5, which are taken from the models presented by Zilinskas et al. (2022). SiO being one of the most abundant species, its features are prominent in the spectra, visible as emission features at around 9 μm and 4.5 μm. Another notable feature is of SiO₂ near 7 μm. Although Na is another common species in the atmosphere, it is also the most volatile species prone to atmospheric loss. Therefore, it may not always be visible in the spectra, but when it does, it will show a strong emission line at 0.6 μm (Falco et al., 2024). Zilinskas et al. (2022) also modelled the emission spectra for the case when the atmosphere is outgassed from

the evolved surface (see Sect. 5.2.1). The corresponding spectra are shown in black in Fig. 5.5. Almost all spectral features are diminished because of the loss of material to space, which was powered by high surface evaporation (see Sect. 5.2.1).

Observations with the *James Webb* Space Telescope (JWST) would help identify some of these features. For example, one of the instruments on board JWST, the Mid-InfraRed Instrument (MIRI), can observe in wavelength ranges from 5–28 μm , covering SiO and SiO₂ features (see Fig. 5.5). Detection of both features together means that the surface is likely not evolved, which, in turn, indicates that the lava ocean is well-mixed and that probably the bulk composition of the planet is FeO-poor. Researchers have tried to observe silicate atmospheres in some of the USPs, for instance, Hu et al. (2024) searched for silicate features in mid-IR observations of 55 Cnc e with MIRI/JWST. However, they concluded that the atmosphere lacks silicate species.

5.2.3 Volatile-rich atmospheres

The hot rocky planets are thought to be lacking volatile elements such as H and C because of high atmospheric escape. However, there are certain situations in which the USP atmospheres could contain volatiles. For example, younger planets that have not yet lost all of their atmospheres should have a significant volatile fraction. Additionally, the planet can outgas volatiles into the atmosphere from its interior if it accreted a significant portion of volatiles during its formation process.

Charnoz et al. (2023); Falco et al. (2024) have studied the effect of H in the atmosphere of hot rocky planets and on the observed emission spectra. Hydrogen in the atmosphere will immediately start reacting with oxygen to make water. Loss of oxygen will, in turn, promote the production of SiO. When there is excess hydrogen, it will directly start reacting with Si to make species like SiH₃, SiH₄ etc. Other species that are present in the atmosphere are Na, K, Fe, MgO, or even hydrocarbons if the equilibrium temperature is low enough (see, e.g., Zilinskas et al., 2023). The addition of H to the atmosphere would reduce the strength of thermal inversion except for very high equilibrium temperatures when a high amount of SiO re-introduces thermal inversion. The spectral features in the spectra could appear as emission or absorption features depending on the temperature profile. The emission spectra of H-rich atmospheres for planets with three equilibrium temperatures are shown in the left panel of Fig. 5.6. The spectra are shown for two hydrogen partial pressures. The main spectral features seen are of SiO and H₂O with some other weak features from Na, K and Fe. We note here that the features can appear either as absorption or emission, depending on the equilibrium temperature.

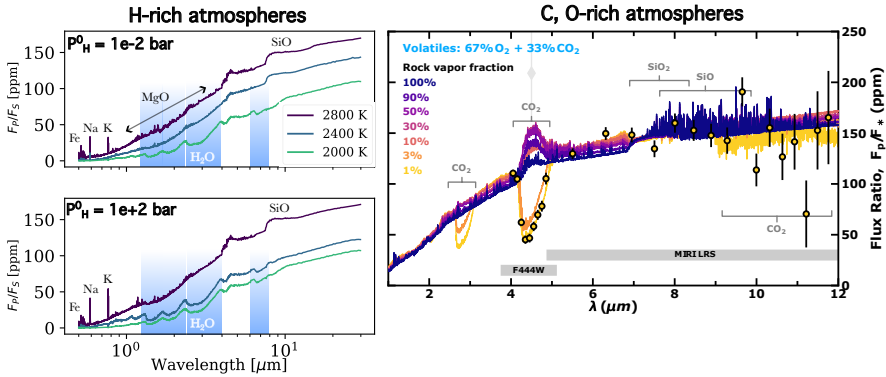


Figure 5.6: Emission spectra of volatile-rich atmospheres. (Left) Spectra of H-rich atmospheres for two different H partial pressures, 10^{-2} and 10^2 bars, taken from Falco et al. (2024). Each case shows spectra for planets with three equilibrium temperatures. (Right) Spectra for C, O-rich atmosphere (with 67% O₂ and 33% CO₂; taken from, Piette et al., 2023) with different fractions of rock vapour indicated by colours. Both panels mark the spectral locations of several important species.

If the planet's interior is C-rich, it could outgas C-rich species in the atmosphere. Indeed, Piette et al. (2023) showed that this will increase abundance of CO₂ in the atmosphere (see also, Zilinskas et al., 2023). The CO₂ feature is prominent in the spectrum, as shown in the right panel of Fig. 5.6, at $4.5 \mu\text{m}$ either in absorption or in emission. The latter point depends on the amount of rock vapour (SiO). A large fraction of SiO would again cause temperature inversion, resulting in CO₂ emission features. Decreasing the amount of rock vapour would create CO₂ feature in absorption. Recently, Hu et al. (2024) found a hint of CO/CO₂ atmosphere on the USP 55 Cnc e by observing an absorption feature in the occultation depth spectra obtained with Near Infrared Camera (NIRCam) on JWST. *Spitzer* observations of the dayside of a hot rocky planet, TOI-431 b, detected a very small occultation depth, which means that the absence of an atmosphere on the planet is unlikely (see also Sect. 2.2, Monaghan et al., 2025). Monaghan et al. (2025) further suggested a presence of an outgassed atmosphere from the magma ocean underneath.

5.2.4 Escape and evolution of secondary atmospheres

One of the main processes for forming a USP is thought to be the photo-evaporation of a low-mass gas giant. Kite & Barnett (2020) showed that hydrogen could drag heavy species while the primordial atmosphere was being lost through photo-evaporation. This could make the planet atmosphere-less unless the

atmosphere is revived by, e.g., volcanic outgassing. They further argue that the secondary atmosphere may be stable against escape only if the XUV environment is not harsh (see [Kite & Barnett, 2020](#), for details). This finding may have important implications for the search for the atmosphere on planets orbiting around M-dwarfs and requires scrutiny by observations.

The atmosphere is prone to escape even after formation. Although low mean molecular weight species are easier to lose to space, high mean molecular weight gases can be retained on the planet after the formation of a secondary atmosphere. Hydrodynamical escape simulations show that while almost all hydrogen would be lost on an Earth-like planet in a close-in orbit, the mass-loss rate for silicate atmosphere is not high enough to make the planet completely devoid of them ([Charnoz et al., 2023](#)). Furthermore, a continuous replenishing, e.g., in the form of volcanic outgassing, could sustain a planet's secondary atmosphere.

6

Hot Jupiters

“None of those worlds [exoplanets] will be identical to Earth. A few will be hospitable; most will appear hostile. Many will be achingly beautiful. In some worlds, there will be many suns in the daytime sky, many moons in the heavens at night, or great particle ring systems soaring from horizon to horizon.”

Carl Sagan in *Cosmos*

DESPITE the similarities of the names with the gas giant in our Solar System, hot Jupiters have very distinct physical properties. The hot Jupiters, as the name suggests, have high temperatures (on the order of 1000 K) because of intense stellar radiation caused by their proximity to the host stars. The proximity further ensures a tidally locked orbit for the planets, making them slow rotators. On the other hand, gas giants in our Solar System are cooler (~ 100 K) and fast rotators. The internal heat of the hot Jupiters can be neglected compared to the intense stellar radiation experienced by these planets, which means that the stellar radiation solely governs the atmospheric structure of the planet. This is not the case for our local gas giants that are both heated from above and within. Additionally, the hot Jupiters are subjected to the tidal force because of their close-in orbits. All of these together change the atmospheric make-up of hot Jupiters, diverging from that of Jupiter. We first discuss the formation mechanisms of hot Jupiters (Sect. 6.1) in this chap-

ter. Afterwards, we investigate the atmosphere of hot Jupiters from chemical (Sect. 6.2), thermal, and dynamical (Sect. 6.3) points of view.

6.1 Formation mechanisms

Planets are formed from protoplanetary disks (also known as the circumstellar disk), which are gas and dust disks found around young stars. There are two ways to form a gas giant from a protoplanetary disk: either by disk instability (Boss, 1997) or by core accretion (Pollack et al., 1996). In the former process, the gaseous disk becomes gravitationally unstable and starts forming gas clumps that later grow bigger to form gas giants. On the other hand, the solid rocky-icy core forms first in the core accretion scenario, which then forms a gas giant by accreting gases on top of the core. The mass of this core is about $10 M_{\oplus}$ to start the gas accretion efficiently (Pollack et al., 1996). The hot Jupiters must have formed via either of these methods. The question then arises about where the hot Jupiters have formed in the protoplanetary disk.

The hot Jupiters could have formed *in situ* at the location where we find them today, close to their host stars. However, it is challenging to form a giant planet by disk instability or core accretion close to the star. The fast rotation of the gas and temperature-induced pressure in the protoplanetary disk would support the disk against gravitational collapse (e.g., Rafikov, 2005). Core accretion can, in principle, form giant planets *in situ*, given that a solid core is formed. However, the formation of a solid core near the star is difficult in the first place. There may not be enough solid mass in the inner parts of a typical circumstellar disk to form $\sim 10 M_{\oplus}$ solid core. Pebble accretion, that is, the accretion of millimetre-to-centimetre-sized pebbles by the solid cores, could deliver enough material to the inner disk to quickly form a solid core. However, the pebble accretion may stop before the solid core can grow big enough (e.g., Dawson & Johnson, 2018; Johansen & Lambrechts, 2017, for a review).

While the *in situ* formation of hot Jupiters is challenging, they can easily form *ex-situ*, far from the star. There is enough solid and ice material further out in the disk, e.g., beyond the snow lines of prominent molecules such as water and CO_2 , where a solid core of mass of about $10 M_{\oplus}$ could form comfortably. The solid core can accrete the available gases to form a gas giant. Similarly, the disk rotation and temperature are appropriate for forming a gas giant planet via disk instability far from the star, e.g., beyond a few tens of AU. The newly formed gas giants can finally migrate to the close-in orbits through some processes. For instance, the gas giant can interact with the still-present gaseous disk and exchange angular momentum to migrate inward. Similarly, after the disappearance of the disk, the planet can interact with other planets in the system. These interactions can excite the eccentricity of the orbit, which

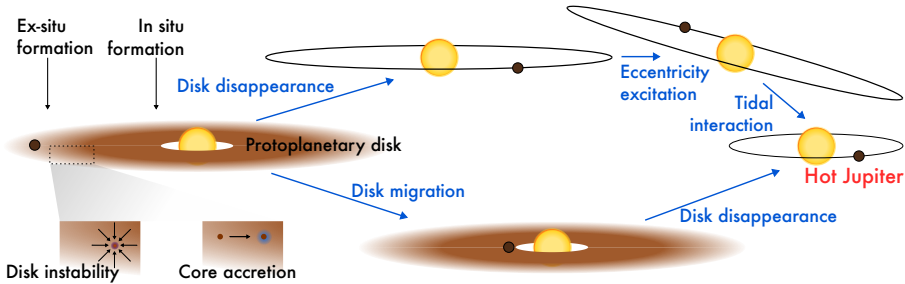


Figure 6.1: The figure depicts various formation mechanisms for a hot Jupiter, which is a modified version of a similar figure from [Dawson & Johnson \(2018\)](#).

is followed by inward migration because of the planet's tidal interaction with the star (e.g., see [Fortney et al., 2021](#); [Dawson & Johnson, 2018](#)). Fig. 6.1 summarises various formation channels of a hot Jupiter.

The formation mechanism and location leave their impact on the planet, especially on the planet's chemical abundances. As mentioned previously, planets form from the protoplanetary disk — the disk has a temperature gradient along the radial distance from the star. As the temperature drops radially, various elements start to condense gradually according to their condensation temperature. The location in the disk where a given element condenses is called the snowline for that element: the element is expected to be in the gaseous and solid phases inside and outside of its snowline, respectively. Some of the most abundant elements besides hydrogen (H), carbon (C) and oxygen (O), are present in several molecular forms such as water (H_2O), carbon dioxide (CO_2) or carbon monoxide (CO) in the protoplanetary disk (e.g., [Öberg et al., 2023](#)). All of these molecules have different condensation temperatures. The radial temperature gradient, together with different condensation temperatures, will create a radial abundance gradient. If a gas giant is formed by accreting gas (e.g., core accretion mechanism), the planetary atmospheric chemical abundance (e.g., abundance of C, H, O) would depend on the location where the planet accretes the gas. Therefore, we can estimate the planet formation location by measuring the elemental chemical abundances. In practice, we typically measure the abundance ratios, e.g., carbon-to-oxygen abundance ratio (C/O), often by comparing them to the corresponding abundance ratios of the planet host star.

[Öberg et al. \(2011\)](#) showed that the planetary atmospheric C/O ratio should be equal to the stellar C/O ratio for the planets which formed inside H_2O , CO_2 , and CO snowlines since these molecules are in gas-phase, and, thus, well mixed. On the other hand, if the planet is polluted by icy grains of H_2O , CO_2 , and CO after gas accretion, e.g., beyond the snowlines of predominant

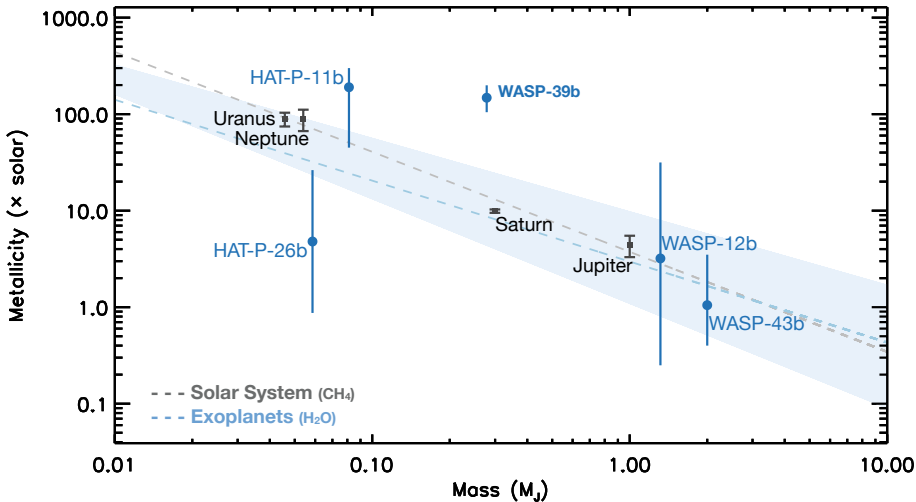


Figure 6.2: The trend of atmospheric metallicity with their mass (in Jupiter mass, M_J), taken from Wakeford et al. (2018). The Solar System planets and exoplanets are shown in black and blue, respectively. The metallicities are computed using CH_4 and H_2O abundances, respectively, for the Solar System planets and exoplanets. The best-fitted trends are shown with dashed lines. The shaded blue region shows the 68% confidence interval of the best-fitted trend for exoplanets.

molecules, it would result in stellar or sub-stellar C/O and superstellar C/H. This is because ices add a lot of oxygen and carbon into the planetary envelope. Superstellar C/O and C/H ratios are a consequence of gas accretion near CO_2 or CO snowline, where carbon mainly remains in the gas phase while oxygen-rich species (H_2O , CO_2) freeze out. Accretion of carbon-rich grains can also increase the carbon abundance, which can increase C/O and C/H ratios. However, the C/H ratio will become substellar if this additional accretion of carbon-rich grains does not happen. On the contrary, the C/O and C/H ratios will remain equal to the stellar value regardless of the formation location, if the planet was formed via disk instability, since the material would be well-mixed. In conclusion, it is possible to estimate the planet formation mechanism and location by measuring abundance ratios (Öberg et al., 2011).

With the advent of the *James Webb* Space Telescope (JWST), it is now possible to directly constrain carbon abundance in planetary atmospheres. This can be done because the wavelength coverage of JWST includes spectral features of several carbon-bearing species. Indeed, the C/H and C/O ratios (also called carbon metallicity) have been estimated for several gas giants using JWST observations (e.g., Feinstein et al., 2023; Xue et al., 2024; Fu et al., 2024; Meech et al., 2025; Ahrer et al., 2025; Wiser et al., 2025, to name a few). The metallicity is found to follow a linear trend with planetary mass (Fig. 6.2) — more

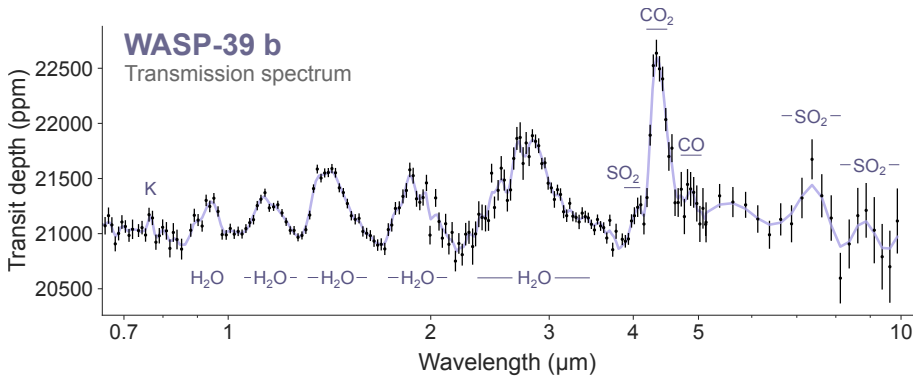


Figure 6.3: Pan-chromatic transmission spectrum (black data points) of WASP-39 b observed with multiple JWST instruments (taken from [Espinoza & Perrin, 2025](#), and references therein). We overplot a Gaussian filter of the data (in purple) to show the spectral features clearly.

massive planets are metal-poor compared to low mass gaseous planets (e.g., [Wakeford et al., 2018](#); [Welbanks et al., 2019](#); [Sun et al., 2024](#)). This happens because bigger planets have a massive core, which can accrete a large amount of H/He envelope, overall decreasing the metallicity. The mass-metallicity relation is hypothesised to be a natural outcome of the core accretion mechanism to form gas giants (e.g., [Fortney et al., 2013](#); [Thorngren et al., 2016](#)). The mass-metallicity correlation for exoplanets nicely follows the trend observed in the Solar system (Fig. 6.2).

6.2 Atmospheric chemistry

The atmospheric chemistry of hot Jupiters is characterised by strong stellar irradiation and a tidally locked orbit. Several chemical species, including Na, K, H₂O, CO, CO₂, CH₄, and NH₃, are expected to be present in hot Jupiters' atmosphere depending upon temperature, pressure and chemical abundances (e.g., [Lodders & Fegley, 2002](#); [Madhusudhan, 2012](#); [Moses et al., 2013](#)). Transmission (Sect. 2.1.2) and emission (Sect. 2.2.1) spectroscopy of transiting hot Jupiters were proved to be very successful in detecting these species. The Wide Field Camera 3 (WFC3) on board the *Hubble* Space Telescope (HST) was instrumental in detecting H₂O in the atmospheres of many planets: it turns out that H₂O is the most common molecule detected in exoplanetary atmospheres (e.g., [Kreidberg et al., 2014, 2015](#); [Wakeford et al., 2018](#); [Feinstein et al., 2023](#)). The carbon-bearing molecules can now be detected with JWST (e.g., [JWST Transiting Exoplanet Community Early Release Science Team et al., 2023](#)). Fig. 6.3 shows a pan-chromatic transmission spectrum, from about 0.5 μm to 10 μm,

of WASP-39 b observed with JWST as a part of the Early Release Science (ERS) program, which shows clear spectral features of not only H₂O, but also CO₂, CO, and SO₂ (Carter et al., 2024; Powell et al., 2024).

6.2.1 Ultra-hot Jupiters

Recent theoretical modelling and observational efforts have shown that hot Jupiters with different temperatures have diverse physical properties (e.g., Arcangeli et al., 2018; Parmentier et al., 2018; Mansfield et al., 2021). A whole new class of gas giants, called ultra-hot Jupiters, has emerged that has extreme dayside temperatures ($> 2000\text{--}2500$ K). A statistical analysis of the emission spectra between 1.1 and 1.7 μm of 19 hot Jupiters shows that the spectral shape of the 1.4 μm water feature changes with the temperature (Mansfield et al., 2021): while the water spectral feature appears in absorption for cooler hot Jupiters (with temperature $\lesssim 2000$ K), it is detected in emission for the ultra-hot Jupiters. This suggests that the temperature-pressure profile, which is non-inverted (i.e., temperature decreases with altitude) for cooler planets, becomes inverted (i.e., temperature increases with altitude) for hotter planets (see Sect. 2.2.1 for the connection between the shape of the spectral feature and temperature profile). When the atmosphere's optical opacity exceeds the infrared opacity, the incoming short-wave radiation gets absorbed in the upper atmosphere and heats it, increasing the temperature with altitude. Furthermore, the opacity of some of the optical absorbers, e.g., TiO, reduces the cooling of the upper atmosphere, and, thus, enhances the temperature inversion (e.g., Parmentier et al., 2015). The extreme temperatures of ultra-hot Jupiters make it easy to sustain short-wave absorbers, such as TiO and VO, in the gas phase, which results in an inverted temperature profile (e.g., Arcangeli et al., 2018; Parmentier et al., 2018). Detection of TiO in the atmosphere of an ultra-hot Jupiter, WASP-189 b, supports this hypothesis (Prineth et al., 2022, 2023). The higher dayside temperatures of ultra-hot Jupiters mean that many of the chemical species will be thermally dissociated and, thus, will exist in atomic form on the dayside (Hoeijmakers et al., 2019, 2020).

6.2.2 Reflective properties of close-in gas giants

The occultation depth measurement of exoplanets in the optical bandpass can estimate the planet's reflective properties by measuring the geometric albedo of the planetary dayside (Sect. 2.2). The presence of clouds in the planetary atmosphere is one of the main factors affecting the geometric albedo of the planet. Although clouds are ubiquitous in exoplanetary atmospheres, especially on the cooler morning/evening and nightside of the planet (e.g., Sing et al., 2016), the hot dayside is mostly cloudless (e.g., Parmentier et al., 2016;

Helling et al., 2023). This happens because the cloud species can only condense at temperatures low enough, found at the morning/evening limb and the nightside. The clear dayside of the planet often leads to a very small geometric albedo, as the contribution mainly comes from the Rayleigh scattering from gas particles. Indeed, the occultation observations of several hot Jupiters from *Kepler* Space Telescope revealed low geometric albedos (e.g., Heng & Demory, 2013; Esteves et al., 2015). The low estimated geometric albedo of hot Jupiters, HD 209458 b and HD 189733 b, constrained using CHEOPS, is thought to be a result of Rayleigh scattering of star light from hydrogen molecules and absorption from sodium (Brandeker et al., 2022; Krenn et al., 2023).

While many hot Jupiters show small geometric albedos, some of the cooler ones have comparatively high albedos (e.g., Demory et al., 2013). Such high geometric albedos are typically attributed to the presence of clouds in the planetary atmospheres. Parmentier et al. (2016) have shown that several species can form clouds on the dayside of the planet that can increase the geometric albedo of the planet, and explain the observations. Their theoretical models of cloud formation show that silicate and manganese sulphide clouds should dominate the planetary atmosphere. Further detailed modelling of cloud microphysics by Gao et al. (2020) suggests that clouds and hazes¹, collectively called aerosols, should be present in the atmosphere below the equilibrium temperature of about 2000 K. They found that the metal oxides and silicates are among the most common cloud species in the atmosphere. Many of the cloud species have spectral features in the near/mid infrared (e.g., Gao et al., 2021), so the near/mid infrared observations of exoplanets with JWST should be helpful in identifying cloud species in their atmospheres. Recently, silicate clouds have been detected in the atmospheres of WASP-17 b and HD 189733 b, using the transmission and emission spectroscopy in the mid-infrared with JWST (Grant et al., 2023; Inglis et al., 2024).

Optical phase curve observations of some hot Jupiters with *Kepler* have found evidence of inhomogeneous reflectivity across the dayside of the planet (e.g., Demory et al., 2013; Esteves et al., 2015). The inhomogeneous reflectance leaves its impact on the planetary phase curve, which should be possible to measure (e.g., Hu et al., 2015). A careful phase curve modelling led Demory et al. (2013); Esteves et al. (2015) to suggest that the morning side is more reflective compared to the evening side for several planets. This has been explained as wind displacing clouds from the nightside to the morning side of the planet (e.g., Esteves et al., 2015).

Phase curve observations in the optical also enable us to measure the single

¹Clouds are formed by condensation of species in the atmosphere, e.g., water clouds on Earth. On the other hand, hazes are particles produced by photochemical reactions of chemical species with stellar radiation in the upper atmosphere.

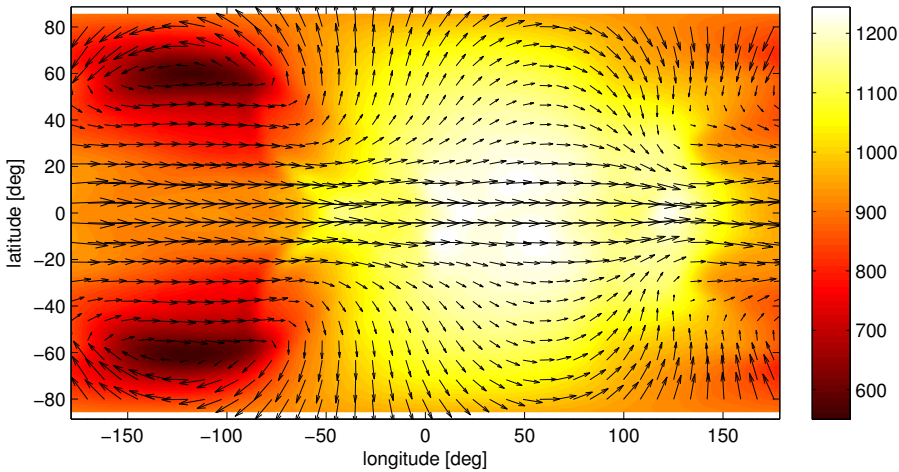


Figure 6.4: Latitude-longitude thermal and dynamical structure of a hot Jupiter as computed by a general circulation model (Showman & Polvani, 2011), taken from Heng & Showman (2015). The colours show how the temperature varies with latitude and longitude on the planet. Also shown are the magnitude and direction of winds as the length and direction of black arrows. The 0° and $\pm 180^\circ$ longitudes correspond to the local noon and midnight, respectively. Therefore, the dayside is encompassed between $[-90^\circ, 90^\circ]$.

scattering albedo (ω) and phase asymmetry factor (g) (Sect. 2.3; Heng et al., 2021). Recently, Morris et al. (2024) has used *Kepler* phase curve observations to constrain ω and g for a handful of the planets.

6.3 Atmospheric thermal and dynamical structure

Many physical properties of the hot Jupiter atmosphere are determined by planetary thermal structure, which, in turn, is closely linked with the atmospheric dynamics. For example, cloud formation and atmospheric chemistry typically rely on the underlying background temperature field. The thermal structure of the planet is needed to understand the planet's infrared phase curve. It is theoretically possible to compute a planet's thermal and dynamical structure by solving the primitive equations in conjunction with the radiative transfer (see Heng & Showman, 2015, for a review). These models are called general circulation models (GCMs); the temperature and dynamical structure computed from a GCM are shown in Fig. 6.4.

The GCM shown in Fig. 6.4, and other GCMs computed with different assumptions, show some qualitatively similar features (e.g., see Heng & Showman, 2015). First, there is a huge temperature contrast between the dayside

and the nightside (Fig. 6.4). The day-night temperature contrast can be understood by comparing the radiative (t_{rad}) and advective (t_{adv}) timescales of the atmosphere. t_{rad} is defined as the timescale over which the air gains and loses energy by absorbing starlight and radiating infrared light, respectively; on the other hand, t_{adv} is a typical time over which the air parcel advects from the day to night. $t_{\text{rad}} \ll t_{\text{adv}}$ means that the absorbed energy from the stellar radiation is quickly lost by the atmosphere before it has a chance to be transported to the nightside, resulting in a large day-night temperature contrast.

A large day-night temperature contrast generates planetary-scale Kelvin and Rossby wave that helps transport energy from day to night side (e.g., Heng & Showman, 2015). The Kelvin and Rossby waves result in a strong eastward (in the direction of the planetary rotation) jet stream, which is known as atmospheric superrotation (e.g., Showman & Guillot, 2002). The superrotation shifts the hottest point on the planet eastward of the substellar point (local noon), as is also visible in Fig. 6.4. The location of the hottest point and the day-night temperature contrast can be directly measured from the infrared phase curve observations (Sect. 2.3). Indeed, infrared phase curves of several hot Jupiters have shown a large temperature contrast and hottest location to the eastward (i.e., before occultation) of the substellar point (e.g., Knutson et al., 2007; Stevenson et al., 2014).

The infrared phase curve observations of several planets show that the day-night temperature contrast increases with the equilibrium temperature of the planet (e.g., Komacek & Showman, 2016; Komacek et al., 2017). The radiative cooling of the dayside becomes more efficient with the increasing equilibrium temperature. Furthermore, magnetic and frictional drag dampen the Kelvin and Rossby waves that help transport heat to the nightside (Komacek & Showman, 2016). Both of these increase the day-night temperature contrast. Finally, since the Kelvin and Rossby waves are damped, it would decrease the strength of superrotation (Heng & Showman, 2015).

The trend of increasing day-night contrast with the equilibrium temperature may break for ultra-hot Jupiters with an equilibrium temperature greater than about 2000 K. At these high temperatures, molecular hydrogen would dissociate to form atomic hydrogen on the dayside, while it would recombine to molecular hydrogen towards the nightside. The dissociation/recombination would increase the day-night heat transport, effectively reducing day-night temperature contrast (e.g., Bell & Cowan, 2018). The infrared and optical phase curve observations of ultra-hot Jupiters are already showing the hints of this effect (e.g., Mansfield et al., 2020; Jones et al., 2022).

Summary and outlook

“If you would be a real seeker after truth, it is necessary that at least once in your life you doubt, as far as possible, all things.”

René Descartes in *Discours de la Méthode*, 1637

THE current thesis aims to provide an introduction to the subject of investigating atmospheres of close-in transiting exoplanets. We start with a broad overview of the exoplanet science in Ch. 1. We then provide a detailed review of the transit technique in Ch. 2. We discussed how exoplanetary transits, occultations, and phase curves can be used to constrain the bulk and atmospheric properties of exoplanets. Precise photometric and spectroscopic observations with modern telescopes, such as CHEOPS, the *James Webb* Space Telescope (JWST), and the Transiting Exoplanet Survey Satellite (TESS), allow us to utilise the transit method to examine exoplanets and their atmospheres. We described in Ch. 3 how, in practice, we can use observations of transiting exoplanets to constrain the physical properties of exoplanets. Once we have estimates of mass and radius of a planet from observations, we can use the theoretical models to constrain the internal structure of the planet as outlined in Ch. 4.

Chs. 2, 3, and 4 form a toolbox of techniques an exoplanet researcher uses. These methods have been used extensively to understand the nature of many exoplanets. This thesis, in particular, deals with the characterisation of close-in rocky and gaseous planets, called ultra-short-period (USP) rocky planets

and hot Jupiters, respectively. Chs. 5 and 6 review the current research done on USPs and hot Jupiters. These chapters include topics on formation mechanisms and the atmosphere of USPs and hot Jupiters.

The current thesis includes four publications, two focusing on USPs and the other two on hot Jupiters. Sects. 7.1 and 7.2 contain a summary of scientific articles on USPs and hot Jupiters, respectively. PDF copies of all articles can be found at the end of this thesis.

7.1 Publications on USPs

7.1.1 Paper I: Photometric observations of TOI-561 b

“CHEOPS and TESS view of the ultra-short-period super-Earth TOI-561 b”
Patel, J. A., Egger, J. A., Wilson, T. G., et al., 2023, A&A, 679, A92.

This article investigates the nature of the USP planet TOI-561 b using photometric observations from CHEOPS and TESS. It was the lowest density USP discovered at the time. We measure the planetary radius with a high precision of 2 % with the help of our extensive precision observations that enabled us to model the internal structure. The models suggest that while the planet would likely not have an H/He atmosphere, other lighter materials, e.g., water, are required in addition to a pure iron core and a silicate mantle to explain observations. We further searched the data for transit depth variability caused by possible changes in the planetary envelope, but without success. Since the equilibrium temperature of the planet is about 2300 K, it can emit significantly even in the optical bandpass of CHEOPS. Motivated by this possibility, we searched for an occultation signal in the dataset. While we found tentative evidence for an occultation signal in the TESS data, we could not detect it in the CHEOPS data. Since the planet’s dayside temperature is unknown, it was not possible to uniquely constrain the geometric albedo from the occultation measurement. Comparing the occultation signal with the theoretical models of outgassed rock vapour atmospheres from the literature hinted at the possibility of a silicate atmosphere on the planet. Observations with the JWST could, in principle, find this atmosphere if it exists.

7.1.2 Paper II: Dayside emission variability of 55 Cancri e

“JWST reveals the rapid and strong day-side variability of 55 Cancri e”
Patel, J. A., Brandeker, A., Kitzmann, D., et al., 2024, A&A, 690, A159.

55 Cancri e, 55 Cnc e for short, is a $8 M_{\oplus}$, $2 R_{\oplus}$ rocky planet ($\rho = 6.7 \text{ g/cm}^3$) orbiting in a 17 hr orbit around a bright, Sun-like star. Although the planet was

observed extensively throughout the wavelength range in the past, its nature is still puzzling. Its infrared phase curve shows a significant phase offset, meaning that the hottest point on the planet is not at the substellar point, hinting towards an atmosphere on the planet (e.g., Demory et al., 2016a; Angelo & Hu, 2017; Hammond & Pierrehumbert, 2017). However, other spectroscopic observations from ground and space failed to detect any species in the atmosphere of the planet (e.g., Ehrenreich et al., 2012; Ridden-Harper et al., 2016; Esteves et al., 2017; Jindal et al., 2020; Tabernerero et al., 2020; Zhang et al., 2021; Deibert et al., 2021; Keles et al., 2022; Rasmussen et al., 2023). Furthermore, the occultation observations of the planet in the optical and infrared show the variability of the dayside emission from the planet (e.g., Demory et al., 2016b, 2023; Meier Valdés et al., 2023). Although several hypotheses have been proposed to interpret the observations, none can explain the optical-infrared variability and conundrum of the atmosphere on the planet described above.

One of the hypotheses suggested that the asynchronous rotation of 55 Cnc e can potentially explain the dayside variability of the planet (e.g., Brandeker, 2019). If the planet is in a 3:2 spin-orbit resonance (i.e., three rotation periods are equal to two orbital periods), similar to Mercury, the observer would see two different faces of the planet during consecutive occultations. Both faces would emit differently if they had distinct physical properties, which could naturally explain the observed optical and infrared emission variability of the planet. At the same time, non-synchronous rotation of the planet around its host star would shift the hottest point away from the substellar point, which could mimic the observed phase offset. We obtained time to observe five occultations of 55 Cnc e with the Near Infrared Camera (NIRCam) onboard JWST to test this hypothesis (Brandeker et al., 2021; Hu et al., 2021). If the reason for the observed dayside variability were the planet showing different faces because of the 3:2 spin-orbit resonance, the occultation depth would be strongly correlated with the epoch number. We observed simultaneous observations at $2.1\text{ }\mu\text{m}$ and at $4.5\text{ }\mu\text{m}$, with the former and latter being photometric and spectroscopic observations, respectively. We observed five occultations, of which four were observed within a week.

Our occultation observations revealed a strong variability in the dayside emission of 55 Cnc e — the band-averaged occultation depths at $4.5\text{ }\mu\text{m}$ and photometric occultation depths at $2.1\text{ }\mu\text{m}$ vary from a non-detection to a significant ~ 100 ppm depth. Unfortunately, the strong variability, since it is not correlated with epoch number, could not be a result of the planet being in a 3:2 spin-orbit resonance and thus showing different faces. Interestingly, the occultation depths at 2.1 and $4.5\text{ }\mu\text{m}$ are not correlated with each other. The emission spectra of the planet statistically favour atmospheric features in two visits, while it is consistent with a featureless spectrum in the remaining three

visits. The observed variability could be interpreted as a stochastic outgassing of the atmosphere followed by subsequent escape (Heng, 2023). Our emission spectra, which favour the presence of an atmosphere only in some of the visits, seem to support the transient atmosphere scenario. While the infrared observations can be interpreted as a result of a transient atmosphere, observations at $2.1\text{ }\mu\text{m}$ with JWST and optical occultation depths with CHEOPS are challenging to explain solely using any atmospheric effects. A grey source of opacity, for example, a circumstellar patchy dust torus generated by exovolcanism on the planet, could explain the optical-near infrared variability (Meier Valdés et al., 2023). We stress the need for multiple simultaneous observations at multi-wavelengths to resolve the nature of 55 Cnc e.

7.2 Publications on hot Jupiters

7.2.1 Paper III: Thermal and orbital structure of WASP-189 b

“TESS phase curve of ultra-hot Jupiter WASP-189 b”

Patel, J. A., Kitzmann, D., Brandeker, A., et al., submitted.

The optical CHEOPS observations of an ultra-hot Jupiter WASP-189 b previously detected an asymmetric transit caused by the misaligned planetary orbit around a gravity darkened oblate star (e.g., Sect. 2.1.1, Lendl et al., 2020; Deline et al., 2022). The CHEOPS occultation observations further detected a deep occultation. The planet was recently observed again with TESS in a slightly redder bandpass than CHEOPS. This article describes the findings of our analysis of TESS phase curves of WASP-189 b. We detected an asymmetric transit in TESS data, confirming the previous detection in the CHEOPS observations, and show that the planet is in a polar orbit around its host star. The planet’s polar orbit around an oblate star could cause the orbital precession because of the gravitational perturbations of the oblate star’s quadrupole moment (e.g., Masuda, 2015). A long temporal baseline between CHEOPS and TESS observations (TESS observed the planet roughly two years after the CHEOPS observations) allows us to check the presence of orbital precession of WASP-189 b. However, we could not detect any significant orbital precession.

We also detected a significant occultation depth in TESS lightcurves. Our atmospheric modelling suggests that the detected dayside emission in both the TESS and CHEOPS bandpass can be explained primarily by thermal emission with a negligible geometric albedo. Motivated by this, we inverted the TESS phase curve observations to find a 2D temperature map of the planet (Sect. 2.3). We re-analyse the archival CHEOPS phase curves to find a similar temperature map for the CHEOPS bandpass. Since both TESS and CHEOPS cover slightly different wavelength ranges, they probe different atmospheric

layers. Therefore, the temperature maps in both bandpasses could inform us how the temperature varies with height in the atmosphere. We found that the temperature in the CHEOPS bandpass on the planetary dayside is slightly higher than that in the TESS bandpass. This is mostly because of an inverted temperature profile, caused by the presence of TiO in the planetary atmosphere. We further used the temperature maps to constrain a small Bond albedo and a moderate heat redistribution efficiency.

7.2.2 Paper IV: Reflective properties of HD 189733 b

“The geometric albedo of the hot Jupiter HD 189733 b measured with CHEOPS”

Krenn, A. F., Lendl, M., **Patel, J. A.**, et al., 2023, A&A, 672, A24.

HD 189733 b is a warm hot Jupiter with an equilibrium temperature of about 1200 K (e.g., [Addison et al., 2019](#)). The thermal map of the planet has been constrained previously, which shows an efficient heat transport from dayside to the nightside (e.g., [Knutson et al., 2007](#)). In this article, we aim to study the reflective properties of the planet by observing its dayside emission in the optical bandpass of CHEOPS. Because of a comparatively cooler equilibrium temperature, the planetary emission in the CHEOPS bandpass is dominated by scattered light. We observed several occultations of the planet with CHEOPS to measure its occultation depth, which, later, can be used to estimate the geometric albedo of the planet. Our CHEOPS observations detected a small, but statistically significant, occultation depth of HD 189733 b. This depth is translated into a geometric albedo of 0.076 ± 0.016 . The occultation depth and geometric albedo of the planet are consistent with a cloud-free atmosphere where the scattering mainly comes from the Rayleigh scattering from hydrogen molecules and absorption from the sodium doublet. Combining this result with previous observations with the *Hubble Space Telescope* suggests a super-stellar sodium abundance on the dayside of the planet.

7.3 Frontiers in research of close-in planets

One of the main goals of the field of exoplanet science is to detect an atmosphere on rocky planets. USP planets are some of the most suitable targets for this purpose. The current observations have already started giving preliminary hints of atmospheres on USPs (e.g., [Hu et al., 2024](#)). [Patel et al. \(2023\)](#) tentatively found evidence of a silicate atmosphere on TOI-561 b. So, the first natural step is to confirm (or reject) this by obtaining precise spectra using JWST. Indeed, two JWST programs, GO 3860 ([Teske et al., 2023](#)) and GO 4818 ([Weiner Mansfield et al., 2024](#)), are precisely doing this. Their observations in

the near and mid-infrared would finally solve the puzzle of the dayside atmosphere of TOI-561 b.

Atmospheres on smaller planets like USPs are prone to atmospheric escape. Several works have pointed out that it is difficult to retain a volatile-rich atmosphere on a close-in rocky planet ([Kite & Barnett, 2020](#); [Charnoz et al., 2023](#); [Falco et al., 2024](#)). [Kite & Barnett \(2020\)](#) suggested that hot rocky planets could sustain an atmosphere only if the XUV environment is favourable. Even the secondary metal-rich atmosphere is susceptible to escape. A systematic study to search for atmospheres on multiple types of rocky planets should be useful to find which of them are likely to retain an atmosphere. Several observing programs with the JWST are designed to observe multiple rocky planets to search for atmospheres. In particular, GO 4818 aims to survey silicate vapour atmospheres in several hot rocky planets ([Weiner Mansfield et al., 2024](#)). However, their sample mainly contains planets around G and K-type stars. We can gain valuable insights into the survivability of the secondary atmosphere by including more planets around F and M-type stars. A systematic survey of atmospheres on planets with a diverse host population could test this idea empirically and have the potential to answer the question of whether USPs can retain a secondary atmosphere or not. Even if secondary atmospheres would escape eventually, it is possible that younger planets are still holding onto secondary, or primordial, volatile-rich atmospheres. Observations of younger planets could prove to be very important in not only testing this belief but also guiding our theoretical models of atmosphere and escape.

We have already detected a diverse range of chemical and aerosol species in the atmospheres of hot Jupiters. Their presence is strongly intercorrelated with the local temperature field. It is therefore important to constrain the 3D thermal structure of the planet. Additionally, such a 3D structure would be helpful in understanding the atmospheric dynamics of the planet. General Circulation Models (GCMs) of hot Jupiters have shown that the planetary flux can change significantly with latitude and longitude. The precise phase curve and occultation observations of the planet could estimate the latitude-longitude flux variations. JWST has already constrained the spatial thermal structure of several hot Jupiters (e.g., [Hammond et al., 2024](#); [Lally et al., 2025](#)). It would be curious to extend this exercise to other hot Jupiters, which is important to study the atmospheric dynamics of planets with diverse physical properties. Furthermore, with the increased sample size, we can look for statistical trends in the atmospheric properties of hot Jupiters. The European Space Agency's PLATO (PLAnetary Transits and Oscillations of stars) mission, expected to launch in late 2026, will provide high-precision observations of many hot Jupiters. It would be possible to constrain 2D latitude-longitude flux variations using this dataset. The optical bandpass of PLATO means that we

would also be sensitive to the reflective properties of planets, especially for the cooler ones. In some cases, we may even constrain the albedo distribution of the planet, which, in turn, can tell us about the cloud distribution on the planet.

Theoretical models of cloud formation have shown that hot Jupiters with different physical properties would have distinct cloud coverage (Helling et al., 2023). While cooler and hotter planets have uniform clouds and clear skies, respectively, the planets with intermediate temperatures could have inhomogeneous clouds on the morning and evening sides. Similarly, hot Jupiters are expected to have chemical and thermal inhomogeneities in their atmospheres. JWST and *Kepler* have already detected thermal and cloud inhomogeneities in the atmospheres of some hot Jupiters (Demory et al., 2013; Espinoza et al., 2024). However, ideally, we would like to have a bigger sample size to infer statistical trends and behaviour of atmospheres for a variety of planets. Archival observations with *Kepler* and new observations with PLATO would be essential in this regard. Finally, the optical observations with PLATO can constrain the reflective properties, such as single scattering albedo and scattering asymmetry factor. Morris et al. (2024) have recently used archival *Kepler* data to do this. They find that, for the planets they studied, the scattering was mainly isotropic. However, the observations of Titan in our Solar system have shown the prevalence of forward scattering (e.g., García Muñoz et al., 2017; Cooper et al., 2025). We are yet to detect non-isotropic scattering in exoplanetary atmospheres (except for a hint of back scattering in WASP-76 b; Demangeon et al., 2024). Precision observations with JWST and upcoming PLATO can potentially reveal the non-isotropic scattering in exoplanetary atmospheres. Again, a statistical sample can help us understand the trends in scattering properties of atmospheres.

Fortunately, we live in the era of telescopes that can provide precision observations. JWST and CHEOPS have already demonstrated their ability to carry out high-precision photometric and spectroscopic observations to answer the described questions. They will continue to provide high-quality science in the upcoming years. In the near future, PLATO will join their cohort to characterise exoplanetary atmospheres. Together with the current and upcoming ground-based telescopes, such as the Extremely Large Telescope (ELT), the space-based telescopes will usher us into a new era in exoplanet science.

Glossary

Aerosols Any solid particles floating in the atmosphere, typically consisting of *Clouds* and *Hazes*.

Backwards scattering Scattering process where the direction of scattered light is exactly the opposite of the direction of incident light.

Bayesian data analysis Modelling (or, fitting) observational data to recover planetary parameters that can best explain the observational data (the so-called parameter estimation). It is also possible to statistically compare competing models to determine which one best explains the data (model comparison). In the context of this thesis, the observational data typically consist of *light curves*, while the models are *transit*, *occultation*, and *phase curve* models. The procedure is often simply called data analysis.

Bond albedo (A_B) Total fraction of incident starlight scattered back into space over the whole wavelength range.

Brightness temperature Temperature of a blackbody of the same shape and at the same distance as the planet, emitting the same flux as the planet in a specific wavelength range.

CHEOPS CHaracterising ExOPlanet Satellite; a photometric satellite launched by the European Space Agency to obtain ultra-precise follow-up observations of known transiting exoplanets.

Clouds A species formed in the atmosphere by condensation.

Data analysis see, *Bayesian data analysis*.

DRP In the context of this thesis, DRP corresponds to the CHEOPS Data Reduction Pipeline, which uses simple aperture photometry to extract light curves from the observations.

Edge-on orbit Orbit whose orbital angular momentum vector points in the perpendicular direction to the line of sight.

Equilibrium temperature Temperature obtained by equating the energy absorbed and emitted by the planet, i.e., in equilibrium condition.

Exoplanets Planets orbiting stars other than our Sun.

Face-on orbit Orbit whose orbital angular momentum vector points in the parallel direction to the line of sight.

Forward scattering Scattering process where the direction of scattered and incident light is the same.

Frictional drag Any processes in the planetary atmosphere that slow down the wind motion in the atmosphere, e.g., *Magnetic drag*.

Gaussian processes Gaussian processes are a distribution over functions in the same way a Gaussian distribution is a distribution over numbers. If we randomly draw N functions from the process, they will collectively follow a multivariate Gaussian distribution. The independent variable for these functions is typically time.

Geometric albedo (A_g) Brightness of the planet compared to an illuminated isotropically scattering disk at full phase.

Gravity darkening The apparent darkening of the stellar disk from pole to equator because of the star's oblate shape.

Hazes A species formed in the atmosphere by photochemical reactions.

Heat redistribution efficiency Amount of heat transported towards the nightside from the total incident heat on the dayside of the planet.

Hot Jupiters Hot gas giants in close-in orbit around their host star.

HST *Hubble* Space Telescope; multi-purpose telescope that can obtain spectroscopic observations from ultraviolet to near infrared.

Ingress/egress Ingress (egress) is the time between when the leading and trailing edge of the planet touches the stellar disk for the first (last) time.

IR Infrared wavelengths.

Isotropic scattering It is called isotropic scattering when the light is scattered in *all* directions equally.

juliet An open-source Python package to model transit and radial velocity light curves of exoplanets using Bayesian techniques.

JWST The *James Webb* Space Telescope; multi-purpose telescope that can obtain photometric and spectroscopic observations in near and mid-infrared wavelengths beyond $\sim 1 \mu\text{m}$.

Kepler/K2 *Kepler* space telescope was a photometric telescope launched by NASA in 2008 to detect transiting exoplanets. Its observational strategy was modified after a technical issue with the satellite in 2013, which gave it a new life, and new name K2.

Lambertian disk Isotropically scattering disk.

LDCs Limb darkening coefficients; *Limb darkening* of a stellar disk is typically modelled by polynomial laws. The coefficients of the polynomial are called the limb darkening coefficients.

Light curve Stellar flux variations with time; when a light curve is observed during a transit/occultation event, it is called a transit/occultation light curve.

Limb darkening The apparent darkening of the stellar disk from the centre to the limb; happens because of the temperature gradient in the stellar atmosphere.

Magnetic drag The gas species typically ionise at high temperatures found in hot Jupiters' atmospheres. The ions react with the magnetic field, and the resulting Lorentz force resists the wind motions in the gas. This is called magnetic drag.

MCMC Markov Chain Monte Carlo; an umbrella term used for methods to draw samples from a target probability distribution.

Metallicity Abundances of elements heavier than hydrogen and helium, often quoted as an abundance relative to that of hydrogen.

MIRI Mid-InfraRed Instrument; one of the instruments onboard JWST with which we can obtain photometric and spectroscopic observations in $5\text{--}28 \mu\text{m}$.

NIRCam Near InfraRed Camera; one of the instruments onboard JWST, which can obtain photometric and spectroscopic observations between about $0.6\text{--}5.4 \mu\text{m}$.

Occultation Passage of a smaller body behind a bigger body. In the context of this thesis, occultation means a planet passing behind its host star.

Occultation depth Amount of total light from a star-planet system blocked during an occultation event.

Occultation depth spectrum Variation in occultation depths with wavelength. Since it measures the dayside emission of the planet, the spectrum is also referred to as the emission spectrum.

Occultation light curve see, *Light curve*

Orbital inclination The angle between the line of sight and the orbital angular momentum vector.

Orbital phase It gives the location of the planet in its orbit; transit and occultation locations correspond to 0 and 0.5 orbital phases.

PDCSAP Presearch Data Commissioning Simple Aperture Photometry; a data reduction pipeline developed for *Kepler*/K2 and TESS to extract photometry using SAP and remove significant systematic and stochastic trends from it.

Pebbles Small millimetre-to-centimetre-sized particles found in protoplanetary disk.

Phase curve Flux variations from the star-planet system throughout the planetary orbit where the observer sees changing planetary phases.

Phase offset The difference between the expected and observed location of the peak phase curve amplitude.

Photometry Precise flux measurements of an astronomical source in a given bandpass.

PIPE PSF Imagger Photometric Extraction; a Python package to extract photometry from raw CHEOPS data by modelling the stellar PSF.

PLATO PLAnetary Transit and Oscillation of stars; an upcoming space mission launched by the European Space Agency to study transiting exoplanets.

ppm Parts per million.

Primitive equations A set of partial differential equations governing a global atmospheric flow. These equations include the continuity equation, conservation of momentum, and the heat equation.

Protoplanetary disk Gas and dust disk found around young stars.

PSF Point Spread Function; PSF describes how the instrument spreads the light of a point source, such as a star, on the detector.

Radiative cooling Cooling of gas by emitting radiation into space.

Radiative transfer equation An equation describing how radiation, when passing through a medium, changes by absorption and emission processes.

Rayleigh scattering Scattering of light by particles much smaller than the wavelength of scattered light; the amount of scattering is proportional to the negative fourth power of the wavelength of the light.

RV Radial Velocity; typically used in the context of the velocity of the exoplanet host star measured along the line of sight.

SAP Simple Aperture Photometry; a technique where *photometry* is measured by simply summing up the total flux inside the aperture.

Scale height The typical height in the atmosphere where the air pressure decreases e-fold compared to the surface pressure.

Scalped semi-major axis Ratio of semi-major axis and the stellar radius.

Scattering asymmetry factor It defines the directional behaviour of scattering, whether it is isotropic or not.

Single scattering albedo It gives the amount of light reflected or scattered by a particle in a single scattering event.

Snowline The location in *protoplanetary disk* beyond which the decrement in temperature causes a given element to condense.

Specific intensity The amount of energy emitted by an illuminated body per frequency, or wavelength, interval, per unit time, passing through unit surface area within a unit solid angle.

Spectral extraction Process of extracting spectrum (i.e., specific intensity as a function of wavelength) from 2D spectral observations.

stark Spectral exTraction And Reduction Kit; an open-source Python package to robustly extract spectra from raw observations.

TESS The Transiting Exoplanet Survey Satellite; a survey satellite launched by NASA to detect exoplanets around bright nearby stars.

Thermal inversion Temperature typically decreases with altitude in planetary atmospheres. It is called thermal inversion, or inverted temperature profile, when the temperature increases with altitude. Since this behaviour is seen in Earth's stratosphere, the region of the planetary atmosphere with thermal inversion is also called the stratosphere.

Time-series photometry Flux variations as a function of time.

TP profile Temperature-Pressure profile; how temperature varies with pressure levels, which are proxies for height, in the atmosphere.

Transit Passage of a smaller body in front of a bigger body. This means a planet passing in front of its host star in the context of this thesis.

Transit depth Amount of starlight blocked during a transit event.

Transit depth spectra Transit depth as a function of wavelength; also called transmission spectra because the starlight transmits through the planetary atmosphere to reach the observer.

Transit light curve see, *Light curve*

TSO Time Series Observations; one of the observing modes of JWST instruments in which spectrum or photometry of a source is taken repeatedly over a certain time period, creating a time series of observations.

USP Ultra-short-period planets; rocky planets whose orbital period is less than about a day.

Volatiles A species typically found in the gaseous phase for a given temperature-pressure range.

WFC3 Wide Field Camera 3; an instrument onboard HST with which we can obtain spectroscopic observations in the near infrared.

Acknowledgements

“If I have seen further, it is by standing on the shoulders of giants.”

Sir Isaac Newton, 1675

Well, I am finally here at the end of my PhD! It has been approximately four years since I joined as a novice student new to an unknown land. Now that I am about to defend my PhD, I think I owe this to many people. It was interesting and fun four years. I would like to take this opportunity to thank these wonderful people, without whom I could not have come this far.

My first big thanks goes to my supervisor, **Alexis Brandeker** — it has been my privilege to work as your PhD student over the last four years. Thank you for always being there to help me, for answering my endless, sometimes stupid, questions, for all fun discussions, and for helping me with my postdoc applications. Thank you for giving me all kinds of opportunities, from encouraging me to write proposals or start new projects to supervising students. Thank you for taking care of me even when you were not around. Ohh, and thank you also for *Terraforming Mars*; we had many fun evenings changing the Martian weather. We are now at a point where we will put life on Venus as well! I thank **Markus Janson**, my co-supervisor, for debriefs and for allowing me to work on a project with you, which I absolutely enjoyed. It was not my area of expertise, but you were very helpful while I was learning new stuff. I also thank you as the Director of Graduate Studies – you made my life very easy on the administrative side. I thank **Anders Jerkstrand** for being supportive for the last four years and for your tips on literature review and thesis writing.

I graciously thank **Néstor Espinoza**, my master’s thesis advisor and now a kind research collaborator, for introducing me to the fantastic worlds of exo-

planets. Thank you for guiding me in my early stages as a researcher. I owe my love of statistics and data analysis to you. I also thank you for helping me with my job applications. I thank **Ludmila Carone** for all those insightful discussions about exoplanet atmospheres, which immensely helped me understand the topic better and often resulted in new projects! I am grateful to you for helping me with postdoc applications. Thank you also for inviting me and showing me around in Graz. I am thankful to **Tom Wilson** for showing me the peculiarities of CHEOPS data analysis when I was new to it, which was later useful during my first CHEOPS paper. My warm thanks to **Apurva Oza**, a fellow Gujarati-speaking exoplaneteer and a kind friend, for all those interesting meetings where we talked about many topics, including that *you-know-which planet (a pn Gujarati maa! Gujarati maa 55 kark e vishe vaato karvani to maja kaik alag j chhe, barabar ne?!)*. Thank you also for helping me with my postdoc applications. I am grateful to **Monika Lendl** for taking care of me in New Zealand and introducing me and my work to other researchers. **Vincent Bourrier** is thanked for designing the core of a project that resulted in my CHEOPS paper and for showing me how to write simply, yet, elegantly. Thank you, **Babatunde Akinsanmi**, **Aaron Bello-Arufe**, and **Vikash Singh** for making after-conference hours memorable and giving me life tips on how to survive academia. I wholeheartedly thank the whole atmosphere and data analysis working groups (**Axis 2/WG4** and **TS2**) of the **CHEOPS Science Consortium** for welcoming me to the team and giving me all those exciting opportunities to work on and develop programs. My special thanks to all of my *co-conspirators* in articles for helping me turn manuscripts into published articles.

I thank all my friends and colleagues at the Department of Astronomy at Stockholm University for a terrific time as a PhD student at the department. Thank you, **Olof Nebrin** and **Dimitri Arramy**, for not regularly coming to the office and, thus, giving us a bigger office space... hahhha just kidding, you know that I extremely enjoyed our *productive discussions* — if you know what I mean ;-) — too bad we could not produce an *Acta Prima Aprilia* paper out of it. I thank **Aaron Meissner** for making our office (and the whole corridor, actually) lively with his presence, and for sharing the love of science fiction books. Thank you guys also for the fun game nights. I am thankful to my fellow planetary group (former) PhD student **Gayathri Viswanath** for helping me get started as a new PhD in Stockholm, for a fun time in Kiruna, and for co-hosting an outreach event. Speaking of outreaches, thank you **Gloria Canocchi**, for introducing me to outreach in Stockholm by inviting me to an event and for supervising a summer school with me — I had a fun time last summer working with you on this; I think we had a blast! Thank you to former and current organisers of the Stars, Planets, and Astrobiology (SPA) group meetings, **Gayathri Viswanath**, **Gloria Canocchi**, **Mila Racca**, J... — no, no, I was

not going to thank myself (though I would like to think that I did a good job hahha) — **Jenny Frediani**, for organising interesting meetings every month (and helping me organising them for about a year and half), that too with fika. Thank you to **Simon Ringqvist** for taking us to Onsala for observations. I thank **Terese Hansen** and **Maria Cavallius** for helping me with my upcoming move to Denmark. Thank you, **Matthias Samland** and **Chinmaya Nagar**, for showing me the hidden gems of Heidelberg. **Andrii Sukhorukov** is thanked for all those hallway chats, for telling us the historical tales of the department, and for fun game nights. I thank **Tom Histon**, the *English Professor*, for inventing the corridor-skating. I appreciate the help I got from **Ryan Boukrouche** and **Mingjie Jian** regarding several research questions at different points during my PhD. **Ryan**, and **Gayathri**, thank you for your travel tips for Bergen. **Sampad Bag** is thanked for a wonderful time during the last year. I thank my teacher **Matthew Hayes** for making the Interstellar Medium (ISM) course and the problem sets interesting and stimulating. Thank you to **Daniel Mortlock** for such a fantastic Bayesian statistics course – I always loved Bayesian statistics, but your course made me appreciate Bayesian statistics even more. **Sergio Gelato** and **Bengt Larsson** are thanked for all the fine IT support that I got for the last four years. I thank the administrative team, **Adriana Todorovic**, **Maria Youngman**, **Nariman Nik Khah**, and **Sebastian Lizak**, for all the support I got over my PhD. **Nariman**, it is always a pleasure to talk to you about the books. Now that I am about to move to Copenhagen, I am going to miss you all and Stockholm, but it is not far, so I will visit (**Gloria** and **Aaron**, I am looking at you guys xD – no pressure hahhh).

I drew inspiration from several PhD theses, including those of **Alexis Branderker**, **Markus Janson**, **Néstor Espinoza**, **Gayathri Viswanath**, and **Simon Ringqvist**, while writing my own. Thank you all – your theses helped me a lot in designing my own thesis. In particular, **Alexis**, some of the formatting of the current thesis is inspired by your PhD thesis, so a part of the credit for the layout goes to you!

A special thanks goes to my best friend **Daxal Mehta** for his friendship. Thanks a lot for all the great times we had over the past years, for listening to my jibber-jabbers. I am glad that you were always there to back me. I know that I could always count on you! Thank you also for the amazing trip to Italy. My warm thanks to my close friend and travel companion **Maulik Bhatt** for all those incredible trips throughout Europe – our trips made my holidays awesome! Thank you also for sharing my love of books, art, culture, and history. I always enjoy our little thought-provoking discussions. I thank **Sahil Shah**, my friend since high school, for his friendship and for aiding me in my little *mischief*. **Kaustav Goswami** is thanked for showing me around in Munich – we still have to plan a tour of Scandinavia! I thank **Viral Parekh**, **Jwalant Naik**,

Nirmal Patel, Madhavi Gujarathi Shah, and Vinod Kataria for arranging out-reach events where I could introduce the high school students to the world of exoplanets.

Last but not least, I want to thank my family for their love and support. Thank you to my parents, **Jignasha** and **Ashok Patel**, for supporting me in my choice of a non-traditional career path as an astronomer. Thank you, **Dad**, for getting a telescope and a camera during my high school years, which fuelled my love of astronomy and astrophotography. My journey as a professional astronomer started that day when I looked at the Galilean satellites through the lens of our telescope. Thank you, **Mom**, for your never-ending love and encouragement, and for making my favourite food when I am home. My warm thanks to my sister, **Maitri Patel**, for all the love and fun we had (and still have) growing up. I would like to remember my late grandparents at this moment and thank them for the pleasant time during my childhood.

Stockholm
June 27, 2025
Ashadhi Bij, 2081

References

- Acuña, L., Deleuil, M., & Mousis, O. 2023, A&A, 677, A14
- Addison, B., Wright, D. J., Wittenmyer, R. A., et al. 2019, PASP, 131, 115003
- Ahrer, E.-M., Gandhi, S., Alderson, L., et al. 2025, MNRAS
- Al Moulla, K., Dumusque, X., Figueira, P., et al. 2023, A&A, 669, A39
- Angelo, I. & Hu, R. 2017, AJ, 154, 232
- Arcangeli, J., Désert, J.-M., Line, M. R., et al. 2018, ApJ, 855, L30
- Auvergne, M., Bodin, P., Boisnard, L., et al. 2009, A&A, 506, 411
- Bakos, G. Á., Csubry, Z., Penev, K., et al. 2013, PASP, 125, 154
- Barnes, J. W. 2009, ApJ, 705, 683
- Barros, S. C. C., Akinsanmi, B., Boué, G., et al. 2022, A&A, 657, A52
- Batalha, N. M., Borucki, W. J., Bryson, S. T., et al. 2011, ApJ, 729, 27
- Bell, T. J. & Cowan, N. B. 2018, ApJ, 857, L20
- Bell, T. J., Crouzet, N., Cubillos, P. E., et al. 2024, Nature Astronomy, 8, 879
- Benz, W., Broeg, C., Fortier, A., et al. 2021, Experimental Astronomy, 51, 109
- Boley, K. M., Panero, W. R., Unterborn, C. T., et al. 2023, ApJ, 954, 202
- Borucki, W. J., Koch, D., Basri, G., et al. 2010, Science, 327, 977
- Borucki, W. J. & Summers, A. L. 1984, Icarus, 58, 121
- Boss, A. P. 1997, Science, 276, 1836

- Bourrier, V., Deline, A., Krenn, A., et al. 2022, *A&A*, 668, A31
- Brandeker, A. 2019, in AAS/Division for Extreme Solar Systems Abstracts, Vol. 51, AAS/Division for Extreme Solar Systems Abstracts, 311.07
- Brandeker, A., Alibert, Y., Bourrier, V., et al. 2021, Is it raining lava in the evening on 55 Cancri e?, JWST Proposal. Cycle 1, ID. #2084
- Brandeker, A., Heng, K., Lendl, M., et al. 2022, *A&A*, 659, L4
- Brandeker, A., Patel, J. A., & Morris, B. M. 2024, PIPE: Extracting PSF photometry from CHEOPS data, Astrophysics Source Code Library, record ascl:2404.002
- Brogi, M., Keller, C. U., de Juan Ovelar, M., et al. 2012, *A&A*, 545, L5
- Burrows, A. S. 2014, *Proceedings of the National Academy of Science*, 111, 12601
- Butler, R. P., Marcy, G. W., Williams, E., Hauser, H., & Shirts, P. 1997, *ApJ*, 474, L115
- Carter, A. L., May, E. M., Espinoza, N., et al. 2024, *Nature Astronomy*, 8, 1008
- Castan, T. & Menou, K. 2011, *ApJ*, 743, L36
- Charbonneau, D., Brown, T. M., Latham, D. W., & Mayor, M. 2000, *ApJ*, 529, L45
- Charnoz, S., Falco, A., Tremblin, P., et al. 2023, *A&A*, 674, A224
- Cooper, C. A., Robinson, T. D., Barnes, J. W., Mayorga, L. C., & Robinthal, L. 2025, arXiv e-prints, arXiv:2507.00924
- Cowan, N. B. & Agol, E. 2008, *ApJ*, 678, L129
- Dawson, R. I. & Johnson, J. A. 2018, *ARA&A*, 56, 175
- Deibert, E. K., de Mooij, E. J. W., Jayawardhana, R., et al. 2021, *AJ*, 161, 209
- Deline, A., Hooton, M. J., Lendl, M., et al. 2022, *A&A*, 659, A74
- Demangeon, O. D. S., Cubillos, P. E., Singh, V., et al. 2024, *A&A*, 684, A27
- Demory, B.-O., de Wit, J., Lewis, N., et al. 2013, *ApJ*, 776, L25
- Demory, B.-O., Gillon, M., de Wit, J., et al. 2016a, *Nature*, 532, 207
- Demory, B.-O., Gillon, M., Madhusudhan, N., & Queloz, D. 2016b, *MNRAS*, 455, 2018
- Demory, B. O., Sulis, S., Meier Valdés, E., et al. 2023, *A&A*, 669, A64
- Dorn, C., Khan, A., Heng, K., et al. 2015, *A&A*, 577, A83
- Dorn, C., Venturini, J., Khan, A., et al. 2017, *A&A*, 597, A37
- Dyreka, A., Min, M., Decin, L., et al. 2024, *Nature*, 625, 51
- Ehrenreich, D., Bourrier, V., Bonfils, X., et al. 2012, *A&A*, 547, A18
- Ehrenreich, D., Bourrier, V., Wheatley, P. J., et al. 2015, *Nature*, 522, 459
- Espinoza, N. & Jordán, A. 2015, *MNRAS*, 450, 1879
- Espinoza, N., Kossakowski, D., & Brahm, R. 2019, *MNRAS*, 490, 2262

- Espinoza, N. & Perrin, M. D. 2025, arXiv e-prints, arXiv:2505.20520
- Espinoza, N., Steinrueck, M. E., Kirk, J., et al. 2024, *Nature*, 632, 1017
- Espinoza, N., Úbeda, L., Birkmann, S. M., et al. 2023, *PASP*, 135, 018002
- Essack, Z., Seager, S., & Pajusalu, M. 2020, *ApJ*, 898, 160
- Esteves, L. J., De Mooij, E. J. W., & Jayawardhana, R. 2015, *ApJ*, 804, 150
- Esteves, L. J., de Mooij, E. J. W., Jayawardhana, R., Watson, C., & de Kok, R. 2017, *AJ*, 153, 268
- Evans-Soma, T. M., Sing, D. K., Barstow, J. K., et al. 2025, arXiv e-prints, arXiv:2506.01771
- Falco, A., Tremblin, P., Charnoz, S., Ridgway, R. J., & Lagage, P.-O. 2024, *A&A*, 683, A194
- Feinstein, A. D., Radica, M., Welbanks, L., et al. 2023, *Nature*, 614, 670
- Foreman-Mackey, D., Hogg, D. W., Lang, D., & Goodman, J. 2013, *PASP*, 125, 306
- Fortier, A., Simon, A. E., Broeg, C., et al. 2024, *A&A*, 687, A302
- Fortney, J. J., Dawson, R. I., & Komacek, T. D. 2021, *Journal of Geophysical Research (Planets)*, 126, e06629
- Fortney, J. J., Mordasini, C., Nettelmann, N., et al. 2013, *ApJ*, 775, 80
- Fu, G., Welbanks, L., Deming, D., et al. 2024, *Nature*, 632, 752
- Fulton, B. J., Petigura, E. A., Blunt, S., & Sinukoff, E. 2018, *PASP*, 130, 044504
- Fulton, B. J., Petigura, E. A., Howard, A. W., et al. 2017, *AJ*, 154, 109
- Gao, P., Thorngren, D. P., Lee, E. K. H., et al. 2020, *Nature Astronomy*, 4, 951
- Gao, P., Wakeford, H. R., Moran, S. E., & Parmentier, V. 2021, *Journal of Geophysical Research (Planets)*, 126, e06655
- García Muñoz, A., Lavvas, P., & West, R. A. 2017, *Nature Astronomy*, 1, 0114
- Gardner, J. P., Mather, J. C., Abbott, R., et al. 2023, *PASP*, 135, 068001
- Goodman, J. & Weare, J. 2010, *Communications in Applied Mathematics and Computational Science*, 5, 65
- Grant, D., Lewis, N. K., Wakeford, H. R., et al. 2023, *ApJ*, 956, L32
- Gray, D. F. 1997, *Nature*, 385, 795
- Gregory, P. C. 2005, *Bayesian Logical Data Analysis for the Physical Sciences: A Comparative Approach with 'Mathematica' Support* (Cambridge University Press)
- Grillmair, C. J., Burrows, A., Charbonneau, D., et al. 2008, *Nature*, 456, 767
- Hammond, M., Bell, T. J., Challener, R. C., et al. 2024, *AJ*, 168, 4
- Hammond, M. & Pierrehumbert, R. T. 2017, *ApJ*, 849, 152
- Hastings, W. K. 1970, *Biometrika*, 57, 97
- Hellier, C., Anderson, D. R., Collier Cameron, A., et al. 2011, *A&A*, 535, L7
- Helling, C., Samra, D., Lewis, D., et al. 2023, *A&A*, 671, A122

- Heng, K. 2017, Exoplanetary Atmospheres: Theoretical Concepts and Foundations (Princeton University Press)
- Heng, K. 2023, *ApJ*, 956, L20
- Heng, K. & Demory, B.-O. 2013, *ApJ*, 777, 100
- Heng, K. & Kitzmann, D. 2017, *MNRAS*, 470, 2972
- Heng, K., Mendonça, J. M., & Lee, J.-M. 2014, *ApJS*, 215, 4
- Heng, K., Morris, B. M., & Kitzmann, D. 2021, *Nature Astronomy*, 5, 1001
- Heng, K. & Showman, A. P. 2015, *Annual Review of Earth and Planetary Sciences*, 43, 509
- Herath, M., Boukaré, C.-É., & Cowan, N. B. 2024, *MNRAS*, 535, 2404
- Higson, E., Handley, W., Hobson, M., & Lasenby, A. 2019, *Statistics and Computing*, 29, 891
- Hoeijmakers, H. J., Ehrenreich, D., Kitzmann, D., et al. 2019, *A&A*, 627, A165
- Hoeijmakers, H. J., Seidel, J. V., Pino, L., et al. 2020, *A&A*, 641, A123
- Hoffman, M. D. & Gelman, A. 2011, arXiv e-prints, arXiv:1111.4246
- Hon, M., Rappaport, S., Shporer, A., et al. 2025, *ApJ*, 984, L3
- Hooton, M. J., Hoyer, S., Kitzmann, D., et al. 2022, *A&A*, 658, A75
- Horne, K. 1986, *PASP*, 98, 609
- Hoyer, S., Guterman, P., Demangeon, O., et al. 2020, *A&A*, 635, A24
- Hu, R., Bello-Arufe, A., Zhang, M., et al. 2024, *Nature*, 630, 609
- Hu, R., Brandeker, A., Damiano, M., et al. 2021, Determining the Atmospheric Composition of the Super-Earth 55 Cancri e, JWST Proposal. Cycle 1, ID. #1952
- Hu, R., Demory, B.-O., Seager, S., Lewis, N., & Showman, A. P. 2015, *ApJ*, 802, 51
- Hu, R., Ehlmann, B. L., & Seager, S. 2012, *ApJ*, 752, 7
- Inglis, J., Batalha, N. E., Lewis, N. K., et al. 2024, *ApJ*, 973, L41
- Ito, Y., Ikoma, M., Kawahara, H., et al. 2015, *ApJ*, 801, 144
- Jackson, B., Stark, C. C., Adams, E. R., Chambers, J., & Deming, D. 2013, *ApJ*, 779, 165
- Jacob, W. S. 1855, *MNRAS*, 15, 228
- Jenkins, J. M., Twicken, J. D., McCauliff, S., et al. 2016, in Society of Photo-Optical Instrumentation Engineers (SPIE) Conference Series, Vol. 9913, Software and Cyberinfrastructure for Astronomy IV, ed. G. Chiozzi & J. C. Guzman, 99133E
- Jindal, A., de Mooij, E. J. W., Jayawardhana, R., et al. 2020, *AJ*, 160, 101
- Johansen, A. & Lambrechts, M. 2017, *Annual Review of Earth and Planetary Sciences*, 45, 359
- Jones, K., Morris, B. M., Demory, B. O., et al. 2022, *A&A*, 666, A118

- JWST Transiting Exoplanet Community Early Release Science Team, Ahrer, E.-M., Alderson, L., et al. 2023, *Nature*, 614, 649
- Keles, E., Mallonn, M., Kitzmann, D., et al. 2022, *MNRAS*, 513, 1544
- Kempton, E. M. R., Zhang, M., Bean, J. L., et al. 2023, *Nature*, 620, 67
- Kite, E. S. & Barnett, M. N. 2020, *Proceedings of the National Academy of Science*, 117, 18264
- Kite, E. S., Fegley, Bruce, J., Schaefer, L., & Gaidos, E. 2016, *ApJ*, 828, 80
- Knutson, H. A., Charbonneau, D., Allen, L. E., et al. 2007, *Nature*, 447, 183
- Koch, D. G., Borucki, W. J., Basri, G., et al. 2010, *ApJ*, 713, L79
- Koll, D. D. B., Malik, M., Mansfield, M., et al. 2019, *ApJ*, 886, 140
- Komacek, T. D. & Showman, A. P. 2016, *ApJ*, 821, 16
- Komacek, T. D., Showman, A. P., & Tan, X. 2017, *ApJ*, 835, 198
- Kreidberg, L. 2015, *PASP*, 127, 1161
- Kreidberg, L. 2018, in *Handbook of Exoplanets*, ed. H. J. Deeg & J. A. Belmonte (Springer International Publishing), 100
- Kreidberg, L., Bean, J. L., Désert, J.-M., et al. 2014, *ApJ*, 793, L27
- Kreidberg, L., Koll, D. D. B., Morley, C., et al. 2019, *Nature*, 573, 87
- Kreidberg, L., Line, M. R., Bean, J. L., et al. 2015, *ApJ*, 814, 66
- Krenn, A. F., Lendl, M., Patel, J. A., et al. 2023, *A&A*, 672, A24
- Lally, M., Challener, R. C., Lewis, N. K., et al. 2025, *ApJ*, 983, L13
- Lammer, H., Selsis, F., Ribas, I., et al. 2003, *ApJ*, 598, L121
- Léger, A., Grasset, O., Fegley, B., et al. 2011, *Icarus*, 213, 1
- Léger, A., Rouan, D., Schneider, J., et al. 2009, *A&A*, 506, 287
- Leleu, A., Alibert, Y., Hara, N. C., et al. 2021, *A&A*, 649, A26
- Lendl, M., Csizmadia, S., Deline, A., et al. 2020, *A&A*, 643, A94
- Lodders, K. & Fegley, B. 2002, *Icarus*, 155, 393
- Lopez, E. D. & Fortney, J. J. 2013, *ApJ*, 776, 2
- Madhusudhan, N. 2012, *ApJ*, 758, 36
- Madhusudhan, N. 2019, *ARA&A*, 57, 617
- Malik, M., Grosheintz, L., Mendonça, J. M., et al. 2017, *AJ*, 153, 56
- Mandel, K. & Agol, E. 2002, *ApJ*, 580, L171
- Mansfield, M., Bean, J. L., Stevenson, K. B., et al. 2020, *ApJ*, 888, L15
- Mansfield, M., Kite, E. S., Hu, R., et al. 2019, *ApJ*, 886, 141

- Mansfield, M., Line, M. R., Bean, J. L., et al. 2021, *Nature Astronomy*, 5, 1224
- Marsh, T. R. 1989, *PASP*, 101, 1032
- Masuda, K. 2015, *ApJ*, 805, 28
- Mayor, M. & Queloz, D. 1995, *Nature*, 378, 355
- Mazeh, T., Naef, D., Torres, G., et al. 2000, *ApJ*, 532, L55
- Meech, A., Claringbold, A. B., Ahrer, E.-M., et al. 2025, *MNRAS*, 539, 1381
- Meier, T. G., Bower, D. J., Lichtenberg, T., Hammond, M., & Tackley, P. J. 2023, *A&A*, 678, A29
- Meier Valdés, E. A., Morris, B. M., Demory, B. O., et al. 2023, *A&A*, 677, A112
- Metropolis, N., Rosenbluth, A. W., Rosenbluth, M. N., Teller, A. H., & Teller, E. 1953, *J. Chem. Phys.*, 21, 1087
- Miguel, Y., Kaltenegger, L., Fegley, B., & Schaefer, L. 2011, *ApJ*, 742, L19
- Mollière, P., van Boekel, R., Bouwman, J., et al. 2017, *A&A*, 600, A10
- Mollière, P., Wardenier, J. P., van Boekel, R., et al. 2019, *A&A*, 627, A67
- Monaghan, C., Roy, P.-A., Benneke, B., et al. 2025, *AJ*, 169, 239
- Morris, B. M., Heng, K., Jones, K., et al. 2022, *A&A*, 660, A123
- Morris, B. M., Heng, K., & Kitzmann, D. 2024, *A&A*, 685, A104
- Moses, J. I., Madhusudhan, N., Visscher, C., & Freedman, R. S. 2013, *ApJ*, 763, 25
- Murray, C. D. & Correia, A. C. M. 2010, in *Exoplanets*, ed. S. Seager (University of Arizona Press), 15–23
- NASA Exoplanet Archive. 2024, Planetary Systems Composite Parameters
- Neal, R. 2011, in *Handbook of Markov Chain Monte Carlo* (Chapman and Hall/CRC), 113–162
- Öberg, K. I., Facchini, S., & Anderson, D. E. 2023, *ARA&A*, 61, 287
- Öberg, K. I., Murray-Clay, R., & Bergin, E. A. 2011, *ApJ*, 743, L16
- Owen, J. E. 2019, *Annual Review of Earth and Planetary Sciences*, 47, 67
- Owen, J. E. & Jackson, A. P. 2012, *MNRAS*, 425, 2931
- Owen, J. E. & Wu, Y. 2013, *ApJ*, 775, 105
- Paragas, K., Knutson, H. A., Hu, R., et al. 2025, *ApJ*, 981, 130
- Parmentier, V., Fortney, J. J., Showman, A. P., Morley, C., & Marley, M. S. 2016, *ApJ*, 828, 22
- Parmentier, V., Guillot, T., Fortney, J. J., & Marley, M. S. 2015, *A&A*, 574, A35
- Parmentier, V., Line, M. R., Bean, J. L., et al. 2018, *A&A*, 617, A110
- Parviainen, H. 2015, *MNRAS*, 450, 3233
- Patel, J. A., Brandeker, A., Kitzmann, D., et al. 2024, *A&A*, 690, A159

- Patel, J. A., Egger, J. A., Wilson, T. G., et al. 2023, *A&A*, 679, A92
- Patel, J. A. & Espinoza, N. 2022, *AJ*, 163, 228
- Pepe, F., Cristiani, S., Rebolo, R., et al. 2021, *A&A*, 645, A96
- Pepe, F., Mayor, M., Queloz, D., et al. 2004, *A&A*, 423, 385
- Perryman, M. 2018, *The Exoplanet Handbook* (Cambridge University Press)
- Persson, C. M. 2024, arXiv e-prints, arXiv:2411.19306
- Petigura, E. A., Marcy, G. W., & Howard, A. W. 2013, *ApJ*, 770, 69
- Piette, A. A. A., Gao, P., Brugman, K., et al. 2023, *ApJ*, 954, 29
- Pollacco, D. L., Skillen, I., Collier Cameron, A., et al. 2006, *PASP*, 118, 1407
- Pollack, J. B., Hubickyj, O., Bodenheimer, P., et al. 1996, *Icarus*, 124, 62
- Powell, D., Feinstein, A. D., Lee, E. K. H., et al. 2024, *Nature*, 626, 979
- Prineth, B., Hoeijmakers, H. J., Kitzmann, D., et al. 2022, *Nature Astronomy*, 6, 449
- Prineth, B., Hoeijmakers, H. J., Pelletier, S., et al. 2023, *A&A*, 678, A182
- Rafikov, R. R. 2005, *ApJ*, 621, L69
- Rappaport, S., Barclay, T., DeVore, J., et al. 2014, *ApJ*, 784, 40
- Rappaport, S., Levine, A., Chiang, E., et al. 2012, *ApJ*, 752, 1
- Rasmussen, C. E. & Williams, C. K. I. 2006, *Gaussian Processes for Machine Learning* (The MIT Press)
- Rasmussen, K. C., Currie, M. H., Hagee, C., et al. 2023, *AJ*, 166, 155
- Rauer, H., Catala, C., Aerts, C., et al. 2014, *Experimental Astronomy*, 38, 249
- Raymond, S. N., Barnes, R., & Mandell, A. M. 2008, *MNRAS*, 384, 663
- Ricker, G. R., Winn, J. N., Vanderspek, R., et al. 2014, in Society of Photo-Optical Instrumentation Engineers (SPIE) Conference Series, Vol. 9143, *Space Telescopes and Instrumentation 2014: Optical, Infrared, and Millimeter Wave*, ed. J. Oschmann, Jacobus M., M. Clampin, G. G. Fazio, & H. A. MacEwen, 914320
- Ridden-Harper, A. R., Snellen, I. A. G., Keller, C. U., et al. 2016, *A&A*, 593, A129
- Rivera, E. J., Lissauer, J. J., Butler, R. P., et al. 2005, *ApJ*, 634, 625
- Sanchis-Ojeda, R., Rappaport, S., Pallè, E., et al. 2015, *ApJ*, 812, 112
- Sanchis-Ojeda, R., Rappaport, S., Winn, J. N., et al. 2014, *ApJ*, 787, 47
- Scandariato, G., Singh, V., Kitzmann, D., et al. 2022, *A&A*, 668, A17
- Schaefer, L. & Fegley, B. 2009, *ApJ*, 703, L113
- Seager, S. 2010, *Exoplanet Atmospheres: Physical Processes* (Princeton University Press)
- Seager, S. & Mallén-Ornelas, G. 2003, *ApJ*, 585, 1038

- Showman, A. P. & Guillot, T. 2002, *A&A*, 385, 166
- Showman, A. P. & Polvani, L. M. 2011, *ApJ*, 738, 71
- Sing, D. K., Fortney, J. J., Nikolov, N., et al. 2016, *Nature*, 529, 59
- Singh, V., Scandariato, G., Smith, A. M. S., et al. 2024, *A&A*, 683, A1
- Skilling, J. 2004, in American Institute of Physics Conference Series, Vol. 735, Bayesian Inference and Maximum Entropy Methods in Science and Engineering: 24th International Workshop on Bayesian Inference and Maximum Entropy Methods in Science and Engineering, ed. R. Fischer, R. Preuss, & U. V. Toussaint, 395–405
- Skilling, J. 2006, *Bayesian Analysis*, 1, 833
- Smith, J. C., Stumpe, M. C., Van Cleve, J. E., et al. 2012, *PASP*, 124, 1000
- Speagle, J. S. 2020, *MNRAS*, 493, 3132
- Stevenson, K. B., Désert, J.-M., Line, M. R., et al. 2014, *Science*, 346, 838
- Struve, O. 1952, *The Observatory*, 72, 199
- Stumpe, M. C., Smith, J. C., Catanzarite, J. H., et al. 2014, *PASP*, 126, 100
- Sun, Q., Wang, S. X., Welbanks, L., Teske, J., & Buchner, J. 2024, *AJ*, 167, 167
- Tabernero, H. M., Allende Prieto, C., Zapatero Osorio, M. R., et al. 2020, *MNRAS*, 498, 4222
- Teske, J., Dang, L., Grant, D., et al. 2023, Phase Curve Observations of TOI-561 b To Study Atmosphere-Interior Exchange, JWST Proposal. Cycle 2, ID. #3860
- Thorngren, D. P., Fortney, J. J., Murray-Clay, R. A., & Lopez, E. D. 2016, *ApJ*, 831, 64
- Tsai, S.-M., Lee, E. K. H., Powell, D., et al. 2023, *Nature*, 617, 483
- Tusay, N., Wright, J. T., Beatty, T. G., et al. 2025, arXiv e-prints, arXiv:2501.08301
- Valencia, D., Sasselov, D. D., & O'Connell, R. J. 2007, *ApJ*, 665, 1413
- Valsecchi, F., Rasio, F. A., & Steffen, J. H. 2014, *ApJ*, 793, L3
- Vidal-Madjar, A., Lecavelier des Etangs, A., Désert, J. M., et al. 2003, *Nature*, 422, 143
- von Braun, K., Boyajian, T. S., ten Brummelaar, T. A., et al. 2011, *ApJ*, 740, 49
- von Zeipel, H. 1924, *MNRAS*, 84, 684
- Wakeford, H. R., Sing, D. K., Deming, D., et al. 2018, *AJ*, 155, 29
- Weiner Mansfield, M., Bean, J. L., Brady, M., et al. 2024, A survey to search for silicate vapor atmospheres in the ultra-hot terrestrial planet population, JWST Proposal. Cycle 3, ID. #4818
- Welbanks, L., Madhusudhan, N., Allard, N. F., et al. 2019, *ApJ*, 887, L20
- Winn, J. N. 2010, in *Exoplanets*, ed. S. Seager (University of Arizona Press), 55–77
- Winn, J. N., Sanchis-Ojeda, R., & Rappaport, S. 2018, *New A Rev.*, 83, 37
- Winn, J. N., Sanchis-Ojeda, R., Rogers, L., et al. 2017, *AJ*, 154, 60

- Wiser, L. S., Bell, T. J., Line, M. R., et al. 2025, arXiv e-prints, arXiv:2506.01800
- Wolszczan, A. & Frail, D. A. 1992, *Nature*, 355, 145
- Xue, Q., Bean, J. L., Zhang, M., et al. 2024, *ApJ*, 963, L5
- Zeng, L., Jacobsen, S. B., Sasselov, D. D., et al. 2019, *Proceedings of the National Academy of Science*, 116, 9723
- Zhang, M., Hu, R., Inglis, J., et al. 2024, *ApJ*, 961, L44
- Zhang, M., Knutson, H. A., Wang, L., et al. 2021, *AJ*, 161, 181
- Zieba, S., Hu, R., Kreidberg, L., et al. 2023, The search for regolith on the airless exoplanet LHS 3844 b, JWST Proposal. Cycle 2, ID. #4008
- Zilinskas, M., Miguel, Y., van Buchem, C. P. A., & Snellen, I. A. G. 2023, *A&A*, 671, A138
- Zilinskas, M., van Buchem, C. P. A., Miguel, Y., et al. 2022, *A&A*, 661, A126